DISCLAIMER

This report was prepared as an account of work sponsored by an agency of the United States Government. Neither the United States Government nor any agency thereof, nor any of their employees, makes any warranty, express or implied, or assumes any legal liability or responsibility for the accuracy, completeness, or usefulness of any information, apparatus, product, or process disclosed, or represents that its use would not infringe privately owned rights. Reference herein to any specific commercial product, process, or service by trade name, trademark, manufacturer, or otherwise does not necessarily constitute or imply its endorsement, recommendation, or favoring by the United States Government or any agency thereof. The views and opinions of authors expressed herein do not necessarily state or reflect those of the United States Government or any agency thereof. Reference herein to any social initiative (including but not limited to Diversity, Equity, and Inclusion (DEI); Community Benefits Plans (CBP); Justice 40; etc.) is made by the Author independent of any current requirement by the United States Government and does not constitute or imply endorsement, recommendation, or support by the United States Government or any agency thereof.

Final Technical Report (FTR)

a. *Federal Agency*	Department of Energy	
b. *Award Number*	DE-EE0009158	
c. *Project Title*	A Novel Framework for Performance Evaluation and Design Optimization of PCM Embedded Heat Exchangers for the Built Environment	
d. *Recipient Organization*	University of Maryland, College Park	
e. *Project Period*	*Start:* April 08, 2020	*End:* September 30, 2024
f. *Principal Investigator (PI)*	Vikrant Aute Research Professor vikrant@umd.edu +1 301 405 8726	
g. *Business Contact (BC)*	Catherine Parker Contract Manager caparker@umd.edu +1 301 405 6275	
h. *Certifying Official (if different from the PI or BC)*	N/A	

_____ _____

Signature of Certifying Official *Date*

By signing this report, I certify to the best of my knowledge and belief that the report is true, complete, and accurate. I am aware that any false, fictitious, or fraudulent information, misrepresentations, half-truths, or the omission of any material fact, may subject me to criminal, civil or administrative penalties for fraud, false statements, false claims or otherwise. (U.S. Code Title 18, Section 1001, Section 287 and Title 31, Sections 3729-3730). I further understand and agree that the information contained in this report are material to Federal agency's funding decisions and I have any ongoing responsibility to promptly update the report within the time frames stated in the terms and conditions of the above referenced Award, to ensure that my responses remain accurate and complete.

Acknowledgment

"This material is based upon work supported by the U.S. Department of Energy's Office of Energy Efficiency and Renewable Energy (EERE) under the Building Technologies Office (BTO) Award Number DE-EE0009158. The views expressed herein do not necessarily represent the views of the U.S. Department of Energy or the United States Government."

Disclaimer

"This report was prepared as an account of work sponsored by an agency of the United States Government. Neither the United States Government nor any agency thereof, nor any of their employees, makes any warranty, express or implied, or assumes any legal liability or responsibility for the accuracy, completeness, or usefulness of any information, apparatus, product, or process disclosed, or represents that its use would not infringe privately owned rights. Reference herein to any specific commercial product, process, or service by trade name, trademark, manufacturer, or otherwise does not necessarily constitute or imply its endorsement, recommendation, or favoring by the United States Government or any agency thereof. The views and opinions of authors expressed herein do not necessarily state or reflect those of the United States Government or any agency thereof."

Executive Summary

Thermal energy storage (TES) using phase change materials (PCMs) is attracting increased attention as a viable solution for managing the fluctuating nature of energy demand and shifting peak building loads. PCM-embedded heat exchangers (PCM-HXs) offer high energy storage density and low temperature variation during phase change, making them effective for thermal management. However, assessing PCM-HX component-level performance is typically done using fully transient, and computationally expensive, Computational Fluid Dynamics (CFD) simulations, which presents significant challenges when the ultimate goal is to assess the performance of PCM-HX integrated thermal energy storage systems in the context of a building space conditioning system.

This research sheds light on the performance evaluation and design optimization of PCM-HXs for the built environment, addressing several barriers to practical issues to PCM-HX commercialization such as modeling aspects (i.e., modeling expertise and computational / time investment, etc.), manufacturing aspects (i.e., at-scale manufacturing, cost assessments, etc.) and experimental performance assessment (i.e., reliable experimental data, assessment of multiple PCM-working fluid combinations, etc.).

We present a novel, comprehensive, and experimentally-validated design optimization framework for PCM-HXs capable of simulating any PCM-HX geometry with reasonable accuracy and significant computational time savings when compared to traditional CFD-based design practices. The framework was validated for a wide range of PCM-HX configurations, including a design optimization for a domestic hot water heater application where TES partially replaces electrical heating input. The resulting PCM-HXs were found to deliver 34-68% of the total daily hot water supply with only 5-10% package volume increase from the water heater, thus within U.S. DOE targets for TES systems.

To identify the most promising HXs for PCM applications, first-order geometry and cost analyses were conducted based on off-the-shelf HX products. As part of this work, 9 PCM-HX prototypes were manufactured using additive and conventional manufacturing methods. Detailed economy-of-scale assessments were conducted for the most promising PCM-HXs and were found to have a good outlook for the next 5-10 years.

The PCM-HX design optimization framework was validated through comprehensive in-house experimental testing using newly-developed PCM-to-fluid test facilities. In total,10 total in-house component-level experiments were conducted using these prototypes, including 9 with water and 1 with refrigerant (R410A) as the working fluid. It was found that the framework can successfully predict experimental thermal-hydraulic performance within ±10-20% the first time without manual design changes, eliminating the need for time-consuming and expensive prototyping efforts as part of the design process.

As part of this work, a publicly-available PCM web tool was released which includes a PCM property database (531 PCMs) and PCM-HX modeling tool to assist the design community on common PCM-HX use-cases, e.g., single/multiple flow path(s) fluid-to-PCM and air-to-fluid-to-PCM configurations (https://ceeeweb.umd.edu/pcmapp/). This work will accelerate the design and time to market for next generation PCM-HXs.

Table of Contents

Acknowledgment 2
Disclaimer 2
Executive Summary 3
Table of Contents 4
Background 6
Motivation 6
Literature Survey: Modeling Techniques of PCM-HX 7
Literature Survey: PCM-HX Heat Transfer Enhancement Techniques 14
Enhancement using Extended Surfaces 15
Enhancement using Highly Conductive Porous Materials 16
Literature Survey: PCM Experimentation 17
Research Gaps 19
Project Objectives 20
Project Discussion and Results 22
PCM-HX Modeling, Analysis and Optimization (M1.4; M2.1; M2.2; M2.3; M2.4; M3.2) 22
CFD Modeling: Effect of Thermophysical Properties on PCM-HX Simulation (M1.4) 22
CFD Modeling: FEM-CFD 32
Resistance-Capacitance Model Development (M2.1, M2.3, M2.4)) 36
Generalized Resistance-Capacitance Model (GRCM) (M3.1, M3.2, M3.3) 44
Performance Maps for Fast & Accurate Building Energy Simulations (M3.2) 59
PCM-HX Manufacturing (M1.1, M1.4, M2.2, M3.1) 70
First Order Analysis of PCM-HX Configurations (M1.1) 70
Recommendations for PCM-Embedded HXs (M1.4, M2.2, M3.1) 73
PCM-HX Prototypes Summary (M1.4, M2.2, M3.1) 76
Cost Assessment of At-Scale PCM-HX Manufacturing (M3.3) 86
PCM-HX Experimentation 92
PCM-HX Test Facility Development 92
Summary of PCM-HX Experimental Work 94
Develop Web/Desktop (UI) that incorporates the reduced order models (M1.3, M2.3; M3.2) 114
PCM Property Database (M1.3) 114
Thermal Battery Analysis Tool (M2.3, M3.2) 116
Significant Accomplishments and Conclusions 119
PCM-HX Modeling, Analysis and Optimization 119
PCM-HX Manufacturing 119
PCM-HX Experimentation 120
Path Forward 121
PCM-HX Modeling, Analysis and Optimization 121
PCM-HX Manufacturing 121
PCM-HX Experimentation 121
Products 122
Journal Publications in Preparation: 122

Conference Publications 122
In Print 122
Master Thesis in Print 123
Project Team & Roles 124
University of Maryland, College Park (UMCP) 124
Heat Transfer Technologies, LLC (HTT) 124
References 125

Background

Note: The contents of this section have been published in the following citations: Alam, 2023 [1].

Motivation

The energy consumption worldwide is predicted to grow by approximately 50% between 2018 to 2050 [2]. Heating, ventilation, and air conditioning (HVAC) accounts for 38% of building energy consumption, equivalent to 12% of global energy [3]. As energy demand rises, the grid-demand response becomes more challenging and will result in higher carbon emissions, especially when using traditional fossil fuel-based energy sources. Renewable energy such as wind and solar will play a significant role in reducing carbon emissions, but they have intermittency. Energy storage is a necessary component to address these challenges. In addition to smoothing the variability in renewable energy production, storage technology can also provide backup or standby power that comes from fossil fuel sources.

Thermal energy storage (TES) is a promising technology due to its relatively low cost and lower environmental impact compared to alternative energy storage methods [4]. TES systems can store energy as sensible heat, latent heat, or through thermochemical processes. While thermochemical energy storage offers high energy density and long-term storage potential, its typically high transition temperatures make it unsuitable for most HVAC applications (Figure 1).

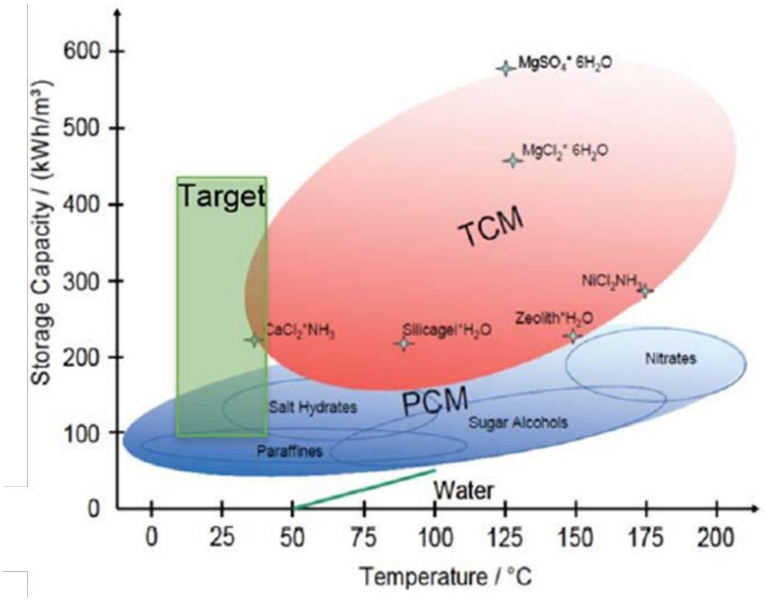

Figure 1: PCM Storage Capacity and Target Application Range [5]

The sensible and latent energy systems are considered mature technology and has been widely researched [6]. The main advantage of latent systems over sensible is its high energy density and the capacity of storing a large amount of energy within a small

temperature range. Latent thermal storage use phase-change materials (PCMs) to absorb or release latent heat in a narrow temperature range. PCM heat exchangers (PCM-HXs) can offer an efficient way to reduce peak load by using the energy stored in off-peak hours to offset the on-peak load partially or fully. The load shifting tries to take advantage of the difference in electricity demands between different times of the day (Figure 2).

Figure 2: Load shifting control enabled by TES systems such as PCM-HXs [7]

This research sheds light on PCM-HX design by establishing a novel framework for the performance evaluation and design optimization of PCM embedded heat exchangers with applications to the built environment.

Literature Survey: Modeling Techniques of PCM-HX

PCM energy storage models have been developed using both analytical and numerical methods in the literature. Elgafy & Lafdi [8] developed a 1-D analytical model to predict the effective thermal conductivity of PCM enhanced with uniformly distributed carbon nanofibers, using the effective thermal resistance method. Their study focused solely on thermal conductivity, without addressing transient temperature profiles or energy storage. Lamberg & Siren [9] proposed an approximate analytical model for solidification in a rectangular PCM storage with internal fins, predicting the solid–liquid interface location and fin temperature distribution. The model assumes a constant solidification temperature and wall temperature, simplifications that do not fully capture the behavior of real PCMs, which typically exhibit a temperature range for phase change and non-uniform wall temperatures. The analytical solution is comprised of the Neumann solution [10] for the solid-liquid interface location and a derived analytical solution for the temperature distribution of the fin. Shamberger [11] introduced a figure of merit (FOM) for PCMs based on the analytical solution of the two-phase Neumann-Stefan problem [12] under constant wall boundary conditions. The FOM is strongly influenced by PCM thermophysical properties and is defined by Equation (1), where α is the thermal diffusivity, k is the conductivity, the subscript *l* denotes liquid phase and λ is the solution to the transcendental equation which describes the position of meting front [11].

$$FOM = \frac{k_l}{\sqrt{a_l}\, erf(\lambda)} \quad (1)$$

FOM can be used as an objective function for selection of material for electronics based thermal management that require faster dynamic response. Yazawa et al. [13] built on this study and used a lumped mass model for mapping different materials showing power and energy tradeoff. FOM was used to compare the cooling power capability of different PCMs and single-phase materials. FOM was also plotted against energy density to graphically demonstrate performance tradeoff between different materials as shown in Figure 3.

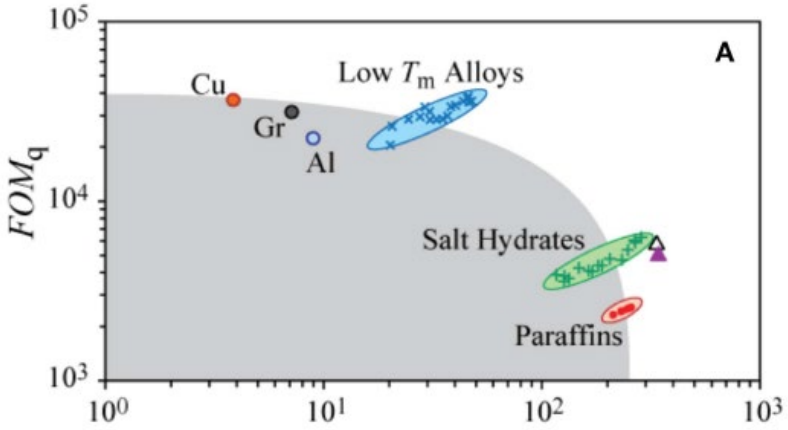

Figure 3 : FOM against specific energy for different PCMs and single phase materials [13]

Table 1: Thermophysical properties of PCMs and calculated FOM

PCM	Specific Heat (J/kg-K)	Thermal Conductivity (W/m-K)	Latent Heat, (kJ/kg)	Density (kg/m^3)	FOM (W/K-m^2-s$^{0.5}$)	Energy Density (MJ/ m^3)
RT35	1800(s) 2400(l)	0.2	160	860(s) 770(l)	2391	130.4
RT62HC	1800(s) 2400(l)	0.2 (s) 0.1(l)	230	850(s) 840(l)	2134	194.4
RT35+ Copper foam (2%)	1772(s) 2360(l)	7.8	156.8	1021(s) 933(l)	16300	127.8
ClimaSel 32	3600	1.08(s) 0.76(l)	145	1500	7178	217.5

Using the approach from Shamberger [11], a FOM and energy density were calculated for the PCMs used in the studies shown in Table 1. The first two PCMs are organic, while the third is a composite consisting of 98% RT35 and 2% copper foam, with its properties estimated based on effective porosity. The final entry represents the inorganic PCM ClimaSel32. From the table and equation (1), thermal conductivity is the primary factor influencing the FOM; Shamberger [11] reported that it accounts for 92.8% of the variance across materials. The composite PCM exhibited the highest FOM but the lowest energy

density, due to reduced PCM volume from metal foam inclusion. This highlights the importance of thermal conductivity enhancement in PCM-based storage systems while also illustrating the trade-off between energy storage capacity and thermal response (i.e., power density).

Analytical models offer the advantage of low computational cost and the ability to identify performance trends. However, they are typically limited to one-dimensional problems and simplified geometries. For more complex domains, boundary conditions, or phase-change behaviors involving mushy zones, numerical methods are required.

Numerical methods, such as finite difference, finite element and finite control volume methods are more powerful in solving the complex multidimensional models. The use of Computational Fluid Dynamics (CFD) is the most extensively found in various heat transfer applications, including PCM-HX's [14] - [30]. Figure 4 illustrates the 3D meshing of different PCM-HX geometries created for CFD analysis. CFD usually imposes high computation cost especially for complex problems such as time-dependent phase-change processes. Bacellar et al. [31], [32] investigated reduced order model using CFD-based correlations and reduced order domain for faster evaluation of PCM-HX. The results showed good match to the CFD simulations with 4 to 5 orders of magnitude less computational cost compared to CFD. But generating correlations that cover a large design space can still be computationally expensive. In certain applications, this may become prohibitive as such that a faster simulation engine with a certain degree of accuracy penalty is acceptable and needed.

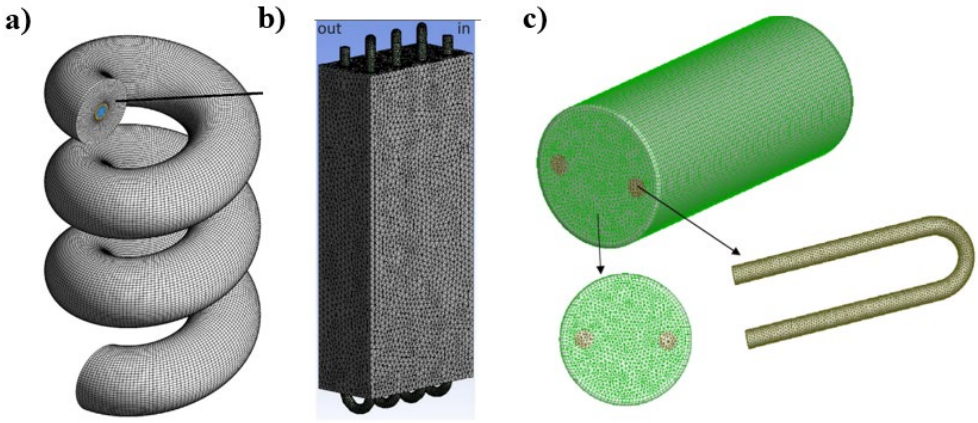

Figure 4: 3D meshing of a) Double pipe helical coil PCM-HX [33] b) PCM-HX with spiral-wired tubes [27] c) Shell and tube PCM-HX with heat pipe[34]

Lattice Boltzmann method (LBM) is a mesoscopic numerical method [35] which has been used to model heat transfer process in PCM-HX. While CFD solves the Navier-Stokes equations, LBM solves the Boltzmann equation [35] in discrete forms and the implementation of this method can describe the fluid motion without solving the Navier-Stokes equations. LBM can have 2 times lower computational cost [36] than CFD due to the model using explicit scheme and local interactions. Consequently, this approach has a very low communication ratio to run efficiently in parallel supercomputers [37].

Liu and He [38] developed a LBM model for PCM melting in porous media and verified the model with data from literature. Gao et al. [39] used an enthalpy-based LBM for porous PCM melting with fins where the solid-liquid phase interface is distinguished by calculating liquid fraction. Li et al. [40] proposed an axisymmetric LBM for PCM-HX solidification and validated their model by the experimental data from Sparrow et al. [41]. The study also showed that LBM can be two orders of magnitude faster compared to CFD. Chen et al. [42] developed a axisymmetric LBM model for melting in a cylindrical heat exchanger with copper foam. The model was validated from experimental data [43] and good match of experimental temperature and predicted temperature was found. While LBM can be faster than CFD, most of the PCM-HXs simulated with LBM are comparatively simple and use constant temperature or constant heat flow boundary conditions. The conjugate heat transfer between HTF and PCM is usually not considered as the implementation of energy conservation scheme in LBM is not straightforward. The pre-processing of input and post-processing of output data is also complex in LBM. The twofold speed gain by using LBM may still be restrictive for applications where faster turnaround is required and thus a faster solver is needed.

An alternate approach is the resistances and capacitances-based models (RCM), which has been used for developing building thermal models [44] and heat exchanger modeling [45]. Unlike CFD or LBM, RCM does not solve for the high-order physics which means the continuity and momentum equations. The model only solves for the energy balance equation and thus have significantly less computational cost. The PCM domain is represented with thermal resistance and capacitance [46]-[50] and an example is shown in Figure 5 which represents a RC network representation for a shape-stabilized PCM slab. This method can provide good estimation of heat transfer rate and energy storage. Gao et al. [48] reported that the average error of surface temperature and heat flux predictions are 0.42°C and 15% respectively when compared to experimental data for a shape-stabilized PCM slab. Mirzaei et al. [50] compared their model against CFD and the obtained mean errors for solidification and melting process were found to be 0.11 K and 0.44 K respectively. These models are 1D and assume conduction as the dominant heat transfer mechanism.

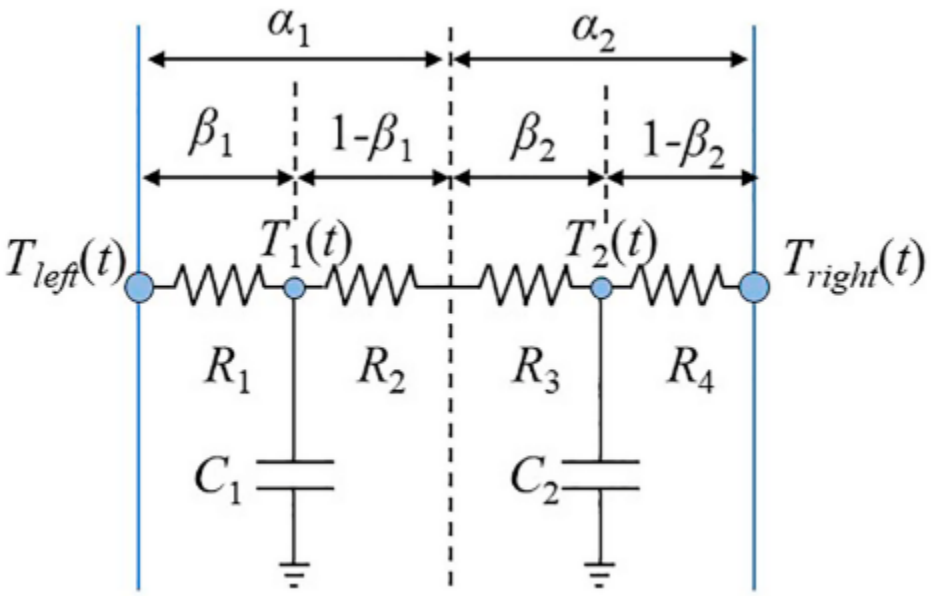

Figure 5: Schematic of the RC network of Shape-Stabilized PCM Slab [48]

Pan et al. [51] introduced an approach which they named Layered Thermal Resistance (LTR) for PCM-HX solidification simulation in multi-dimensions with and without fins. The model assumes a quasi-steady heat conduction approach. The liquid PCM is assumed to be solidified layer by layer and once a layer is fully solidified the solidification front moves to the next layer as shown in Figure 6. The total solidification time of the domain is estimated by summing up the solidification times of all the different layers. When compared to a CFD model it was first found that the LTR model overestimated the solidification time by 50-60%. A regression model was later used to find a tuning parameter from the CFD model to tune the resistance in LTR. The model was verified with a CFD model after the tuning. However, this tuning with the configuration and operation specific correction factor limits its applicability.

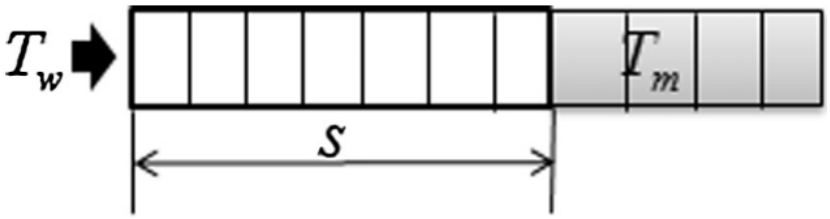

Figure 6: 1D Layered Thermal Resistance solidification front [40]

Parsazadeh et al. [52] proposed an improved LTR model for better prediction of the solid-liquid phase change process. Unlike the original model, this improved model considered transient heat conduction in each layer and did not use a tuning factor. The new model showed better predictions of solidification time than the previous model for large Stefan numbers (ratio of sensible-to-latent heat). The higher Stefan number indicates more sensible heat utilization which means higher degree of superheating or subcooling.

Neumann et al. [53] proposed a simplified 2D RC-model for a flat plate PCM energy storage. The model accounted for free convection during the melting process in

rectangular PCM gaps between the flat plates (Figure 7), based on CFD based correlations developed by Vogel et al. [54]. According to Vogel et al. [54] the natural convection effect is significant when the melting process reaches a critical liquid fraction which is a function of the Rayleigh number (Ra) and geometry parameter A in Equation (2).

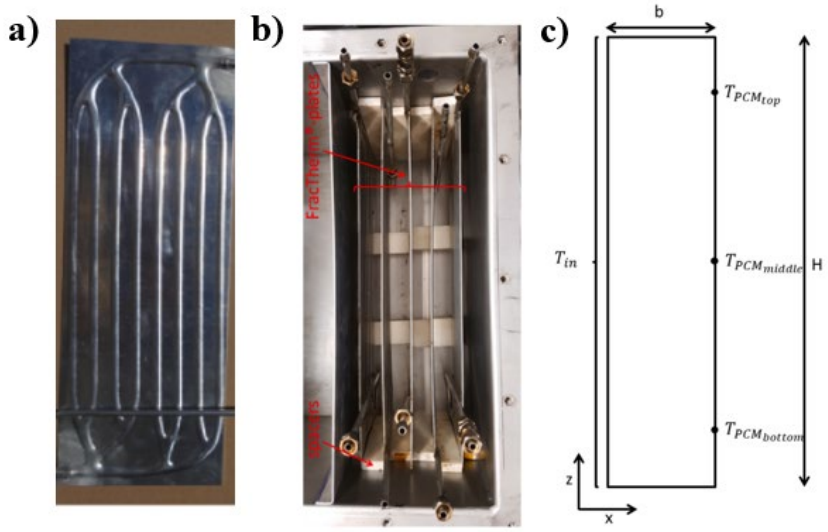

Figure 7: Schematic of a) used flat plate b) top view of storage envelope c) 2D computational domain for a PCM gap [42]

A is the ratio of PCM gap (b) and the gap height (H) as shown in Figure 7c. If the liquid fraction (f) was lower than the critical liquid fraction f_{crit}, the heat transfer in the RC-model was defined by only heat conduction. If the liquid fraction goes over the critical value a reduction factor $\bar{\varepsilon}$ is used to add the effect of natural convection in the model as shown in Equation (3). These equations are developed for rectangular PCM gaps in flat plate PMCHX and may not be valid for other configurations.

$$f_{crit} = \sqrt[4]{\frac{150A}{Ra}} \tag{2}$$

$$\bar{\varepsilon} = \begin{cases} 1 & \text{for } \mathrm{Ra}^{\frac{1}{6}}\mathrm{A}^{-\frac{1}{4}} < 2.73 \\ 0.57\left(\mathrm{Ra}^{\frac{1}{6}}\mathrm{A}^{-\frac{1}{4}}\right) - 0.38 & \text{for } \mathrm{Ra}^{\frac{1}{6}}\mathrm{A}^{-\frac{1}{4}} \geq 2.73 \end{cases} \tag{3}$$

Neumann et al. [53] validated the RC-model with a finite element model (FEM), and reported that the mean deviation of the outlet fluid temperature and PCM temperature between both models were 0.62Kand 0.85K, respectively. The simulation time for the RC model was reduced by 20-30 times compared to the FEM. This study considered a geometry where the motion of liquid PCM is significant. But for geometries where the flow of molten PCM is negligible, the natural convection effect can be considered less dominant and be dismissed in favor of computational speed gains [31].

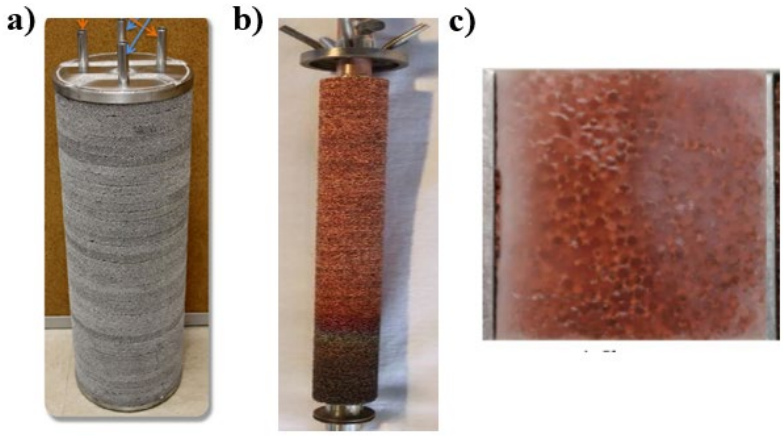

Figure 8: PCM-HX with a) Cylindrical Aluminum Metal Foam [55] b) Cylindrical Copper Metal Foam [43] c) Rectangular Copper Metal Foam [56]

Different PCM-HX modeling approaches covered in this review are summarized in Table 2. Table 3 briefly summarizes different PCM-HX modeling approaches based on the accuracy, computational cost and the ability to solve complex geometries.

Table 2: Summary of Different Modeling Techniques

Author	Model Type	Software	Dimension	Validation
Elgafy & Lafdi [8]	Analytical	NA	1D	Yes. Experimental
Lamberg & Siren [9]	Analytical	NA	1D	No
Longeon et al. [20]	CFD	Ansys FLUENT	2D	Yes. Experimental
Pu et al. [23]	CFD	Ansys FLUENT	2D	Yes. Data from Longeon et al. [20]
Zhang et al. [29]	CFD	Ansys FLUENT	2D	Yes. Data from [57]
Tay et al. [24]	CFD	Ansys CFX	3D	Yes. Data from Tay et al. [58]
Duan et al. [59]	CFD	Ansys FLUENT	3D	Yes. Experimental
Yang et al. [26]	CFD	Ansys FLUENT	2D	Yes. Experimental
Jian-you [60]	Simple iterative model	NA	1D	Yes. Experimental
Al-Abidi et al [14]	CFD	Ansys FLUENT	2D	Yes. Experimental
Mat et al. [22]	CFD	Ansys FLUENT	2D	Yes. Experimental
Mahdi & Nsofor [61], [62]	CFD	Ansys FLUENT	2D	Yes. Data from Esapour et al.[57]
Youssef et al. [27]	CFD	Ansys FLUENT	3D	Yes. Experimental
Ebrahimi et al. [15]	CFD	Ansys FLUENT	3D	Yes. Data from Elgafy et al. [57]
Mahdi et al. [21]	CFD	Ansys FLUENT	3D	Yes. Experimental
Koukou et al. [18]	CFD	Ansys FLUENT	2D	Yes. Experimental
Hu et al. [63]	CFD	Ansys FLUENT	2D	Yes. Data from Akgün et al. [64]
Faghani et al. [65]	CFD	Ansys FLUENT	2D	Yes. Data from Assis et al. [66]
Assis et al. [66]	CFD	Ansys FLUENT	2D	Yes. Experimental
Zhao et al. [67]	CFD	Ansys FLUENT	2D	Yes. Data from Al-Abidi et al. [68]
Zhang et al. [69]	CFD	ANSYS Fluent	3D	Yes
Fahad et al. [70]	CFD	ANSYS Fluent	2D	Yes Data from [71]
Kurnia and Sasmito [72]	CFD	ANSYS Workbench	3D	Yes Data from [73]
Liu et al. [74]	CFD	ANSYS Fluent	2D	Yes

				Data from [75]
Yadav et al. [76]	CFD	ANSYS Fluent	3D	Yes Data from [77]
Yang et al. [78]	CFD	ANSYS Fluent	2D	Yes Data from [79]
Oskouei and Bayer [80]	CFD	ANSYS Fluent	3D	Y
Najafian et al. [81]	-	TRNSYS	2D	No
Righetti et al.[82]	-	TRNSYS	2D	Yes. Experimental
Dhumane et al. [83]	-	Modelica	NA	Yes, Data from Du et al. [84]
Dhumane et al. [85]	-	Modelica	NA	Yes, Data from Du et al. [86]
Promoppatum et al.[87]	CFD	COMSOL	2D	Yes. Experimental
Zhang et al. [88]	CFD	COMSOL	2D	Yes, Experimental
Calvet et al. [89]	CFD	COMSOL	2D	Yes. Experimental
Bacellar et al. [31]	CFD	Ansys FLUENT	2D	NA
Bacellar et al.[32]	CFD	Ansys FLUENT	2D	NA
Velraj et al.[90]	FDM	NA	1D	Yes. Experimental
Ismail et al.[91]	FDM	NA	1D	Yes. Experimental
Erek et al. [92]	FDM	FDM	2D	Yes. Experimental
Liu & He[38]	LBM	NA	2D	No
Gao et al. [39]	LBM	NA	2D	No
Li et al. [93]	LBM	NA	2D	Yes. Data from Sparrow et al. [41]
Liu et al. [94]	LBM	NA	2D	No
Chen et al.[42]	LBM	NA	2D	Yes. Data from Martinelli et al.[43]
Zhu et al. [46]	RCM	NA	1D	Yes. Experimental
Bontemps et al. [47]	RCM	TRNSYS	1D	Yes. Experimental
Gao et al. [48]	RCM	NA	1D	Yes. Experimental
Stupar et al. [49]	RCM	NA	1D	No
Mirzaei et al. [50]	RCM	NA	1D	No
Neumann et al. [53]	RCM	NA	2D	Yes. Experimental
Ling et al. [95]	RCM	NA	2D	Yes

Table 3: Comparison of PCM-HX Modeling Approaches

Approach	Physics Order	Accuracy	Computational Cost
Analytical	Low	Low	Low
RCM	Low	Medium	Low
LBM	High	High	High
RCM	High	Very High	Very High

Literature Survey: PCM-HX Heat Transfer Enhancement Techniques

Common PCM materials include organic materials, such as octadecane, paraffin wax, and eicosane, inorganic salt hydrates and eutectic alloys. Organic PCMs are widely used due to their high latent heat storage capacity per unit mass, chemical stability, and negligible supercooling. However, they typically exhibit low thermal conductivity, which hinders efficient heat transfer and can limit the rate at which the stored energy is released, often resulting in suboptimal temperature control [96]. Research has been conducted to improve the thermal conductivity of PCM, by increasing the surface area of heat exchanger (i.e. fins, metal foams, graphite) or integrating with thermally conductive fillers

such as nanoparticles [97], [98], [99]. The most common heat transfer enhancement techniques thus involve the use of extended surfaces such as fins and metal foams.

Enhancement using Extended Surfaces

The incorporation of fins is a simple yet effective strategy to enhance heat transfer in TES systems. The selection of fin material depends on various factors, including thermal conductivity, density, cost, and corrosion resistance [100]. Velraj et al. [90] conducted both numerical and experimental studies on a cylindrical vertical tube filled with PCM and equipped with internal longitudinal fins. Their findings showed that the solidification time decreased approximately in proportion to 1/n, where n is the number of fins. They also developed a theoretical model that accounted for circumferential heat conduction through the tube wall, using an enthalpy-based formulation solved via a fully implicit finite difference method. Choi et al.[101] experimentally investigated the performance of finned and non-finned tubes in a low-temperature TES system, focusing on the effects of heat transfer fluid (HTF) inlet temperature and flow rate on solidification. Their results demonstrated that thin fins had a negligible impact on heat transfer, while thick fins nearly doubled the heat transfer coefficient compared to the non-finned configuration.

Table 4 provides a summary of key numerical and experimental studies on LHTES systems. While these studies consistently confirm that the addition of fins enhances heat transfer during phase change, they often overlook the trade-off between improved performance and the reduction in available PCM volume due to fin insertion. Consequently, optimizing fin design is essential yet challenging. Most existing research efforts focus on optimizing a single parameter, such as fin number, height, or spacing, rather than employing multi-variable or holistic optimization approaches [102], [103], [104], [105].

Table 4: Summary of studies for heat transfer enhancement with fins

Ref	Fin Material	Fin Geometry	Study Type	Sol/Melt	Notes
[90]	Aluminum	Rectangular	Exp, Sim	Sol	Solidification time is faster approximately by the reciprocal of number of fins.
[101]	Steel	Circular	Exp	Sol	Thick-finned-tube system gives about 2 times higher heat transfer coefficient than the non-finned tube.
[91]	-	Rectangular	Exp, Sim	Sol	Increase in fin number reduced the solidification rate by about 14%.
[106]	Steel	Rectangular/vertical	Exp	Both	About 40% reduction in solidification time due to the presence of fins.
[107]	Bronze	Circular	Exp, Sim	Sol	The energy storage increases with increasing fin radius and decreasing fin space.
[57]	Copper	Spiral	Exp	Melt	The equivalent thermal conductivity of the PCM increased by 3 times due to the presence of the fins. Furthermore, reducing the fin pitch leads to better melting process.
[108]	Copper	Longitudinal, circular	Exp	Both	System with longitudinal fins gave the best thermal response during melting than the one with circular fins.

[68]	Copper	Rectangular	Exp, Sim	Both	Increase in HTF inlet temperature, mass flow rate and fin height give higher PCM melting rate.
[14]	Copper	Rectangular	Exp, Sim	Melt	The total melting time with the highest number of fins was decreased by 34.7%.
[22]	Copper	Rectangular	Exp, Sim	Sol	The total solidification time for TTHX geometry with the highest number of fins was decreased by 35%.
[109]	Copper	Rectangular	Exp, Sim	Melt	The use of internal–external fin reduced the melting time of the PCM by 43.3%.
[110]	Brass	Rectangular/longitudinal	Exp	Both	About 12.5% and 24.52% reduction in melting time for HTF inlet temperature 80°C and 85°C respectively due to fins.
[111]	-	Y-shaped	Sim	Sol	The optimized unit can achieve an increase of 24% of the system efficiency.
[112]	Aluminum	Rectangular	Exp	Both	Mainly investigated the effects of HTF flow parameters.
[113]	Aluminum	Rectangular	Sim	Melt	Transient melting process of the PCM depends on the thermal and geometrical parameters of the system.
[114]	Aluminum	Rectangular	Sim	Both	The minimum enhancement rate achieved with widely spaced fins was 3 times higher.
[90]	Copper	Rectangular	Sim	Melt	The use of fins promotes rapid melting, followed by a low melting after the PCM in the inter-fin regions has been liquefied.
[101]	Aluminum	Rectangular	Sim	Sol	The results showed faster energy extraction from the PCM to the HTF

Enhancement using Highly Conductive Porous Materials

A simple and effective way to enhance the thermal conductivity of PCMs is by the impregnation of porous materials of high thermal conductivity into pure PCM. Table 5 highlights various experimental and numerical studies on LHTES system which was enhanced by highly conductive porous materials. Aluminum/copper foam and expanded graphite (or graphite foam) are found to be the most widely used conductive materials. This is due to their relatively low or medium densities and high thermal conductivities as hinted earlier compared to other additives. Increasing the volume fraction of porous materials can increase the melting/solidification rate but it can also decrease storage capacity.

Table 5: Summary of studies for heat transfer enhancement with porous materials

Ref.	Material	Summary/Key Findings
[115]	Metal matrix	The melting rate increases with increase in the matrix porosity.
[116]	Graphite matrix	The composite matrix has a thermal conductivity 20–130 times greater than that of pure PCM.
[117]	Polyethylene glycol, silica gel, and β-Aluminum nitride powder	The thermal conductivity increased from 0.3847Wm^{-1} K^{-1} to 0.7661Wm^{-1} K^{-1} with the mass ratio of β-Aluminum nitride from 5% to 30%.
[118]	Metal foam	The heat transfer rate is enhanced by 5–20 times.

[119]	Aluminum foam	The presence of aluminum foam reduced the discharging time by 42.42% and also decreased the charging time by 15.37%.
[120]	Aluminum foam	The aluminum foam indicates considerable promise as a thermal conductivity enhancer
[121]	Expanded graphite (EG)	Increasing the mass fraction of EG from 2% to 10% increased the thermal conductivity of paraffin/EG composite PCM.
[122]	Aluminum foam	Melting time by using higher porosity or bigger pore size aluminum foams, as compared to foams with lower porosity or smaller pore size.
[123]	Copper porous foam (CPF)	The CPF increased the effective thermal conductivity from 0.423 W/m K to 3.06 W/m K.
[124]	Graphite foams (GFs)	Pore-size and thickness of ligaments of the foam played a key role in improving the thermal conductivity and the storage capacity of the Paraffin-GF composite.
[125]	Compressed expanded natural graphite (CENG)	Thermal conductivity of the paraffin wax/CENG composites can be 28–180 times that of the pure paraffin wax.
[126]	Copper, steel alloy and EG	The heat transfers rate can be enhanced by the metal foam, the EG and the mixture of metal foam and EG by 210%, 190% and 250%, respectively.
[127]	Copper foam, copper-steel alloy and EG	Heat transfer is enhanced by both metal foams and EG, which reduce the charging and discharging period.
[128]	Copper foam, EG	Adding metal foams and EG into PCMs can enhance the heat transfer whilst influence the heat storage capabilities.
[129]	Copper matrix	Both melting and solidification times are substantially reduced.
[115]	Aluminum foam	The heat transport of wax/foam composite was mainly dominated by the heat conduction in the metal matrix, and the effect of the metal foam structure on the heat transfer is significant.
[116]	Copper foam, Nickel foam	Natural convection was dominant during melting in the case of pure molten-salt and it was weakened in the case of molten-salt with metal foam. The heat retrieval process was enhanced by the presence of the metal foam.

Literature Survey: PCM Experimentation

Conceptually, integration of LHTES into various building applications can yield significant energy savings by shifting the peak heating and cooling demands and enabling buildings

to minimize their on-peak electricity usage. However, achieving high-performance LHTES while maintaining compactness is often challenging due to inherent thermophysical properties of PCMs, such as latent heat content, low thermal conductivity, volume change ratio during melting, and supercooling. Hence, a purpose-built test bench that can work alongside the simulation model is essential to efficiently develop and validate various PCM-HX concepts. It is also important to note that the investigation of a simple baseline configuration is a crucial step for researchers to further develop and improve the design in the future. Longeon et al. [20] and Mehta et al. [130] conducted experimental research in conjunction with simulation models using the vertical straight shell-and-tube configuration to investigate the performance of each PCM-HX while validating the physical phenomena. The experimental research provides useful test results and conclusions that can be compared and referenced. However, the energy balance assessment of the PCM-HXs is often neglected due to the absence of proper heat loss estimation. Moreover, the large amount of heat loss becomes a by-product of not using any insulation to maintain the visibility of the testing progress. Conversely, the use of conventional insulation sheets does not allow phase change observation during testing.

As discussed previously, PCM-TES systems suffer from inadequate thermal performance stemming mainly from the PCM's low thermal conductivities. The use of radial fins with an annular tube to reduce the PCM-side thermal resistance is one of the promising options among those improvement measures because of its simple configuration and high thermal performance enhancement effect [131]. Therefore, it is crucial to accurately understand the thermal behavior of the finned-tube configuration under various test conditions to enhance the thermal performance of the future finned-tube designs. Karami and Kamkari [132] experimentally investigated the thermal performance of the radial fins on an annular tube in vertical orientation under different HTF inlet temperatures and mass flow rates and checked the melting performance of the PCM-HX with the recorded images and installed thermocouples. Numerous studies have been conducted to understand the thermal performance and behavior of the finned-tube PCM-HX with radial fins. However, for both numerical and experimental studies, heat loss and thermal mass assessment of the test setup often get neglected for simplicity.

Numerous studies have explored and discussed various PCM-HX configurations to integrate them into potential HVAC&R applications, with most focusing solely on single-phase fluid as the preferred heat transfer fluid in the tube side. Choure et al. [133] reviewed various methods of heat transfer enhancement techniques for PCM-HX-based TES systems, albeit focusing on water as HTF. While there is limited literature on studies utilizing two-phase refrigerant as HTF, Qiao et al. [134] conducted an experimental study on PCM-HX used in a personal cooling device with R-134a as the chosen HTF, emphasizing a system-level analysis and comparing different copper tube-based in-house HX configurations and PCM-side heat transfer enhancement techniques. Khalifa and Koz [135] numerically investigated the solidification process of a serpentine-shaped PCM-HX evaporator in a vapor compression refrigeration system using a quasi-2D model, but experimental validation with an actual two-phase refrigerant was not conducted; water was instead utilized as the HTF.

Research Gaps

Based on the current literature review, the research gaps are as follows:

- PCM Thermophysical Properties
  - There is a high degree of uncertainty regarding the accuracy of PCM thermophysical properties and their uncertainty across the literature;
  - CFD-based studies have not extensively discussed the effects of thermophysical properties that are less frequently available in open literature
- PCM-HX Modeling, Analysis, & Optimization
  - CFD simulations are widely used but present high computational cost, which is a challenge for PCM-HX design optimization;
  - Reduced-order models for PCM-HXs, e.g., RCMs, are geometry-dependent and require redefinition of the RC network for each new PCM-HX configuration, which limits scalability and rapid prototyping
  - In most RCMs, the boundary conditions are constant heat flux or wall temperature, and there are not many validated models with conjugate heat transfer between heat transfer fluids (HTFs) and PCMs;
  - The literature lacks discussion on systematic design optimization workflows for PCM-HX optimization using RCMs and multi-objective optimization;
  - The literature lacks modeling frameworks for system-level optimization and performance prediction of HP-TES using PCMs in a computationally-efficient manner
- PCM-HX Manufacturing & Experimentation
  - The literature lacks comparative analyses across several PCM-HX configurations, toward identifying the most promising PCM-HX architectures for a given application;
  - PCM-HX experimental facilities in literature are configuration-specific, i.e., changing the PCM-HX configuration requires a new test setup. These test setups also do not comprehensively consider heat losses, HX thermal mass assessments, and visualizations.
  - No literature investigating component-level performance of PCM-embedded HXs which utilize refrigerants (i.e., phase-changing fluids) as the working fluid.

Project Objectives

The main objective of this project was to develop and test PCM embedded heat exchangers (PCM-HX) which meet the performance metrics defined in Table 6. Additionally, an online PCM-HX performance simulation tool was developed to assist the design community on common PCM-HX use-cases, e.g., single/multiple flow path(s) fluid-to-PCM and air-to-fluid-to-PCM configurations. The SOPO table is summarized in Table 7.

Table 6: PCM-HX Performance Metrics.

Metric Description	Metric
Demand Reduction (1)	≥ 50%
Time Period	≥ 4 hours
Volume increase (1)	≤ 10%
Weight increase (1)	≤ 10%
Simple Payback Period (2)	≤ 5 years
Operation	Start/Stop Multiple times as required
Technology Lifetime (1)	≥ baseline
Service & Installation (1)	≤ baseline
Note (1): Measured with respect to baseline conventional heat exchanger Note (2): The system cost includes all part for operation, including all energy storage parts and subcomponents.	

Table 7: SOPO Table.

Task Number	Task /Subtask Title	Milestone Type	Milestone Number	Milestone Description
1	Intellectual property management plan (IPMP) development	Milestone	1.0	IPMP is completed
1.1	Establish two applications of interest	Milestone	1.1	Two PCM-HX applications determined
1	Develop a new framework for design optimization	Milestone	1.2	The first version of the PCM-HX design framework is completed and two optimized heat exchangers are designed
1	Set up PCM property database	Milestone	1.3	a PCM database including commonly used PCMs is established
1	Fabricate and test simple PCM-HX geometries for fundamental control volume validation	Milestone	1.4	Fundamental control volume validation completed
[redacted]		Go/NG	G/NG1.1	The first version of framework complete, verified and validated for simple geometries

		Go/NG	G/NG1.2	Two optimal designs for different PCM HX applications
2	Update framework, generate reduced order performance map (ROMs) and test the integration in building simulation tools	Milestone	2.1	Two ultra-performance PCM-HX design completed
2	Fabricate the PCM-HXs (P1 and P2) developed in 2.1	Milestone	2.2	PCM-HXs P1 and P2 fabricated
2	Develop Web/Desktop UI that incorporates the reduced order models	Milestone	2.3	First version of ROMs published
2	Complete performance tests on prototypes	Milestone	2.4	PCM-HX P1 and P2 performance measured and the framework is validated by those data
		Go/NG	G/NG2.1	First version of the tool released to select users
		Go/NG	G/NG2.2	Ultra-performing PCM-HXs design completed and ready for fabrication
		Go/NG	G/NG2.3	The second version of framework passes validation
3	Fabricate and test the two HXs (P3 and P4) and validate the model			
3	Second round of Performance map generation and integrate with UI	Milestone	3.2	the second version of ROMs published
3	Final framework complete. and documentation delivery	Milestone	3.3	Design Framework and other related documentation delivered. ROMs made available to design community through appropriate publication medium.

Project Discussion and Results

PCM-HX Modeling, Analysis and Optimization (M1.4; M2.1; M2.2; M2.3; M2.4; M3.2)

Note: The contents of this section have been published in the following citations: Bacellar et al. [136]*; Bacellar et al.* [137]*; Alam et al.* [138]*; Alam et al.* [139]*; Alam et al.* [140]*; Alam et al.* [141]*; Alam et al.* [142]*; Menezes et al.* [143]

The modeling efforts for this project are listed below. A detailed report on each effort is included in the following section.

- (M1.4; M2.1; M2.2; M2.4) Development of reduced order models (ROMs), update framework and generate performance maps and test the integration in building simulation tools
- (M2.3) Develop Web/Desktop UI that incorporates the reduced order models (i) Integration of Resistance-Capacitance Model into Web/Desktop UI
- (M3.2) Second round of Performance map generation and integrate with UI (i) Integration of Generalized Resistance-Capacitance Model into Web/Desktop UI

CFD Modeling: Effect of Thermophysical Properties on PCM-HX Simulation (M1.4)

Introduction, CFD Modeling, & PCM Thermophysical Properties

A CFD study was conducted to assess the impact of thermal expansion coefficient (β), viscosity (μ), and melting temperature range (MR) on the charging (melting) operation for PCM-HX with and without fins. A straight tube PCM-HX was investigated (Figure 9a), and RT35 was used as PCM. Values for the thermophysical properties were taken from Pu et al. [144] and Longeon et al. [20]. The model was validated based on experimental data conducted by [20]. It can be observed from Figure 9b that the results of the numerical model for melting agree well with the experiment which validates our model.

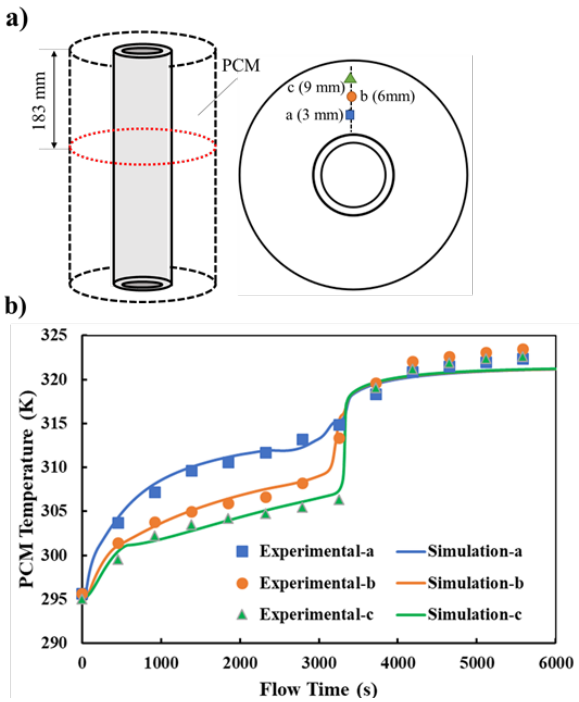

Figure 9: a) Thermocouple locations from experiment [20] b) Numerical melting model validation based on pcm local temperature profile from experiment

However, using thermophysical data from Ebadai et al. [145], the model would have not been validated as well as it did when data from Pu et al. [144] was used since there is significant difference between the thermophysical data of PCM reported in these two sources, as can be seen in Table 8. There is always uncertainty involved when reliable source for a thermophysical data is not present and the range of that uncertainty needs to be studied. Unlike non-finned domains, the PCM flow can get obstructed in the finned which reduces the natural convection. As the latter also depends on thermophysical properties, it is necessary to check if there is any difference in the impact of the thermophysical properties.

Table 8: Properties of PCM RT35 from different sources

Source	β (1/K)	μ (kg/m-s)	Lit. Source	Exp./ Calc. Procedure	Latent Heat (kJ/kg)
Pu et al. [23]	0.001	0.0029	Y	N	157
Longeon et al. [20]	0.001	0.0027	N	N	157
Ebadi et al. [145]	0.0006	0.023	Y	N	160
Rahimi et al. [146]	0.0006	NA	N	N	170
Manufacturer Datasheet [31]	NA	NA	-	-	160

Both computational domains are 2D axisymmetric. The non-finned domain is a 40 mm x 15 mm rectangular section, while the finned one is a part of the annular finned PCM-HX. It has been shown by Bacellar et al. [31] that for structured surface with fins, reduced domains reproduces the same behavior as full domain at approximately half the computational cost. The annular fins have a diameter of 70 mm, thickness of 4 mm, and fin pitch of 15 mm. The ratio between fin pitch and diameter is less than 0.25, which can

be considered as small fin pitch. The finless domain may be considered a case with very large fin pitch; therefore, we are addressing both extremes. Both the tube and the fin are copper.

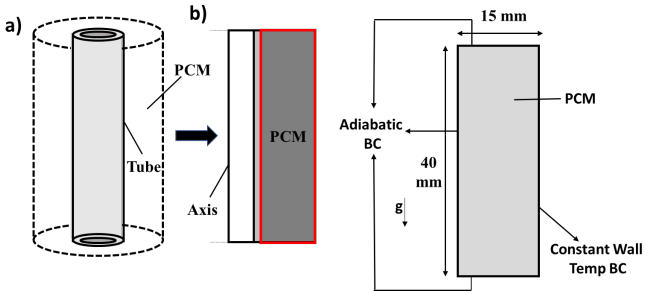

Figure 10: Non-finned domain a) physical model b) computational domain

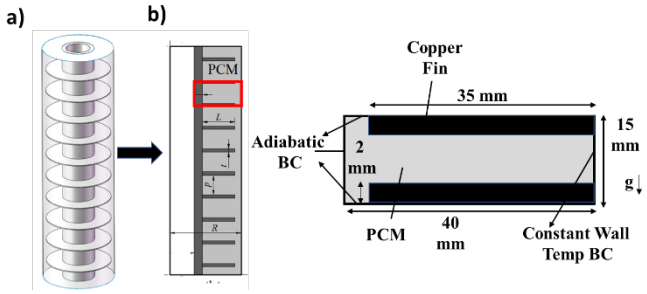

Figure 11: Finned domain a) physical model b) computational domain

Both models have constant temperature boundary condition on the tube wall. The wall temperature for this study was 100°C but other wall temperatures were used in a separate study presented at a later subsection in this manuscript to verify consistency in the results. All the other walls in the domain were set as adiabatic. The initial temperature for the simulation was 26°C. Natural convection is taken into consideration during PCM melting process using Boussinesq approximation. The flow of liquid PCM is considered laminar since viscous forces play a major role as it will be discussed further. Structured rectangular grids are used to discretize the computational domain, and a time step size of 0.1s was used [144]. General CFD settings used in this work are presented in Table 9.

Table 9: CFD Settings

Settings	Value(s)
Pressure-Velocity Coupling	SIMPLE
Pressure Disc. Scheme	PRESTO!
Momentum Disc. Scheme	QUICK
x-vel. Convergence Criteria	10^{-5}
y-vel. Convergence Criteria	10^{-5}
Energy Convergence Criteria	10^{-12}

Max Iterations per Time Step	100
Mushy Zone Parameter	10^6

A parametric study consisting of a combination of threes values of β, μ and melting range, was conducted. Two values of β were taken from the literature and using an equation from Schimmelpfennig et al. [147], a third value for β was estimated, as can be seen in Table 10. The equation requires the density of liquid PCM in two different temperatures, however, from the manufacturer provided data there are only density of PCM in two different phases.

Table 10: Thermophysical properties of RT35

Constant value properties				
Property	**Units**	**Method**	**Value(s)**	
Density	kg/m^3	Boussinesq	880	
Specific Heat	kJ/kg-K	PiecewiseLinear	1.8(solid)/2.4(liquid)	
Thermal Conductivity	W/m-K	Constant	0.2	
Latent Heat	kJ/kg	Constant	157	
Properties for sensitivity analysis				
β (1/K)	**Ref.**	**μ (kg/m-s)**	**Ref.**	**MeltingRange (°C)**
0.0006	[145]	0.0029	[148]	28-40
0.001	[148]	0.01295	-	30-38
0.0026	[147]	0.023	[145]	32-36

Using these density values, β is likely to be overestimated since the expansion only occurs, in practice, in the liquid phase. Two of the values of μ are taken from the literature and the third is the average of the two. Three melting ranges with a nominal melting temperature of 34°C were considered. The remaining thermophysical properties were taken from Pu et al. [144].

Results: Effect of Thermal Expansion Coefficient

For each μ and melting range values while parameterizing β resulted in 27 cases for each non-finned and finned domain. The results are summarized in Table 11.

Table 11: Effect of Thermal Expansion Coefficient in Melting Time

Case No.	MR (°C)	μ (kg/m-s)	β (1/K)	Non-Finned Melting Time (s)	Dev (%)	Finned Melting Time (s)	Dev (%)
1	28-40	0.0029	0.0006	532	*	231	*
4			0.001	465	-12.6	204	-11.7
7			0.0026	356	-33.1	174	-24.7
2		0.01295	0.0006	707	*	290	*
5			0.001	628	-11.2	260	-10.3
8			0.0026	492	-30.4	210	-27.6
3		0.023	0.0006	795	*	321	*
6			0.001	703	-11.6	286	-10.9
9			0.0026	553	-30.4	230	-28.3
10	30-38	0.0029	0.0006	530	*	229	*
13			0.001	464	-12.5	202	-11.8
16			0.0026	354	-33.2	173	-24.5
11		0.01295	0.0006	715	*	291	*
14			0.001	634	-11.3	260	-10.7
17			0.0026	497	-30.5	209	-28.2
12		0.023	0.0006	795	*	323	*
15			0.001	709	-10.8	288	-10.8

18			0.0026	561	-29.4	234	-27.6
19	32-36	0.0029	0.0006	528	*	227	*
22			0.001	460	-12.9	200	-11.9
25			0.0026	352	-33.3	172	-24.2
20		0.01295	0.0006	727	*	294	*
23			0.001	644	-11.4	264	-10.2
26			0.0026	502	-30.9	210	-28.6
21		0.023	0.0006	794	*	328	*
24			0.001	725	-8.7	293	-10.7
27			0.0026	573	-27.8	236	-28.0

The variation in the thermal expansion coefficient (β) significantly influences the melting rate across all tested cases. For every combination of dynamic viscosity (μ) and melting range, the deviation caused by increasing β follows a similar trend. A higher value of β enhances the volumetric expansion of the liquid PCM, thereby intensifying natural convection and accelerating the melting process. However, when comparing finned and non-finned domains, the impact of increasing β on melting behavior remains similar in most cases. Notable exceptions include Cases 7, 16, and 25, where the lowest μ and highest β values were used, leading to the strongest natural convection effects. As shown in Table 11**,** these cases also correspond to the shortest melting times. In the finned domain, however, the presence of fins partially obstructs the flow of liquid PCM, reducing the influence of natural convection. As a result, the enhanced convection effects observed in the non-finned cases are not fully realized in the finned geometry, leading to noticeable deviations between the two configurations for these particular cases.

Figure 12 presents the average PCM temperature profiles for selected cases in both finned and non-finned domains. In the non-finned domain, increasing β results in more pronounced temperature deviations compared to the finned configuration. Since temperature profiles are often used to validate numerical models against experimental data, this figure highlights the importance of using accurate β values for model validation, particularly in non-finned geometries, where natural convection plays a more significant role. Furthermore, local temperature deviations caused by inaccurate β values can be much greater than what is reflected in the average temperature. The figure also indicates the corresponding liquid fraction at which the temperature profile begins to diverge. In the non-finned domain, this deviation occurs relatively early during the melting process, whereas in the finned domain, it appears closer to the end of melting. This is because conduction dominates heat transfer near the fin surfaces, rendering the effect of β less significant in those regions.

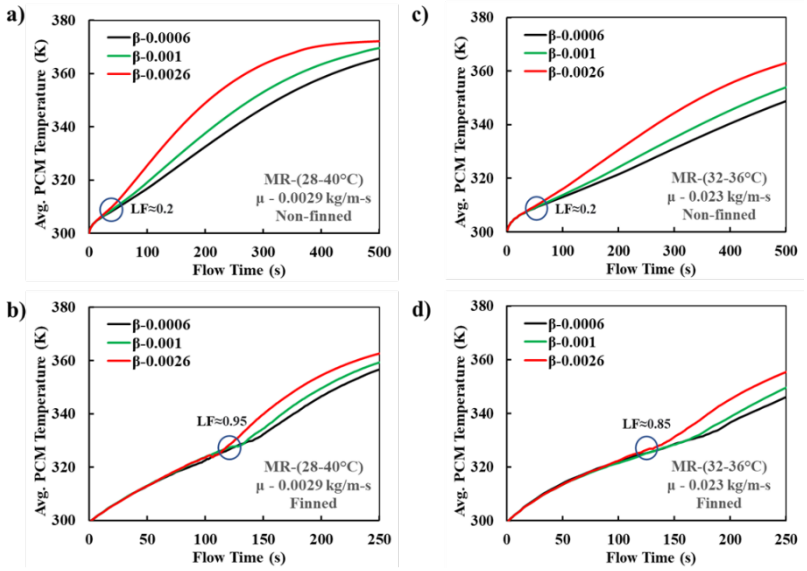

Figure 12: Effect of Thermal Expansion Coefficient in Average PCM Temperature Profile, For Case (1,4,7) A) Non-Finned B) Finned; For Case (21,24,27) C) Non-Finned D) Finned

Results: Effect of Viscosity

Table 12 summarizes the results from the 27 cases and shows the impact of changing viscosity with different values of β and melting range. The case studies are same as Table 11 but this table is presented in a way to visualize the effects of viscosity.

Table 12: Effect of Viscosity in Melting Time

Case No.	MR (°C)	β (1/K)	μ (kg/m-s)	Non-Finned Melting Time (s)	Dev (%)	Finned Melting Time (s)	Dev (%)
1	28-40	0.0006	0.0029	532	-	231	-
2			0.01295	707	32.9	290	25.5
3			0.023	795	49.4	321	39.0
4		0.001	0.0029	465	-	204	-
5			0.01295	628	35.1	260	27.5
6			0.023	703	51.2	286	40.2
7		0.0026	0.0029	356	-	174	-
8			0.01295	492	38.2	210	20.7
9			0.023	553	55.3	230	32.2
10	30-38	0.0006	0.0029	530	-	229	-
11			0.01295	715	34.9	291	27.1
12			0.023	795	50.0	323	41.0
13		0.001	0.0029	464	-	202	-
14			0.01295	634	36.6	260	28.7
15			0.023	709	52.8	288	42.6
16		0.0026	0.0029	354	-	173	-
17			0.01295	497	40.4	209	20.8
18			0.023	561	58.5	234	35.3
19	32-36	0.0006	0.0029	528	-	227	-
20			0.01295	727	37.7	294	29.5
21			0.023	794	50.4	328	44.5
22		0.001	0.0029	460	-	200	-

23			0.01295	644	40.0	264	32.0
24			0.023	725	57.6	293	46.5
25		0.0026	0.0029	352	-	172	-
26			0.01295	502	42.6	210	22.1
27			0.023	573	62.8	236	37.2

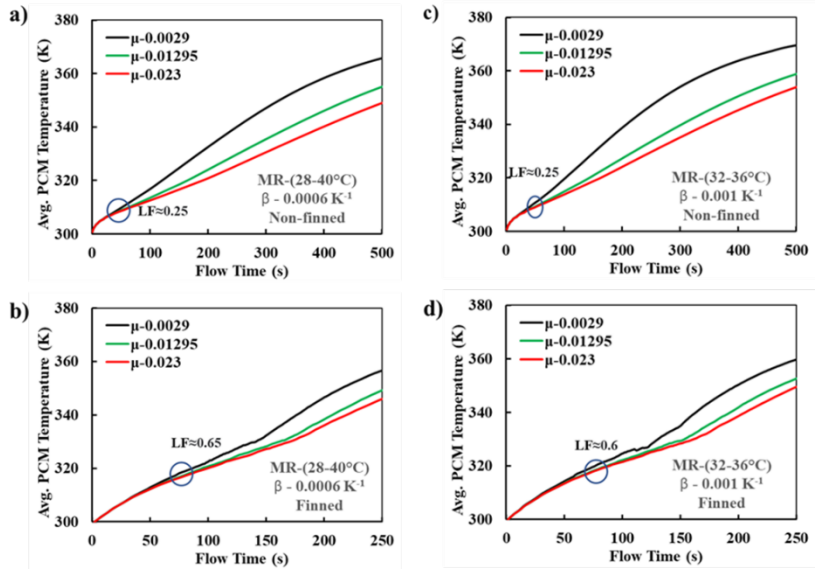

Figure 13: Effect of Viscosity in Average PCM Temperature Profile, For Case (1,2,3) A) Non-Finned B) Finned; For Case (22,23,24)°C) Non-Finned D) Finned

A variation in μ can significantly impact the melting rate in all the cases. When the viscosity is increased, the flow of the liquid PCM is also increased and thus reducing the natural convection and increasing the melting time. The deviation due to change in μ is higher compared to the previous section when we changed β. This can happen because the magnitude of difference between the three values were higher for viscosity.

Unlike the previous section, here the impact on finned cases is significantly lower compared to the non-finned cases. This can be explained by the fact that the fins impose a flow resistance reducing the freedom of motion of the liquid PCM, therefore minimizing the buoyancy effects. From the table it can also be seen that, for higher value of β, the deviation between the melting time increases compared to the lower values.

Figure 13 shows the average PCM temperature profile for some sample cases for finned and non-finned domain when different values of μ are used. Like in the previous section, for the non-finned domain, the temperature deviation is higher than the finned cases. However, unlike in the previous section, the deviation of temperature does not start at the end of the melting process, rather it starts in the middle of the process. The lower viscosity reduces flow resistance allowing the liquid PCM to move more freely, thus contributing to an enhanced heat transfer as supported by the higher temperature values observed.

Results: Effect of Melting Range

Table 13 summarizes the results from the 27 cases and shows the impact of changing MR with different values of β and μ. The table shows that change in MR did not significantly impact the melting time for any of the cases for both finned and non-finned

domain. This finding can be useful as it can lead to less uncertainty while performing future CFD simulation tasks by not requiring the accurate knowledge of PCM MR.

Table 13: Effects of Melting Range

Case No.	β (1/K)	μ (kg/m-s)	MR (°C)	Non-Finned Melting Time (s)	Dev (%)	Finned Melting Time (s)	Dev (%)
1	0.0006	0.0029	28-40	532	-	231	-
10			30-38	530	-0.4	229	-0.9
19			32-36	528	-0.8	227	-1.7
2		0.01295	28-40	707	-	290	-
11			30-38	715	1.1	291	0.3
20			32-36	727	2.8	294	1.4
3		0.023	28-40	795	-	321	-
12			30-38	795	0.0	323	0.6
21			32-36	794	-0.1	328	2.2
4	0.001	0.0029	28-40	465	-	204	-
13			30-38	464	-0.2	202	-1.0
22			32-36	460	-1.1	200	-2.0
5		0.01295	28-40	628	-	260	-
14			30-38	634	1.0	260	0.0
23			32-36	644	2.5	264	1.5
6		0.023	28-40	703	-	286	-
15			30-38	709	0.9	288	0.7
24			32-36	725	3.1	293	2.4
7	0.0026	0.0029	28-40	356	-	174	-
16			30-38	354	-0.6	173	-0.6
25			32-36	352	-1.1	172	-1.1
8		0.01295	28-40	492	-	210	-
17			30-38	497	1.0	209	-0.5
26			32-36	502	2.0	210	0.0
9		0.023	28-40	553	0.0	230	0.0
18			30-38	561	1.4	234	1.7
27			32-36	573	3.6	236	2.6

Figure 14 shows the average PCM temperature profile for some sample cases for finned and non-finned domains with minimal deviation among the different MR's. This, however, may have been masked by the fact that a large temperature difference was used. The next section presents a more detailed analysis introducing the effect of temperature potential.

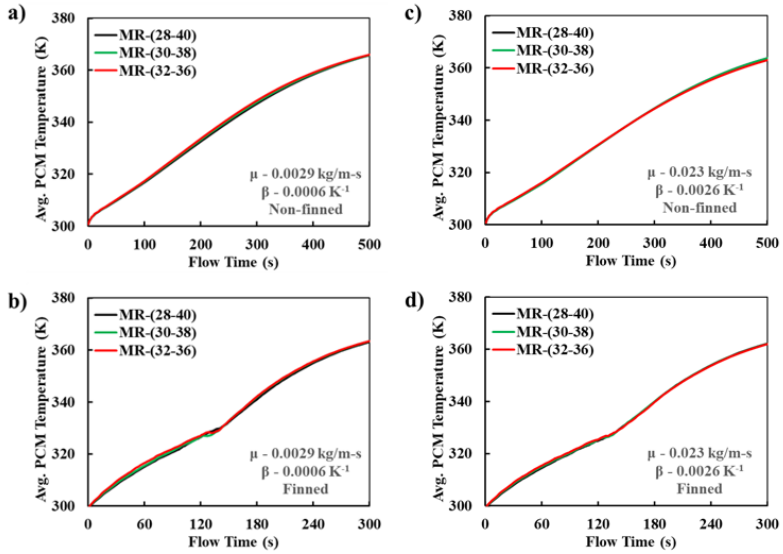

Figure 14: Effect of MR in Average PCM Temperature Profile, For Case (1,2,3) A) Non-Finned B) Finned; For Case (22,23,24) C) Non-Finned D) Finned

Effects of Wall Temperature

Based on the literature, a wall temperature of 100 °C is considered relatively high. To assess the influence of lower driving temperatures, additional simulations were conducted for the finned domain using reduced wall temperatures. Table 14 summarizes the results for both high and low wall temperatures across different values of β and μ. The results indicate that lowering the wall temperature had minimal impact on the trends associated with β variations but significantly influenced the system's sensitivity to μ. Specifically, at lower wall temperatures, the melting time became less sensitive to changes in μ. This suggests that reducing the approach temperature decreases the relative influence of viscous forces more than buoyancy forces.

It is important to note that this analysis was confined to finned domains, where PCM flow is more restricted. In non-finned configurations, where natural convection plays a larger role, different behavior may be observed. Overall, as the temperature gradient decreases, the influence of viscous effects on the thermal response diminishes, highlighting the complex interplay between thermal and fluid dynamic properties in PCM-based systems.

Table 14: Effect of Wall Temperature in Melting Rate Deviation

Case No.	MR (°C)	μ (kg/m-s)	β (1/K)	Wall Temp-45°C		Wall Temp-100 °C	
				Melting Time (s)	Dev (%)	Melting Time (s)	Dev (%)
1	28-40	0.0029	0.0006	1327	--	231	-
4			0.001	1180	-11	204	-12
7			0.0026	982	-25.9	174	-24.7
4	28-40	0.0029	0.001	1180	-	204	-
5		0.01295		1383	17.2	260	27.5
6		0.023		1478	25.2	286	40.2

Table 15 summarizes the result for effect of three different wall temperature in the impact for change in melting range. The result shows that for both the high and medium wall temperature, change in melting rate do not have any effect in the melting time. However, for the low wall temperature the deviation in melting time is significant. This shows that when the temperature difference between the heat source and the nominal temperature of PCM is close, the selection of melting range becomes significant.

Table 15: Effect of Wall Temperature in Melting Rate Deviation Caused by Different Melting Ranges

μ-0.0029 (kg/m-s) β -0.001 (1/K)		Wall Temp-45°C		Wall Temp-65°C		Wall Temp-100 °C	
CaseNo.	MR(°C)	Melting Time(s)	Dev(%)	Melting Time(s)	Dev(%)	Melting Time(s)	Dev(%)
4	28-40	1180	-	408	-	204	-
13	30-38	1102	-6.6	402	-1.5	202	-1
22	32-36	1065	-9.8	403	-1.2	200	-2

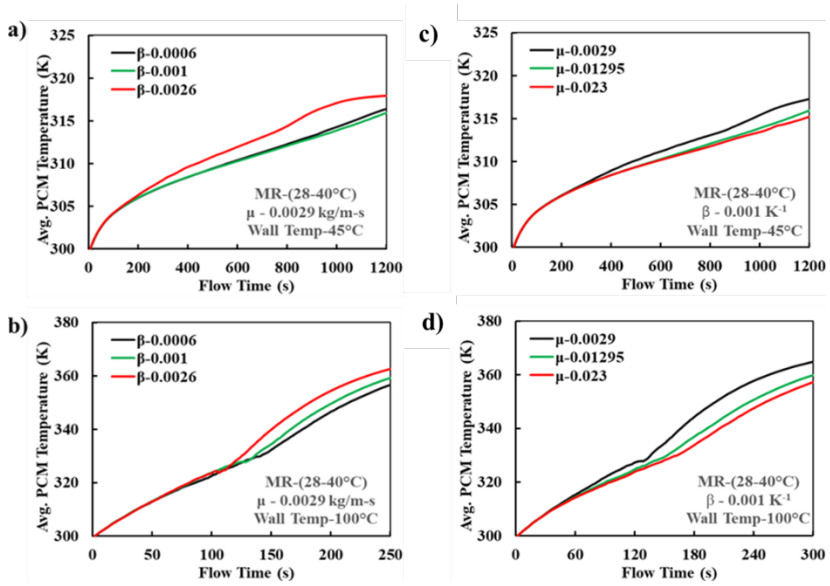

Figure 15: a), b) Effect of Wall Temperature in Deviation Caused by Thermal Expansion Coefficient, For Case (1,4,7); c), d) Effect of Wall Temperature in Deviation Caused by Viscosity, For Case (4,5,6)

Figure 15 shows the effect of wall temperature in the PCM temperature profile deviation caused by different values of β and μ respectively. For the higher wall temperature, effect of change of μ is higher than the lower wall temperature. The change in values for β and μ showed a significant impact on the melting time prediction. Using different μ and β values from literature resulted in a deviation of up to 57.6% and 12.9% respectively for the non-finned domain. For the finned domain, the effect of μ is comparatively lower (46.5%) while the effect of β is found similar (11.9%) when compared to the non-finned domain.

The study highlights the challenges imposed by the inaccurate knowledge of μ and β for accurate prediction of PCM-HX temperature profile and melting time with CFD. β and μ are part of the momentum source term in the momentum equation solved in CFD and is required to model the transition between solid and liquid phase. For the simulation of

different PCMs available in the market, CFD can be restrictive. In this work for rapid simulation tool and optimization framework development, focus was given on geometries where the momentum equations are not required to be solved and thus simplified model like RCM can be created for the accurate prediction in PCM-HX.

CFD Modeling: FEM-CFD

As described previously, most CFD simulations account for phase change and natural convection, which is computationally expensive and time consuming. Therefore, a CFD model was developed, FEM-CFD, which considers the phase change process (melting / solidification) by replacing the PCM with an equivalent solid-only material with equivalent specific heat as taken from measured DSC data. The model was (i) verified against full CFD simulations and (ii) validated against experimental data from three cyclic tests. The FEM-CFD model provided a good prediction of average PCM temperature and water outlet temperature when compared to the experimental result, however the computational speed-up was still not sufficient for design optimization.

CFD Model Description

The CFD model is described in Figure 16, and it is similar to what have been done in the annular fin validation using RCM. The model assumes a vertical upward fluid flow, fluid flow turbulence modeling. All CFD runs are conducted using Ansys® Fluent 2021R2 [149].

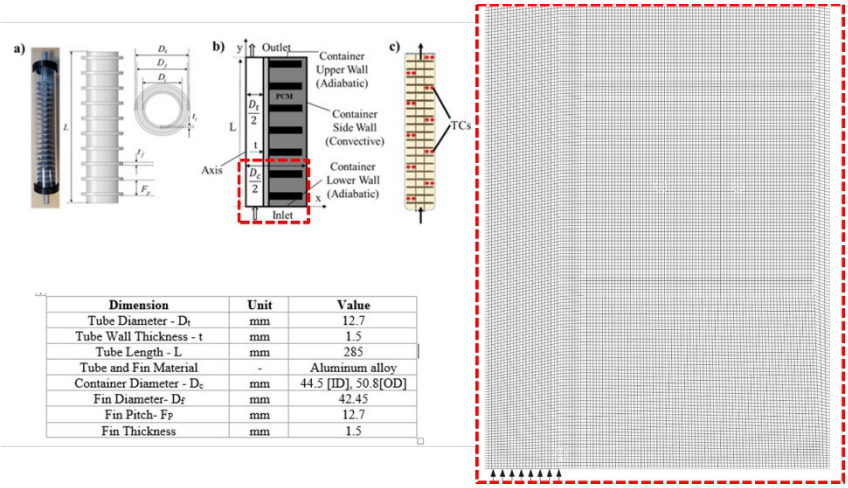

Dimension	Unit	Value
Tube Diameter - D_t	mm	12.7
Tube Wall Thickness - t	mm	1.5
Tube Length - L	mm	285
Tube and Fin Material	-	Aluminum alloy
Container Diameter - D_c	mm	44.5 [ID], 50.8[OD]
Fin Diameter- D_f	mm	42.45
Fin Pitch- F_P	mm	12.7
Fin Thickness	mm	1.5

Figure 16: CFD Model: (Top Left) PCM-HX Schematic Diagrams; (Bottom Left) PCM-HX Dimensions; (Right) Zoom-In of Mesh (near heat transfer fluid inlet).

Treatment of PCM in FEM-CFD

The FEM-CFD model treats the PCM as a solid-only material with specific heat calculated from DSC data, here RT-35, such that the phase change process is accounted for as a temperature-dependent thermophysical property change in the PCM material. Because the PCM is treated as a solid (i.e., phase change and fluid motion not considered), the PCM portion becomes a finite element model (FEM) where conduction is the only mode of heat transfer. Since the model still solves for the heat transfer and fluid flow in the HTF

portion of the PCM-HX (here, water), the new model is termed the “FEM-CFD model” since it combines FEM (for PCM) and CFD (for the HTF).

The FEM-CFD model requires the PCM specific heat to be provided as a function of temperature. This is accomplished by extracting the PCM specific heat from measured DSC data. The process is described below:

1. Digitize DSC data from third-party vendor (Figure 17).
2. Denormalize the specific heat using Equation (4) across the PCM melting range (28°C ≤ T ≤ 35°C) while ensuring the PCM latent heat was the same as the DSC data.
3. Fit the (denormalized) specific heat using a third order polynomial (Equation (5)) across the PCM melting range.
4. Compute the PCM latent heat using the specific heat curve fit to ensure the total energy storage is close to the given DSC data.

A comparison of the PCM latent heat from different sources (DSC, previous full CFD run, digitized DSC, and new curve fit) are summarized in Table 16. It is clear that the denormalization and curve fitting process produced an acceptable approximation of the total PCM latent heat and could be used in future models as well (CFD, RCM, etc.). Additionally, the specific heat denormalization and curve fitting process could be applied to other PCMs, provided the DSC data is available.

$$c_p = c_{p,DSC,Norm} \cdot \frac{\int_{T_s}^{T_l} c_{p,DSC,Norm}\, dT}{h_{lf,DSC,Norm,Given}} \tag{4}$$

$$c_p(T) = AT^3 + BT^2 + CT + D \tag{5}$$

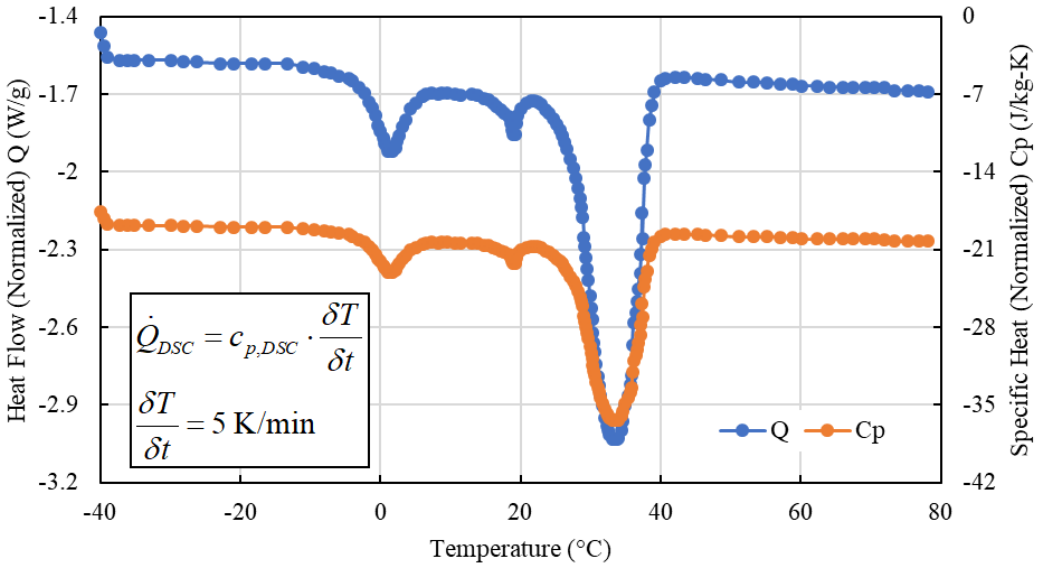

Figure 17: Third Party Digitized DSC Data for RT-35.

Table 16: PCM Latent Heat from DSC Data.

Data Source	h_{lf}	% Error	Notes
[-]	[kJ/kg]	[-]	-
DSC (Given)	138.52	REF	26.72°C ≤ T ≤ 41°C
Diarce et al. [2]	135	-2.54%	Used for full CFD run 28°C ≤ T ≤ 35°C
DSC (Digitized) $h_{lf,DSC} = \int_{T_s}^{T_l} c_{p,DSC} dT$	133	-3.98%	Denormalized 28°C ≤ T ≤ 35°C
New Curve Fit $h_{lf,DSC} = \int_{T_s}^{T_l} c_{p,CurveFit}(T) dT$	138.18	-0.25%	Third order polynomial 28°C ≤ T ≤ 35°C

Figure 18 presents a comparison of the specific heat from the previous full CFD runs, the digitized DSC data, and the new curve fit. The jump discontinuity results due to the phase change, where the specific heat significantly increases (about one order of magnitude). Within the Ansys® Fluent [149] environment, the specific heat is implemented as a piecewise polynomial (Equation (6)). Note that Ansys® Fluent [149] utilizes internal smoothing methods in the transition region between polynomials.

$$\begin{aligned} T < T_s \quad & c_p = 1800 \text{ J/kg} \cdot \text{K} \\ T_s < T < T_l \quad & c_p(T) = AT^3 + BT^2 + CT + D \\ T < T_l \quad & c_p = 2400 \text{ J/kg} \cdot \text{K} \\ T_s = 28°\text{C}, \quad & \text{T}_l = 35°\text{C} \end{aligned} \tag{6}$$

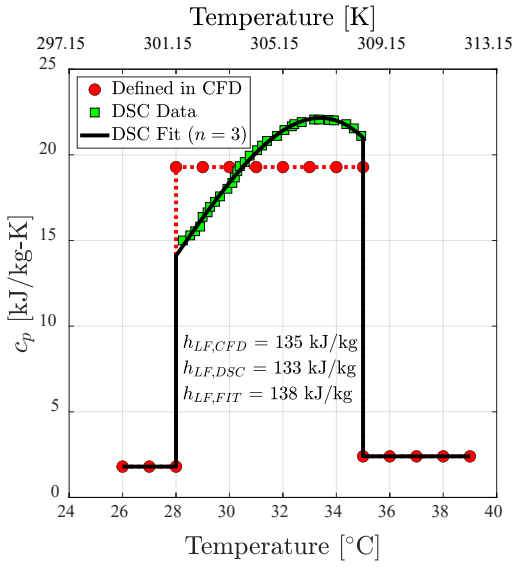

Figure 18: Specific Heat Comparison: Full CFD vs. Digitized DSC Data vs. Curve Fit.

Experimental Validation & Computational Time Improvements

The FEM-CFD model was simulated for three cyclic cases Table 17, and the water temperature (Table 18, Figure 19) and average PCM temperature (Table 19, Figure 20)

from each case were compared from (i) experiments, (ii) full CFD, and (iii) RCM. It is clear that the FEM-CFD model gives comparable accuracy to the full CFD model. One main deviation which warrants discussion is that the RCM and FEM-CFD model both consistently underpredict the experimental maximum average PCM temperature, which occurs during the melting process. One potential explanation for this is that both the RCM and FEM-CFD model do not consider natural convection in the PCM, which would result in national convection currents which would bring lower temperature (liquid) PCM closer to the heat transfer surface(s) (tube + fins) to be heated. This would result in higher average PCM temperature since more liquid PCM could be heated faster. However, during the solidification process, the temperature agreement is very good across all models. Previous discussion in past reports mentioned that PCM solidification process is dominated by conduction, which is exactly the physics considered by the FEM-CFD and RCM, and thus the temperature predictions in this PCM regime should be better than in the melting region, which is clear.

Table 17: PCM-HX Cyclic Tests Conditions for Validation.

Case	Nominal Inlet Water Mass Flow Rate	Nominal Inlet Water Temperature During Melting
[-]	[g/s]	[°C]
1	2.5	44.5
2		49.5
3		54.5

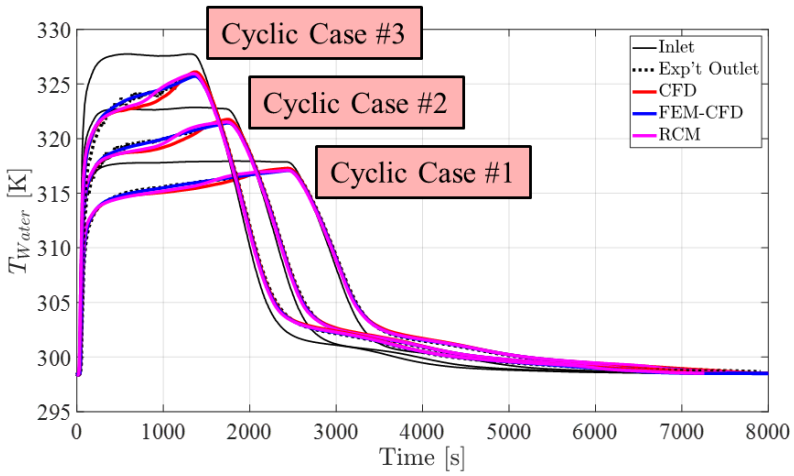

Figure 19: Water Temperature Experimental Validation: Full CFD, FEM-CFD, RCM.

Table 18: Water Temperature Experimental Validation Statistics.

	Case #1			Case #2			Case #3		
Model	Mean Abs Err	Max Err	RMSE	Mean Abs Err	Max Err	RMSE	Mean Abs Err	Max Err	RMSE
[-]	[K]	[K]	[K]	[K]	[K]	[K]	[K]	[K]	[K]
CFD	0.1796	+2.2260	0.2664	0.2107	+3.2324	0.3542	0.2284	+4.2280	0.4539
FEM-CFD	0.1163	+2.2352	0.1965	0.1486	+3.2511	0.2782	0.1981	+4.2442	0.4145
RCM	0.2028	+4.3420	0.3592	0.2442	+5.6688	0.4805	0.2832	+7.2663	0.6313

Finally, the computational speed of the new FEM-CFD model was compared to the full CFD model, and the results are shown in Table 20. Compared to a full CFD model (with

phase change, natural convection), the FEM-CFD model (without phase change, natural convection) showed similar accuracy while offering approximately 36% speed-up. However, the speed-up is not sufficient to enable optimization with FEM-CFD, where the optimization algorithm would require hundreds (thousands, or more) of simulations for a single optimization run.

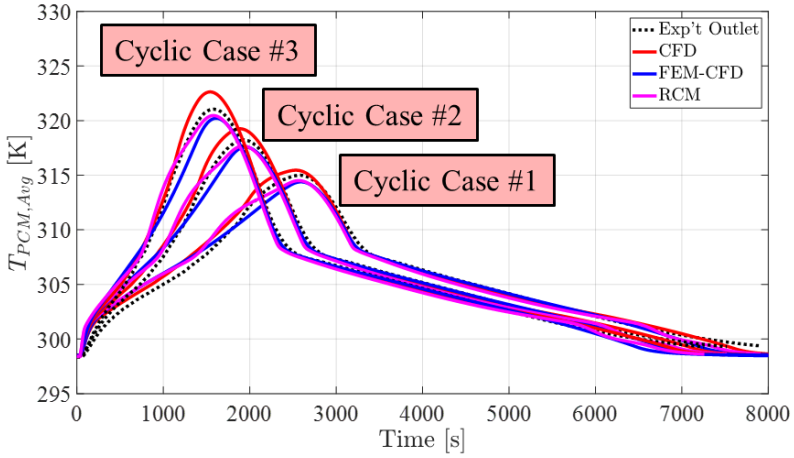

Figure 20: Average PCM Temperature Experimental Validation: Full CFD, FEM-CFD, RCM.

Table 19: Average PCM Temperature Experimental Validation Statistics.

	Case #1			Case #2			Case #3		
Model	**Mean Abs Err**	**Max Err**	**RMSE**	**Mean Abs Err**	**Max Err**	**RMSE**	**Mean Abs Err**	**Max Err**	**RMSE**
[-]	**[K]**	**[K]**	**[K]**	**[K]**	**[K]**	**[K]**	**[K]**	**[K]**	**[K]**
CFD	0.4325	+1.5442	0.5491	0.4525	+1.4736	0.5928	0.4461	+1.8794	0.6195
FEM-CFD	0.4717	+1.6878	0.6412	0.4563	+1.65501	0.6502	0.4806	+2.0723	0.7109
RCM	0.5724	+2.1106	0.6986	0.5574	+2.1007	0.6954	0.5167	+2.2937	0.6546

Table 20: Computational Speed Analysis: FEM-CFD vs. Full CFD.

Model	**Simulation Time**	**Speedup Ratio t_{REF} / t_{MODEL}**	**PC Hardware**
[-]	**[hr]**	**[-]**	**[-]**
Full CFD	8.70	REF	Intel® Xeon® Gold 6242R CPU @ 3.10GHz 3.09 GHz (2 processors) 256 GB RAM 32 parallel processes
FEM-CFD	6.38	1.364	

Resistance-Capacitance Model Development (M2.1, M2.3, M2.4))

Introduction

Resistance-Capacitance models (RCMs) have recently gained popularity for evaluating PCM-HX performance with acceptable computational cost. Compared to CFD, RCMs can accurately predict PCM-HX thermal-hydraulic performance with lower computational cost

by assuming conduction as the main heat transfer mode, thus avoiding the need to solve for higher-order PCM-HX physics, e.g., natural convection during PCM melting. Neumann et al. (2021) developed an RCM for a plate heat exchanger where the outlet fluid and PCM temperature deviations compared to a finite-element model were 0.62 K and 0.85 K, respectively, with the benefit of a 20-30x computational reduction. An RCM for melting in periodic structure was developed and validated against experimental data by Alam et al. (2022), showing a mean temperature deviation range between 1.34 K to 2.81 K. The most important factor was the real-time factor (RTF) of the solver, which was on the order of 1E-04.

Summary of RCM Development

As part of this project, XX geometry-specific RCMs were developed (Table 21) for a wide variety of PCM-HX configurations, operating conditions, and working fluids. The reader is referred to the noted references for additional information on each particular study. For the sake of brevity, we include the details of one RCM development study pertaining to the optimization of a straight tube annular finned PCM-HX (noted with *** in Table 21). The prototyping and experimental validation efforts for this PCM-HX will be discussed in future chapters.

Table 21: Summary of RCM studies (with References)

Ref	PCM-HX Configuration	Source Data	Working Fluid(s)	Experimental Validation?
[140]	Rectangular PCM-HX with porous media	Literature	-	Y
[141]	PCM embedded in 3D periodic structure	University of Padua	-	Y
[139]	Straight tube PCM-HX	CEEE	Water	Y
Internal study (A)	Straight tube annular finned PCM-HX	CEEE	Water	Y
[142], [143]	Optimized straight tube annular finned PCM-HX***	CEEE	Water	Y
Internal Study (B)	Serpentine microchannel PCM-HX	CEEE	Water	Y

Optimization of an Annular Finned PCM for Domestic Hot Water Heater Application

A resistance-capacitance based model (RCM) was developed for an annular finned-tube PCM-HX. Compared to past RCM work by the authors [150], [151], the present work includes conjugate heat transfer with a single-phase heat transfer fluid on the tube-side. The model was integrated with a multi-objective genetic algorithm (MOGA) [152] for optimization targeting a U.S. DOE standard medium-usage DHW application [153]. Comprehensive experimental testing was conducted using a conventionally-manufactured proof-of-concept optimal PCM-HX prototype to validate the RCM. The overall approach is shown in Figure 21.

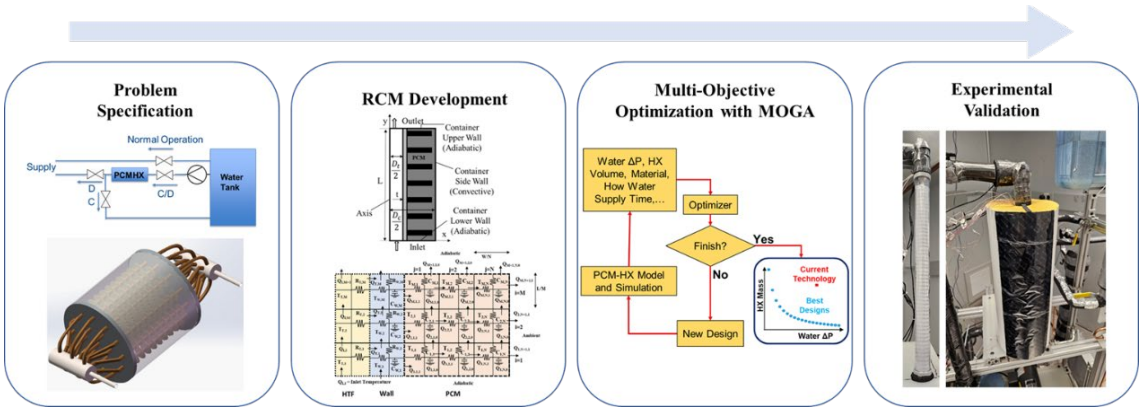

Figure 21: PCM-HX optimization approach.

Storage-type water heaters have a tendency for tank water temperatures to drop below the set-point during daytime operation. This requires the water be reheated above the set-point using (electrical) power input, which is undesirable during peak electricity consumption hours [154]. PCM-TES can be integrated into DHW heater systems to mitigate this issue. One such PCM-HX integration is illustrated in Figure 22(L) [155]. During peak periods (discharge (D) cycle in Figure 22(L)), the PCM-HX heats water before supply (PCM solidification), eliminating the need for heaters. The PCM-HX is charged (PCM melting) during off-peak hours using heaters. In this work, we consider a PCM-HX with straight tubes and annular fins (Figure 22(R)) which are connected in parallel while PCM occupies the remaining space in the tank.

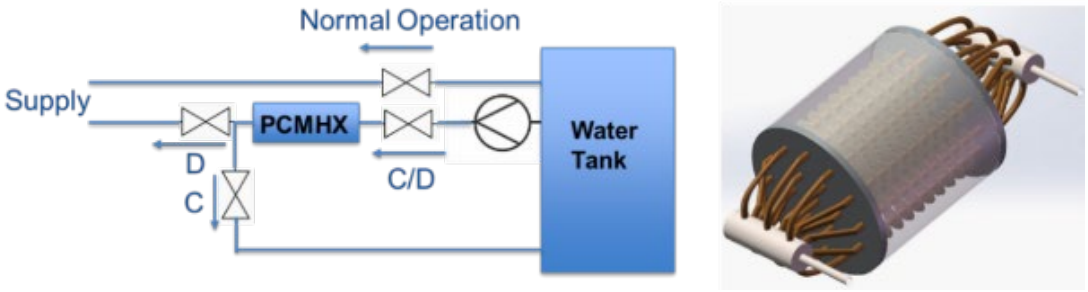

Figure 22: (Left) Operation diagram for PCM-HX integrated with domestic water heater system; (Right) Annular fin PCM-HX storage concept [155].

For effective heat extraction, the PCM must have a phase change temperature range sufficiently higher than the supply water temperature, which must meet or exceed 51.7°C as per the U.S. DOE standard [153]. However, selecting a PCM with an excessively high phase-change temperature may complicate the recharge cycle by increasing recharge time and energy input. Accordingly, the organic PCM RT62HC (RUBITHERM GmbH) was chosen. The thermophysical properties of the PCM and the aluminum tube/fins are outlined in Table 22. Assuming that 25% of total daily hot water consumption will be supplied by the TES, the system must continuously deliver water at 51.7°C for at least 540 seconds at a flow rate of 6.4 L/min [153]. The PCM-HX inlet water temperature was set to 46.7°C, considering a 5 K temperature drop during daytime operation due to heat

loss. The initial temperature of the fully charged (melted) PCM-HX was assumed to be 65.7°C.

Table 22: Thermophysical properties of materials.

Material	k (W/m-K)	ρ (kg/m^3)	c_p (J/kg-K)	T_{sol} - T_{melt} (°C)	ΔH (kJ/kg)
RT62HC	0.2	850 (solid), 840 (liquid)	2000	60-64	230
Aluminum Alloy	170	2670	890	-	-

RCMs are a lightweight alternative to computational fluid dynamics (CFD) for evaluating PCM-HX performance which simplify the computational requirements by not solving for higher-order physics. Instead, RCMs rely on approximations of thermal resistance to achieve accurate results at a fraction of the computational cost typically associated with CFD simulations [151]. In this study, an RCM was developed for a cylindrical PCM-HX with straight tubes and annular fins, where PCM fills the annular space. The annular tube-fin geometry (Figure 23(L)) involves conjugate heat transfer with a single-phase heat transfer fluid. Figure 23(R) represents the RCM thermal network, which will be discussed in more detail in subsequent sections.

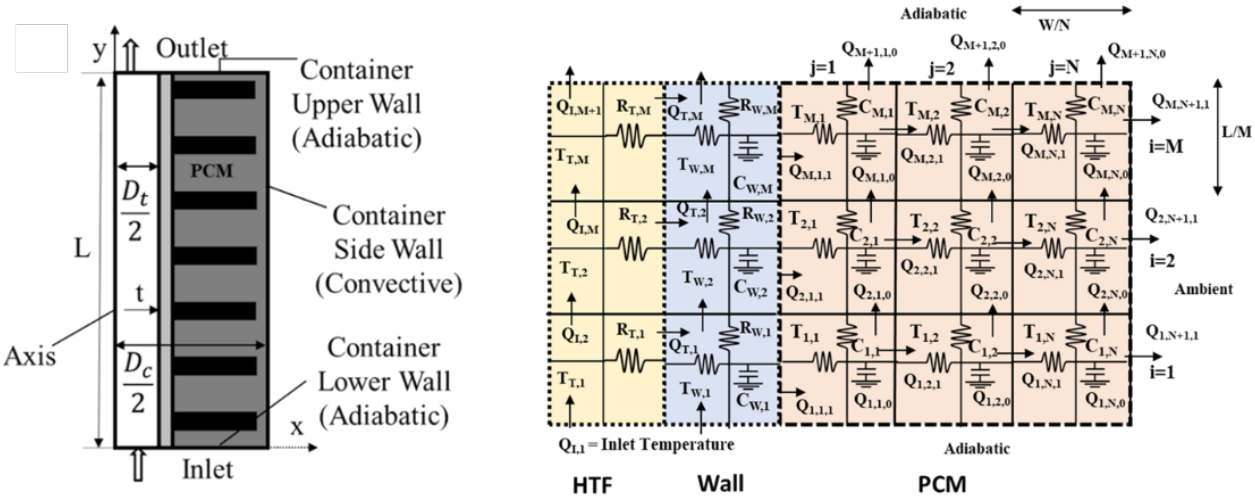

Figure 23: (Left) Computational domain of a cylindrical PCM-HX with straight tube with annular fins; (Right) Thermal network of 2D RCM for annular finned PCM-HX.

The general assumptions for the RCM are as follows. First, natural convection effects in the PCM are considered negligible, making the heat transfer conduction-dominated. Additionally, the properties of each segment are regarded as constant, and the entire segment can be described by a point at its center. When both PCM and fins are present within a segment, they are treated as a composite medium, with effective material properties calculated based on the volumes of PCM and fin material within that segment, as outlined by [151]. Moreover, the effect of contact resistance is ignored, ensuring a simplified calculation model. Additionally, no mass transfer occurs between segments, further simplifying the model and focusing purely on thermal properties. These assumptions help streamline the RCM for effective use in modeling and simulation.

Figure 23(R) depicts the thermal resistance-capacitance network for the annular tube-fin PCM-HX. The computational domain is segmented into three zones: (i) the heat transfer fluid (HTF) or “tube side”, (ii) the tube wall, and (iii) the PCM / fins zone. As noted in

Assumption 3, segments with both PCM and fins are treated as homogeneous segments with effective material properties determined based on the volumes of PCM/fin material present in that segment. The reader is referred to [151] for additional details on the non-uniform porosity calculation. The PCM and fin domain is discretized into equal-length segments in both the vertical and radial directions, while the tube and wall domains are discretized in the vertical direction only (i.e., one segment in the radial direction). Each segment has its own resistance and capacitance. Heat transfer between the tube and tube wall is calculated assuming laminar flow.

The time marching scheme is a first-order explicit Euler method to solve for the transient temperature profile in the PCM domain. The explicit time marching formulation for the annular finned PCM-HX is presented below. The tube-side thermal network parameters are calculated using Equations (7)-(10):

$$R_{T,i,t} = \frac{1}{h_W A_T} \quad (7) \qquad \dot{Q}_{T,i,t} = \frac{T_{T,i,t} - T_{W,i,t}}{R_{T,i,t}} \quad (8)$$

$$T_{T,i,t} = T_{W,in};\ i = 1 \quad (9) \qquad T_{T,i,t} = T_{T,i-1,t} - \frac{\dot{Q}_{T,i,t}}{\dot{m}_W c_{p,W}};\ i \geq 2 \quad (10)$$

The wall thermal network parameters are calculated using Equations (11)-(16)

$$R_{W,i,R} = \frac{Mln\frac{D_o}{D_i}}{2\pi L k_W} \quad (11) \qquad \dot{Q}_{W,i+1,t} = \frac{T_{W,i,t} - T_{W,i+1,t}}{R_{W,i,V}} \quad (12)$$

$$\dot{Q}_{P,i,0,t} = \frac{T_{W,i,t} - T_{i,0,t}}{R_{W,i,t,R}} \quad (13) \qquad \frac{dT_{W,i,t+1}}{dt} = \frac{\dot{Q}_{T,i,t} + \dot{Q}_{W,i,t} - \dot{Q}_{W,i+1,t} - \dot{Q}_{P,i,0,t}}{C_{W,i,t}} \quad (14)$$

$$T_{W,i,t+\Delta t} = T_{W,i,t} + \frac{dT_{W,i,t}}{dt} \cdot \Delta t \quad (15) \qquad R_{W,i,V} = \frac{L\ /\ M}{k_W \cdot A_W} \quad (16)$$

The PCM/fin domain thermal network parameters are calculated using Equations (17)-(24), and the RCM solver flowchart for the annular finned tube PCM-HX geometry is shown in Figure 24.

$$R_{P,i,j,R} = \begin{cases} \dfrac{Mln\ \frac{D_1}{D_0}}{2\pi L k_{eff}}; for\ i = 1 \\ \dfrac{Mln\ \frac{D_j}{D_{j-1}}}{2\pi L k_{eff}}; for\ i \geq 2 \end{cases} \quad (17) \qquad R_{P,i,j,V} = \frac{L/M}{k_{eff} \times A} \quad (18)$$

$$\dot{Q}_{i,j,t,0} = \begin{cases} 0 & ;for\ i = 1 \\ \dfrac{T_{i-1,j,t} - T_{i,j,t}}{R_{P,i,j,V}} & ;for\ i \geq 2 \end{cases} \quad (19) \qquad \dot{Q}_{i,j,t,1} = \begin{cases} \dfrac{T_{i,j,t} - T_{i,j+1,t}}{R_{P,i,j,V}} & ;for\ i \geq 1 \\ \dfrac{T_{i,N,t} - T_{amb}}{R_{P,i,j,V}} & ;for\ i = N \end{cases} \quad (20)$$

$$\frac{dT_{i,j,t}}{dt} = \frac{\dot{Q}_{i,j,t,0} + \dot{Q}_{i,j,t,1} - \dot{Q}_{i+1,j,t,0} - \dot{Q}_{i,j+1,t,1}}{C_{i,j,t}} \quad (21)$$

$$T_{i,j,t+1} = T_{i,j,t} + \frac{dT_{i,j,t}}{dt} \times \Delta t \quad (22)$$

$$C_{PCM} = \begin{cases} C_s; & T < T_s \\ Cs + \dfrac{\Delta H}{T_{melt} - T_{sol}}; & T_s \leq T \leq \\ C_l; & T > T_l \end{cases} \quad (23)$$

$$C_{i,j,t} = [\gamma\ C_{PCM}\ \rho_{PCM} + (1-\gamma)\ C_{FIN}\ \rho_{FIN}] \quad (24)$$

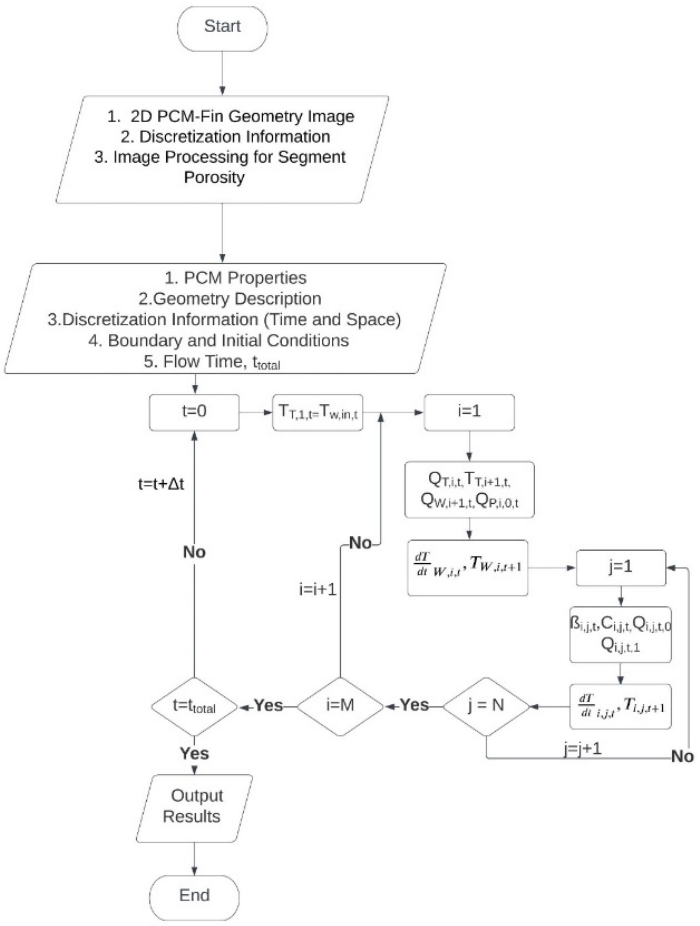

Figure 24: RCM solver flowchart for annular finned PCM-HX.

The low computational cost of RCM makes it suitable for optimization using a multi-objective genetic algorithm (MOGA) [152]. The overall objective is to design annular PCM-HXs to serve as a TES solution for mitigating heat loss from U.S. DOE standard medium-usage DHW heaters [153]. The objective functions are to minimize the water pressure drop and minimize the total material mass (tube + fin mass) of PCM-HX (Equation (25)).

$$\min \Delta P_{Water}, M_{HX,Material}$$
$$s.t. \quad (25)$$
$$t_{HW} \geq 540s; \qquad V_{HX,total} \leq 0.1 \cdot V_{tank,baseline}; \qquad -0.1 \leq SOC \leq 0.1$$

The baseline water heater tank volume was chosen based on a commercially-available electric water heater system. It was assumed that there is no heat loss to ambient. The design space is detailed in Table 23, where tube diameter, fin thickness, and container diameters are discrete variables based on the availability of off-the-shelf aluminum tubes, aluminum fins, and polycarbonate tubes. Additionally, two tube thicknesses were chosen. The continuous variables, fin pitch and tube length, are chosen based on previous experience with annular-fin PCM-HXs, and the number of parallel units is chosen to ensure the PCM-HX achieves the required capacity.

Table 23: Optimization design space.

Continuous Variables	**Lower Limit**	**Upper Limit**
Fin Pitch (mm), F_P	0.2 D_f	0.5D_f
Length (mm), L	300	700
Discrete Variables	**Values**	
Outer Tube Diameter (mm), D_t	15.87, 12.7, 9.52, 7.94 6.35,4.76 (t_t =0.89) 9.52, 6.35 (t_t =0.71)	
Fin Thickness (mm), t_f	0.81,0.63,0.41,0.25	
Container Diameter (mm), D_C	25.4, 28.58, 31.75, 34.93, 38.1, 44.45, 50.8, 57.15,63.5	
Number of Parallel Units, N	20-82	

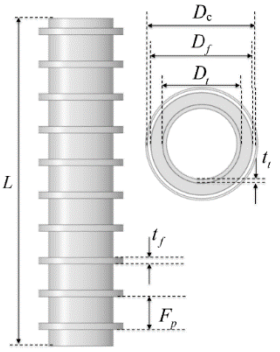

The optimization constraints include the total hot water supply time, the total HX volume, and the State of Charge (SOC). The minimum total hot water supply time is predetermined as 540 seconds [153].

Based on the volume of a commercially available storage-type domestic water heater tank with medium water usage [153], represented by a total volume of 254,650 cm³ ($V_{Tank, Baseline}$), the maximum total HX volume ($V_{HX,total}$) is determined, adhering to the U.S. DOE

target, which specifies that the thermal energy storage (TES) should not exceed 10% of the original system volume. The final constraint is based on the State of Charge defined as the ratio of energy stored in the TES at a specific time to the theoretical maximum energy storage, and ensures that the TES primarily remains in the latent region during PCM-HX operation (Equation (26)).

$$SOC(t) = \frac{Remaining\ energy\ stored\ (t)}{Theoretical\ maximum\ storeable\ energy} \quad (26)$$

The annular tube-fin PCM-HX optimization results are shown in Figure 25. The color scale indicates the PCM-HX discharge time, i.e., the total time the PCM-HX can supply hot water before the outlet temperature falls below the set-point temperature. The marker size corresponds to the total PCM-HX volume. Six optimal designs are further analyzed, each representing a cluster of designs with similar characteristics (e.g., geometry and performance).

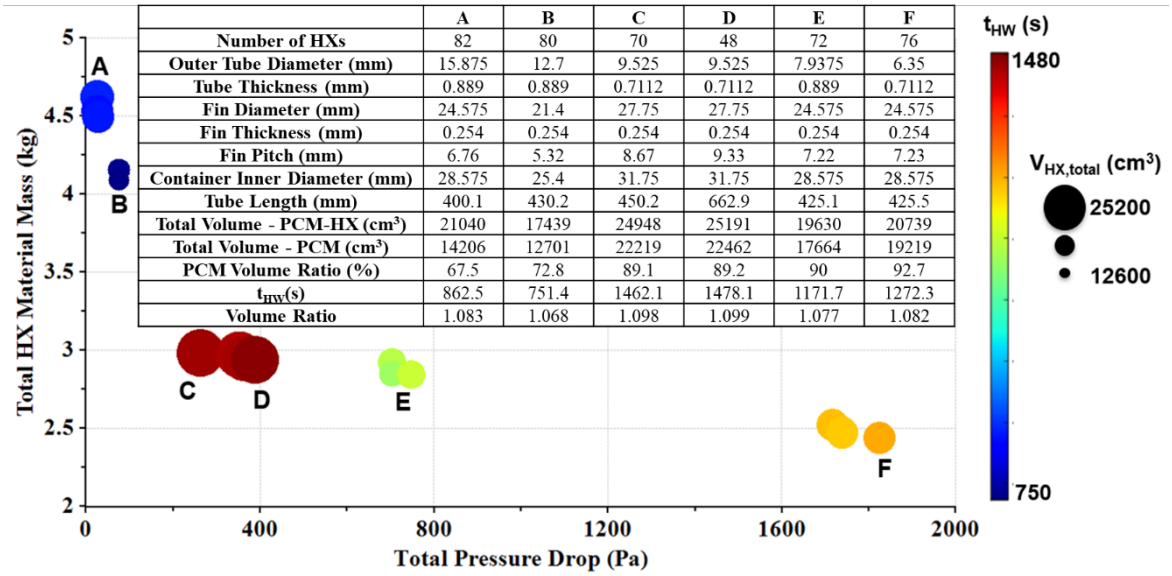

	A	B	C	D	E	F
Number of HXs	82	80	70	48	72	76
Outer Tube Diameter (mm)	15.875	12.7	9.525	9.525	7.9375	6.35
Tube Thickness (mm)	0.889	0.889	0.7112	0.7112	0.889	0.7112
Fin Diameter (mm)	24.575	21.4	27.75	27.75	24.575	24.575
Fin Thickness (mm)	0.254	0.254	0.254	0.254	0.254	0.254
Fin Pitch (mm)	6.76	5.32	8.67	9.33	7.22	7.23
Container Inner Diameter (mm)	28.575	25.4	31.75	31.75	28.575	28.575
Tube Length (mm)	400.1	430.2	450.2	662.9	425.1	425.5
Total Volume - PCM-HX (cm³)	21040	17439	24948	25191	19630	20739
Total Volume - PCM (cm³)	14206	12701	22219	22462	17664	19219
PCM Volume Ratio (%)	67.5	72.8	89.1	89.2	90	92.7
t_{HW}(s)	862.5	751.4	1462.1	1478.1	1171.7	1272.3
Volume Ratio	1.083	1.068	1.098	1.099	1.077	1.082

Figure 25: Annular finned PCM-HX optimization results with a tabulated summary of six selected designs.

Moving from left to right in Figure 25, the tube diameters and the number of parallel units generally decrease, leading to a greater water pressure drop. Larger tube diameters, lower fin pitches, and a higher number of parallel units contribute to the higher PCM-HX mass. Despite similarities in most aspects, designs C and D differ notably in tube length and the number of parallel units. Design D compensates for a lower number of parallel units with a tube length that is ~50% longer than the other designs.

Generalized Resistance-Capacitance Model (GRCM) (M3.1, M3.2, M3.3)

Introduction

Previous work with PCM-HX RCMs required creating a new resistance-capacitance network for every heat exchanger case of interest, which limits the ability to evaluate multiple PCM-HX geometries cost-effectively. To this end, we propose a computationally-efficient generalized RCM (GRCM) for predicting the thermal-hydraulic performance of PCM-HX.

GRCM Description

The GRCM is a computationally-efficient model capable of providing a good estimation of PCM transient behavior for any arbitrary Resistance-Capacitance network (Figure 26), unlike previous RCMs where a specific solver algorithm is required for every geometry. The geometry independence of GRCM provides flexibility to the solver, allowing rapid simulation by simultaneously solving the entire PCM-HX domain using a matrix inversion. The differences between the GRCM and RCM approaches are summarized in Table 24.

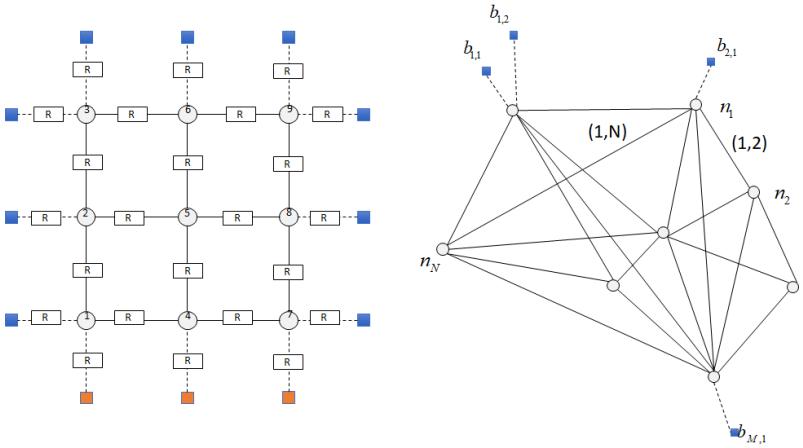

Figure 26: Arbitrary RC Networks: uniform (left), non-uniform (right).

Table 24: RCM vs. GRCM.

	RCM	GRCM
Solver	Geometry dependent	Geometry independent
Spatial marching	In series	Simultaneous (matrix inversion)
Computational cost	Low	Low
Flexible	No	Yes

Figure 27 shows the thermal networks for the RCM and GRCM. In the GRCM, the Resistance-Capacitance network is generated independently of heat exchanger geometry, while in the RCM is always uniform and geometry-dependent. The GRCM discretizes the PCM domain and calculates capacitances for each node. Resistances are placed based on horizontal and vertical connections as an array of pairs of nodes for each segment. The solver then calculates temperature difference using a simultaneous matrix inversion at each segment. Thereafter, the solver determines the temperature in the next time step and updates the flow time. The assumptions in the GRCM model include:

- Natural convection effects are disregarded, and conduction is the dominant heat transfer mode;
- No mass transfer across segments;
- The contact resistance between PCM and metal was neglected;
- Constant PCM thermophysical properties.

The domain is discretized into segments, where thermal resistances and capacitance of each segment are dependent upon the porosity. Segments with only metal structures have a porosity of 0, while segments with only PCM have a porosity value of 1. Segments containing both metal and PCM have volume-averaged porosity and thermophysical properties, as demonstrated by Alam et al. [157].

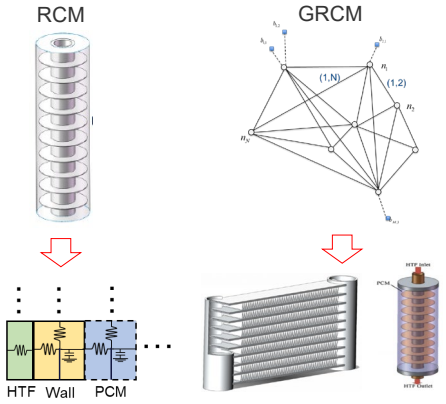

Figure 27: RCM and GRCM Resistance-Capacitance Network

Capacitances are calculated based on volume of each segment and PCM thermophysical properties, as in Equations (27) and (28).

$$C = [\gamma_{PCM} C_{PCM} \rho_{PCM} + (1-\gamma_{PCM}) C_{metal} \rho_{metal}] V_{node} \tag{27}$$

$$C_{PCM} = \begin{cases} c_{p,\,sol} & T \le T_{sol} \\ c_{p,\,sol} + \dfrac{h_s}{T_{melt} - T_{sol}} & T_{sol} < T < T_{melt} \\ c_{p,\,liq} & T \ge T_{melt} \end{cases} \tag{28}$$

The general matrix equations utilized by the GRCM are summarized in Equations (29)-(31). The matrix M is defined by vertical and horizontal internal resistances along segments, which are calculated based on thermal conductivity, segment area and length. The matrix B considers the heat transfer at the PCM-HX boundaries using the wall temperature (T_{wall}) and boundary resistances ($R_{boundary}$) for all boundary segments, as showed in. Then, the temperature change across the time step is calculated by taking the sum of all temperatures over the respective internal resistances summed by the heat transfer at the boundary, Equation (29). After calculating the temperature difference, the temperature for the next time step is updated based on Equation (31), where Δt is the time step.

$$B_i = \begin{pmatrix} \frac{T_{wall_i}}{R_{boundary_i}} \\ \vdots \\ \frac{T_{wall_i}}{R_{boundary_i}} \end{pmatrix} \quad (29)$$

$$\dot{T}_{i+1} = C_i^{-1}(MT_i + B_i) \quad (30)$$

$$T_{i+1} = T_i + \dot{T}_{i+1}\Delta t \quad (31)$$

The GRCM flowchart is demonstrated in Figure 28. The time marching is used to solve transient simulations for PCM storage devices. The solver initializes setting up capacitance, boundary and internal heat flow matrices. Then, GRCM calculates the temperature difference at each segment, solving a matrix inversion. Then, the solver updates the temperature at each segment for the next time step until the simulation time terminates.

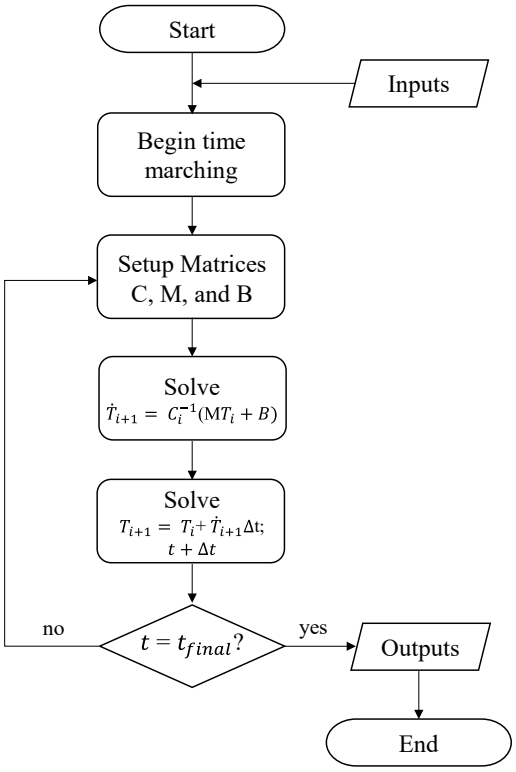

Figure 28: GRCM Flowchart

Summary of GRCM Verification & Validation

As part of this project, seven PCM-HX geometries using GRCMs were tested and validated (Table 25) for a wide variety of operating condition, and working fluids. The prototyping and experimental validation efforts for this PCM-HX will be discussed in future

chapters. The reader is referred to the noted references for additional information on each particular study.

Table 25: Summary of GRCM studies (with References)

Ref	PCM-HX Configuration	Source Data	Working Fluid(s)	Experimental Validation?
[143]	Rectangular PCM-HX with copper foam	Literature	-	Y
[143]	Optimized straight tube annular finned PCM-HX	CEEE	Water	Y
Internal Study (A)	Round tube plate-fin PCM-HX	Literature	Water	N
Internal Study (B)	Longitudinal fin PCM-HX	CEEE	Water	Y
[158]	PCM-to-refrigerant microchannel HX	CEEE	Refrigerant (R410A)	Y
	PCM-to-refrigerant embedded in graphite matrix	CEEE	Refrigerant (R134a)	Y
Internal Study (C)	Straight tube annular finned staged PCM-HX	CEEE	Water	N

GRCM Verification and Validation: PCM-HX with Metal Foam

To show GRCM capability in predict PCM with metal foams, Figure 29 shows the PCM-HX using paraffin PCM embedded in copper foam, as proposed by Zheng et al. [159]. This heat exchanger was heated by an electrical heater attached on top of the PCM-HX, providing a constant heat flux of 1150 W/m^2. Three thermocouples were placed at 25, 50 and 100 mm from the heated wall (Figure 29b). The PCM-HX dimensions are 100x100x30 mm. To verify and validate the 3D geometry HX, a transient 2D GRCM model was used with a grid size of 20x20 (400 elements), total simulation time of 2150 s and a time-step of 0.5 seconds.

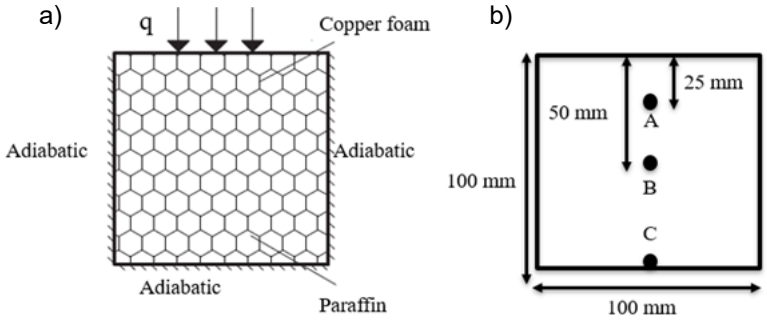

Figure 29: PCM-HX embedded in copper foam: (a) Domain and boundary conditions; (b) Thermocouple locations

The GRCM was verified and validated using CFD results proposed by Alam [160], and experimental data for a PCM-HX embedded in copper foam proposed by Zheng et al. [159]. The left side of Figure 30 shows an excellent agreement of the average PCM temperature with both CFD and GRCM simulations, resulting in maximum temperature deviation of 0.29 K.

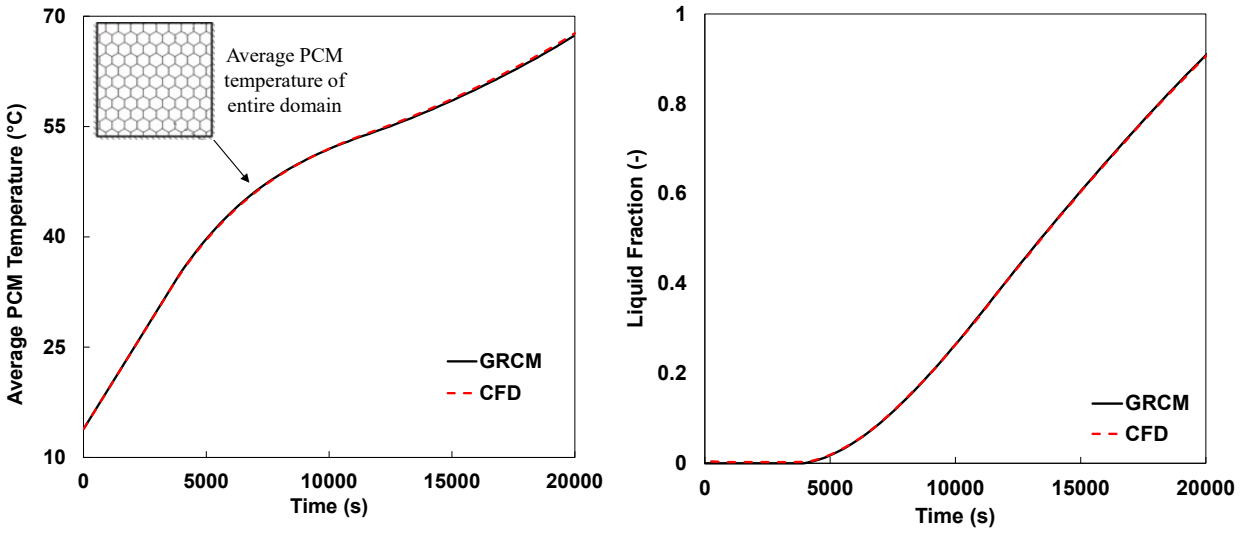

Figure 30: Average PCM temperature (Left) and liquid fraction (right) comparison between GRCM and CFD [160]

Figure 31 shows the PCM temperature profile at Thermocouple A (TC-A) and C (TC-C) and top wall for GRCM and CFD compared to the experimental data of Zheng et al. [159]. The deviation in temperature profile for TC-C is higher than for TC-A. It is worth to point out that TC-C is located at the bottom wall of the HX, opposite side of the heater, which was considered adiabatic during simulation. However, heat loss to the ambient during the experiment is unavoidable, which would result in higher GRCM-predicted temperatures compared to the experimental results. Comparing GRCM with experimental data, the mean temperature deviation for Thermocouples A and C are 1.57 K and 3.31 K, respectfully.

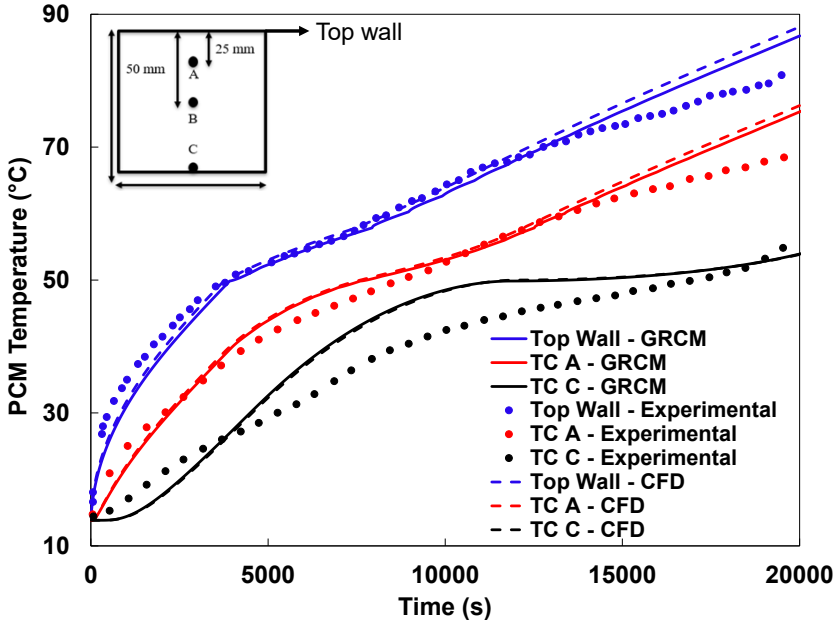

Figure 31: Verification and validation of GRCM based on the PCM temperature at different thermocouple locations based on experimental data [159]

GRCM Verification: Slab-Finned Microchannel HX

Figure 32 shows the single finned-slab microchannel PCM-HX [161]. The PCM is located in the top section of the HX between fins, and hot water flows through 68 ports in the minichannel tube. The PCM-HX operating conditions are as follows: the water inlet temperature is 63 °C with a mass flow rate of 30 g/s, and the initial PCM temperature is 20°C. Aluminum is the material for the tube and fins. The detailed geometry of the single-slabbed finned PCM-HX is listed in Table 26. This PCM-HX analysis is accomplished assuming conjugate heat transfer at the bottom boundary condition, while the external boundaries are assumed adiabatic.

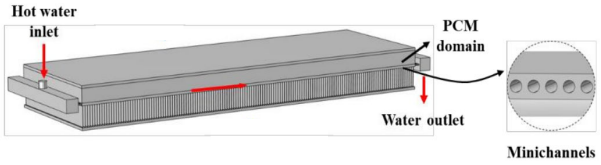

Figure 32: Single-slabbed finned PCM-HX domain and boundary conditions [161]

Table 26: Single-slabbed finned PCM-HX geometry specifications [161]

	Slab Width	Slab Length	Slab Height	Top Row Height	Number of fins	Fin Thickness	FPI	Channel Diameter	# of Tubes
Unit	mm	mm	mm	mm	-	mm	-	mm	-
Value	305	600	100	10.65	144	1.85	12	1	68

Three paraffin-based PCMs (Table 27) were considered: Docosane, Tetracosane, and Hexacosane, based on their availability, thermal properties, system compatibility, and practical application relevance [162].

Table 27. PCM thermophysical properties.

PCM properties	Docosane [163]	Tetracosane [164]	Hexacosane [165]
K_{solid} (W/m·C)	0.37	0.37	0.22
K_{liquid} (W/m·C)	0.24	0.20	0.15
Cp_{solid} (J/kg·C)	1700	1800	1694
Cp_{liquid} (J/kg·C)	2200	2100	2190
Latent heat (kJ/kg)	234	259	256
Density (kg/m³)	820	779	758
Melting range (°C)	42.9 – 44.1	48.1 – 50.6	55.3 – 56.3

Figure 33 shows the RC network and grid size used to simulate the single slab all-aluminum finned PCM-HX. To ensure computational efficiency, a grid size of 170x11 (1870-element RC network) was selected in this case. The simulation for the PCM-HX melting case spans a total time of 300 seconds, with a time-step of 0.001.

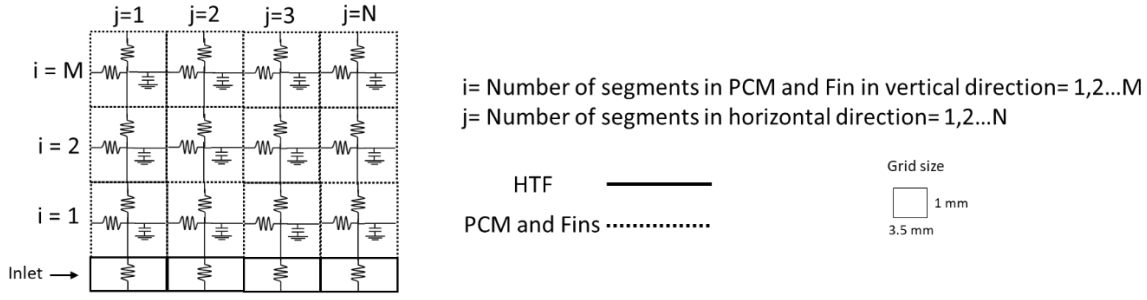

Figure 33: RC Network and grid size used in the GRCM simulation.

Figure 34 shows a comparison of the average PCM temperature predictions from CFD and the GRCM for the melting case for three PCMs: (i) Docosane, (ii) Tetracosane and (iii) Hexacosane. For the tetracosane and hexacosane cases, the highest temperature deviation comes from the estimation of temperature glide during PCMs charging case. It is possible to observe from Figure 34 that even with the assumption of neglecting the effects of natural convection in the model, the GRCM demonstrated excellent agreement in predicting average PCM temperature compared to CFD simulation.

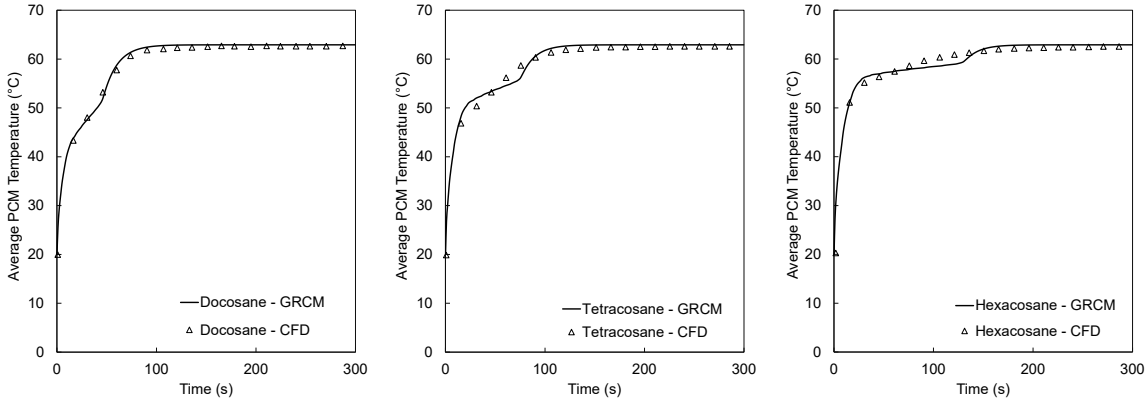

Figure 34: CFD vs. GRCM average PCM temperature: (Left) Docosane; (Center) Tetracosane; (Right) Hexacosane

Table 28 shows the accuracy prediction of GRCM compared to CFD. Compared to CFD simulation, the absolute mean deviation ranges from 0.6 – 0.7 K. This table also reports the maximum temperature deviation, which is 2.7 K for the tetracosane. The overall good agreement between GRCM and CFD showcases the ability of the GRCM to simulate different PCM-HX architectures with a high degree of accuracy and significantly less computational effort, e.g., the CFD grid used approximately 10^6 elements, while the GRCM used approximately 10^3 elements.

Table 28: Average PCM temperature deviation: CFD vs. GRCM

PCM	Absolute Mean Deviation (K)	Absolute Maximum Deviation (K)
Docosane	0.6	2.3
Tetracosane	0.7	2.7
Hexacosane	0.7	2.0

GRCM Validation: Optimized Annular Fin-Tube PCM-HX

For the annular-fin HX, the prototyped tested in-house at CEEE is shown in Figure 35. The dimensions selection is representative of an optimum design using the model proposed previously in this project. Then, an in-house experimental study was conducted for this specific design, and the data was used to validate the GRCM. To simplify simulation and reduce computational cost, an axisymmetric domain was employed, as it is extensively done in the literature [166], Figure 35b. Also, the RC-Network that represents the axisymmetric domain is demonstrated in this figure. For the annular-fin HX, a grid size of 260x8 (2080 elements) was chosen to compare with experimental data. The total simulation time is 360 and 250 s for melting and solidification cases,

respectively, with a time-step of 0.005. The geometry specifications for this PCM-HX are provided in Table 29. The assumptions for this validation are as follow:

- Adiabatic container wall
- Natural convection effects are negligible
- Conjugate heat transfer between PCM and HTF (Water)
- No mass transfer between segments

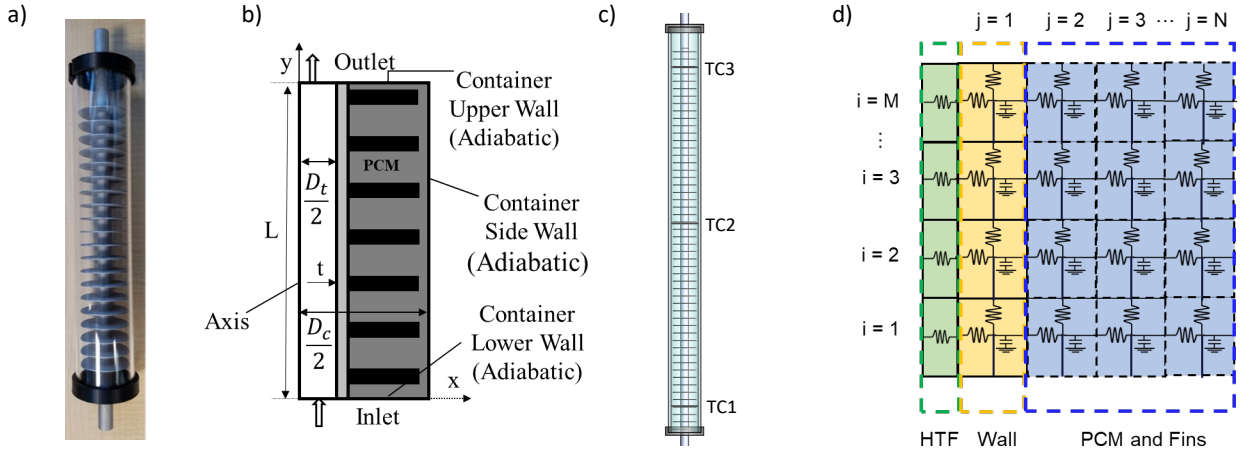

Figure 35: (a) Annular-Fin PCM HX design; (b) axisymmetric domain at the bottom; (c) Thermocouple positions and (d) RC-Network.

Table 29: Geometries specifications for Annular-Fin Heat Exchanger

	Tube Diameter	Tube Wall Thickness	Tube Length	Container Diameter	Container Wall Thickness	# of fins	Fin Pitch	Fin Thickness
Unit	mm	mm	mm	mm	mm	-	mm	mm
Value	9.53	1.78	475.2	38.1	6.35	52	8.67	0.25

The PCM used in this heat exchanger was RT62HC and the thermophysical properties is written in Table 30. The properties were taken from the manufacturer website. The model validation was done by placing virtual thermocouples in the same position as the experimental setup and comparing the PCM temperature profile during melting and solidification, as showed in Figure 35c. In addition, outlet water temperature was also simulated in this validation and compared against experimental data. The experimental PCM average temperature was calculated by taking the average temperature of the three thermocouple temperatures.

Table 30: RT62HC thermophysical properties [156]

PCM properties	RT62HC
K_{solid} (W/mK)	0.2
K_{liquid} (W/mK)	0.1
$C_{p,solid}$ (J/kg°C)	2000
$C_{p,liquid}$ (J/kg°C)	2000
Latent Heat (kJ/kg)	230
ρ_{solid} (kg/m^3)	850
ρ_{liquid} (kg/m^3)	840
Melting Temperature Range (°C)	62-63

As can be seen from Figure 36, the average PCM temperature is slightly overpredicted by the model for the melting case, while the solidification case showed good agreement. For the melting case, it is clear that the PCM temperature is overpredicted by the GRCM, which can be related to the assumption of neglecting heat loss to the ambient. Furthermore, during the PCM melting case, the third thermocouple (near the top) was exposed to air during experiment, due to PCM thermal expansion during the phase-change process. Therefore, the measured temperature at this thermocouple location should be ignored. Despite that, the overall agreement was acceptable, with mean temperature deviation between GRCM and experimental data of 1.71 K for the melting case.

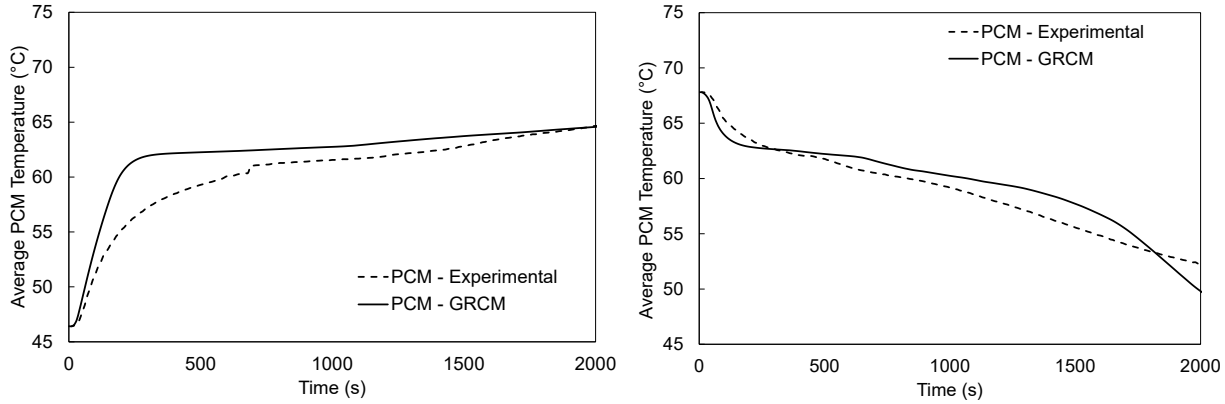

Figure 36: Average PCM temperature comparison of GRCM and experimental data for (left) melting and (right) solidification cases.

For the solidification case, the maximum temperature deviation was 2.45 K, with mean temperature deviation of 1.17 K. The temperature deviation during the solidification case can be explained by the overprediction of PCM phase-change process and the assumption of neglecting heat loss. The PCM temperature profile at each thermocouple is shown in Figure 37. As can be seen, the GRCM starts with a good agreement for Thermocouples 1 and 3, then deviates from experimental data, delaying the phase change of PCM. This discrepancy in measurement could be explained by the phase change hysteresis [167], which is not accounted for in the GRCM simulation.

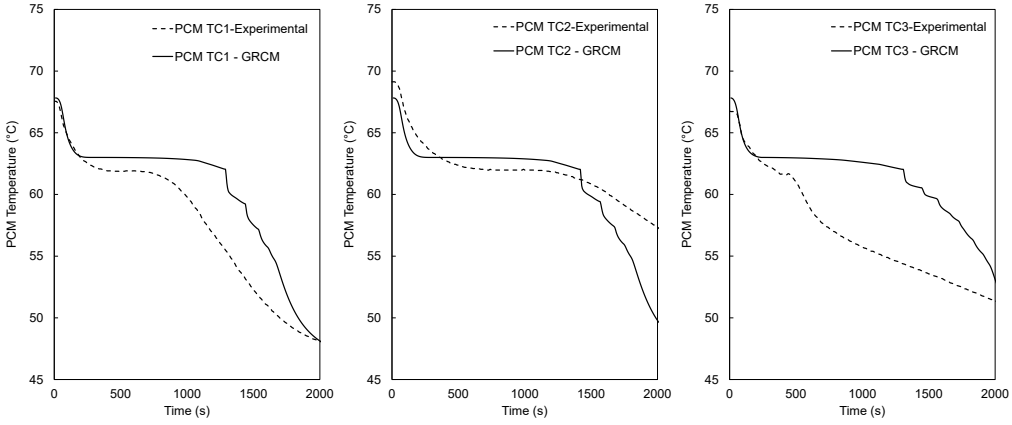

Figure 37: GRCM vs. experimental PCM temperature at each thermocouple position during PCM solidification

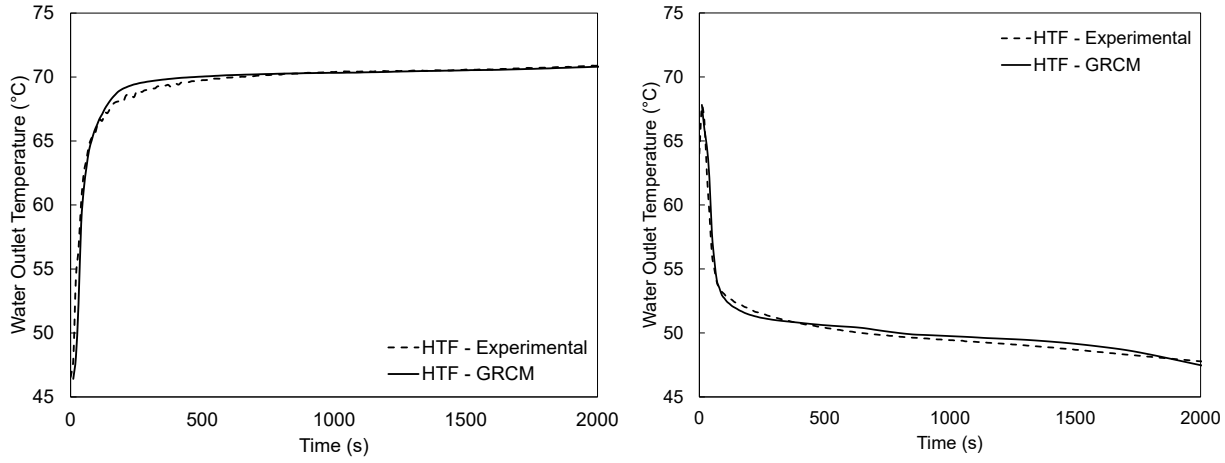

Figure 38: Water outlet temperature prediction from GRCM compared to experimental data: (left) melting case and (right) solidification case.

For the water outlet temperature, the GRCM showed good agreement for both melting and solidification cases, with the highest deviation occurring during PCM phase change, as can be seen in Figure 38. The deviation from experimental water outlet temperature increases over time due to neglected heat loss to the ambient. Compared to the experimental data, the mean temperature deviation during charging time was 0.24 K, while for the solidification case, the mean temperature deviation is 0.34 K, with maximum HTF outlet temperature deviation of 2.7 K.

GRCM Validation: PCM-to Refrigerant Straight-Tube HX

This validation uses the work proposed by Qiao et al. [168]. PCMRHX works as a condenser in a vapor compression cycle to store the waste heat from refrigerant condensation. In this work, Compressed Expanded Natural Graphite (CENG) is also added to increase PCM thermal conductivity. The PCMRHX was designed with a multi-tube configuration with the refrigerant flowing inside tubes, in which PCM was filled in the annular space between the PCM container and tubes. The refrigerant modeled in this HX was R134a. As explained by Dhumane et al. [169], only a single tube was modeled for simplification due to symmetry. The multi-tube, single tube designs and thermocouple location can be seen in Figure 39. The PCM used was PureTemp37, and thermophysical properties can be seen in Table 31.

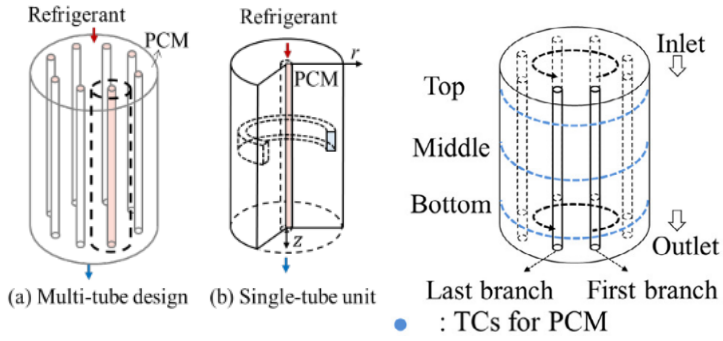

Figure 39: PCMRHX condenser design, model simplification and thermocouple (TC) location

The effects of both natural convection and radiation on the outer wall of the PCM container are accounted for by providing an outer wall heat transfer coefficient of 10 W/m^{2}K. The mid-point of the liquid to solid phase change temperature range was 35 °C with a temperature glide of 2 °C.

Table 31: PureTemp37 thermophysical properties

PCM properties	PureTemp37
K_{solid} (W/mK)	0.25
K_{liquid} (W/mK)	0.15
$C_{p,solid}$ (J/kg°C)	2210
$C_{p,liquid}$ (J/kg°C)	2630
Latent Heat (kJ/kg)	210
ρ_{solid} (kg/m^3)	920
ρ_{liquid} (kg/m^3)	840
Melting Temperature Range (°C)	34-36

For the refrigerant side, the HTC for single phase and two-phase refrigerant flow is calculated using correlation proposed by Gnielinski [170] and Shah [171], respectively. Figure 40 shows the condenser inlet temperature from the experiment, condenser outlet temperature from the experiment and also calculated by GRCM solver. Since the data collected from experiment comes from a VCC, the inlet refrigerant temperature has fluctuations due to variation in the mass flow rate and compressor power. Therefore, GRCM outlet refrigerant temperature also presents fluctuations since uses the temperature from experimental data to simulate the PCMRHX. There is a slight mismatch in the initial part of the cycle, which can be attributed to lack of a compressor model in the GRCM. However, the outlet comparison between condenser outlet temperature from experimental data and GRCM shows good agreement with mean temperature deviation of 1.11 K.

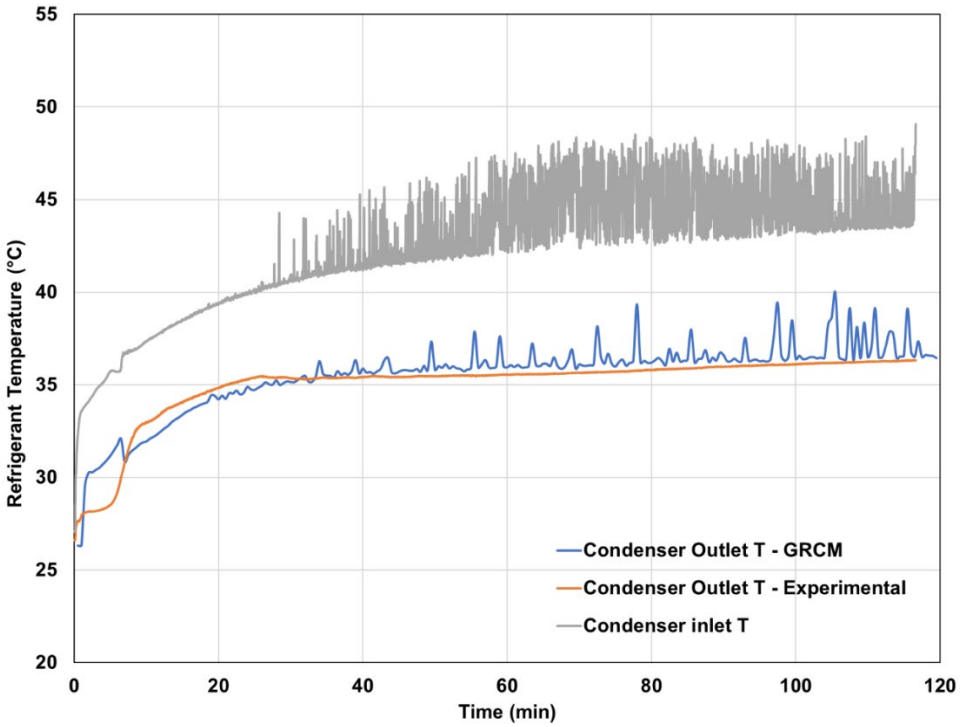

Figure 40: Outlet temperature comparison between GRCM and experimental data

GRCM Validation: PCM-to-Refrigerant Microchannel HX

Another simulation for two-phase flow was conducted for microchannel HX using a in-house CEEE experimental data to validate the model. The experiment details can be seen in the experimental and prototyping section. The refrigerant utilized was R410A and the PCM utilized was RT35 [148]. Three thermocouples (2,7,18) were utilized to validate the model, as shown in Figure 41. The refrigerant mass flow rate used for validation was 4 g/s. Figure 42 show the validation results for three different thermocouple positions. There is a rapid PCM discharging and the refrigerant outlet condition is two-phase, mainly because the condenser is oversized and PCM volume was not fully utilized before refrigerant outlet condition is two-phase. Even though the condenser is oversized, this faster PCM melting is also due to the use of refrigerant as HTF compared to water. The refrigerant has higher HTC compared to water which reduces the fluid resistance, increasing heat transfer to the PCM. Refrigerant mean temperature deviation of 1.1 K at Thermocouple 18.

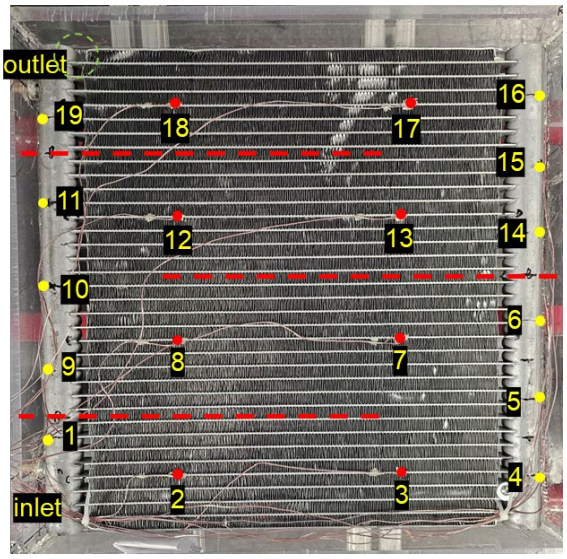

Figure 41: Microchannel HX Thermocouple positions

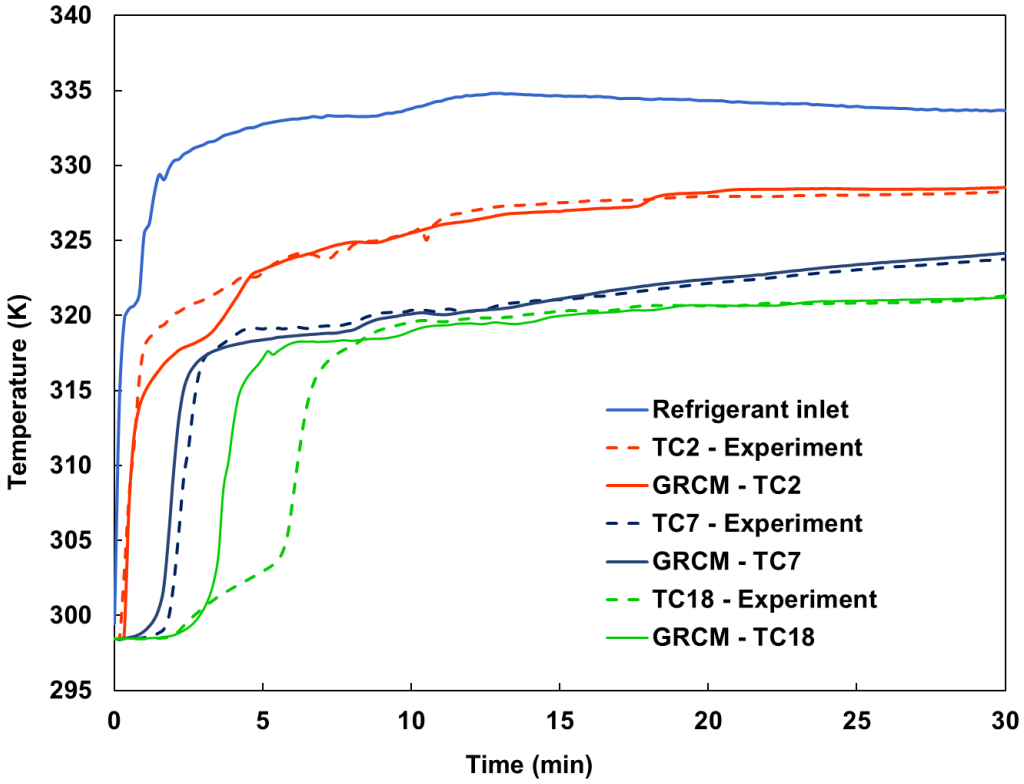

Figure 42: Validation results comparing experimental data and GRCM for the three thermocouple positions

GRCM Validation: Longitudinal Fin PCM-HXs

The longitudinal fin structure is based on the design proposed by [172]. Figure 43 shows the 3D prototype and PCM-HX schematic, showing thermocouple angular position and lateral view with plane section for thermocouple position. The HX consists of an aluminum tube with 10 longitudinal fins; 12 thermocouples are evenly distributed along the three planes in different angular positions. The GRCM considers conjugate heat transfer with water as the heat transfer fluid, while natural convection inside the PCM domain is disregarded. The PCM was RT35, with thermophysical properties presented in Table 32.

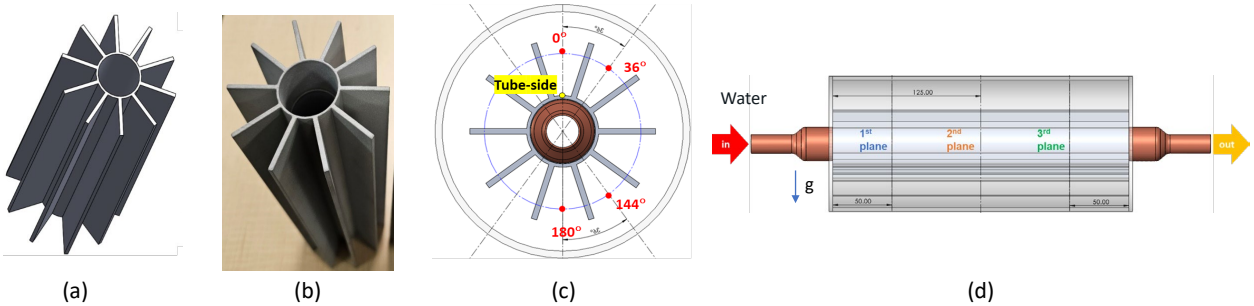

Figure 43: PCM-HX schematic: (a) and (b) 3D printed prototype; (c) thermocouple angular positions; (d) lateral view with plane section for thermocouples position

Table 32: PCM thermophysical properties [148]

Property	Unit	Nominal Value
k	W/mK	0.2
$c_{p,solid}$	kJ/kgK	2
$c_{p,liquid}$	kJ/kgK	2
Latent heat	kJ/kg	160
ρ_{solid}	kg/m³	770
ρ_{liquid}	kg/m³	860
Melting range	°C	32-38

Longitudinal Fin PCM-HX – Solidification Case

Figure 44 shows the results for solidification comparing virtual thermocouples in GRCM with the four thermocouples placed at the 2nd plane on the HX during experimental data. The temperature difference of each thermocouple in different plane sections are very small, thus, 2nd plane was used for validation. As can be seen from Figure 44, GRCM predicts really well the PCM temperature, especially in thermocouples with angular position of 144° and 180°. The good agreement between GRCM and experimental data is because conduction plays a more important role and is the dominant heat transfer process during solidification.

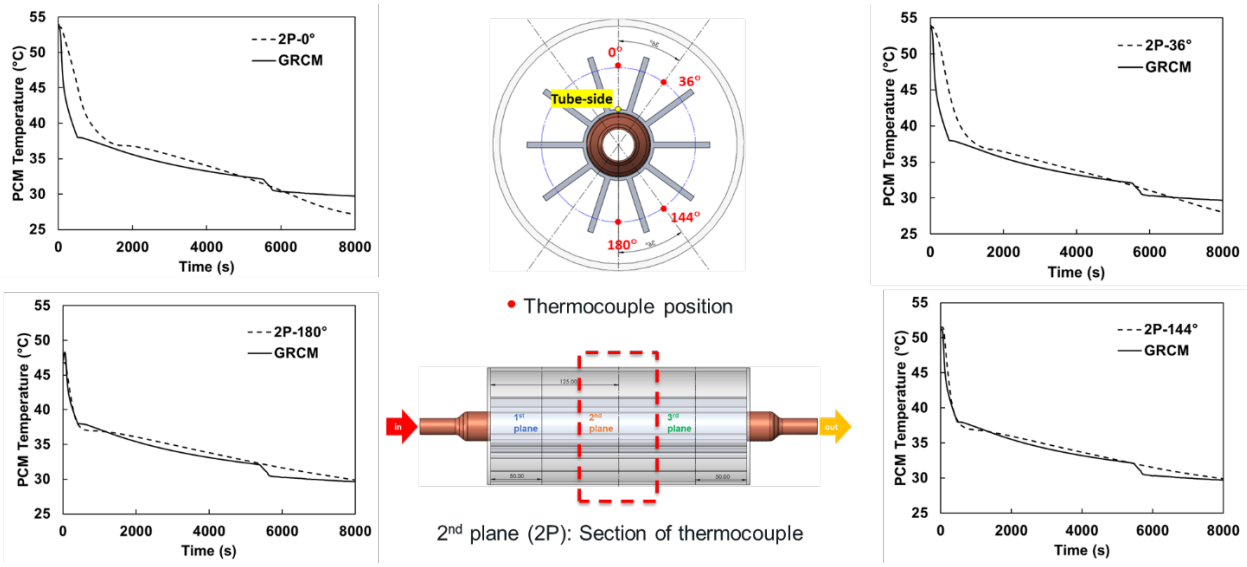

Figure 44: GRCM vs. experimental PCM temperature at each thermocouple position during PCM solidification

Longitudinal Fin PCM-HX – Melting Case

Same thermocouples angular position and at the same plane is analyzed and compared to experimental data, as can be seen in Figure 45. Convection is substantially dominant than conduction in the PCM phase transition process. GRCM solution approach is conduction dominate, disregards effects of natural convection, thus, we have higher deviation during melting case compared to solidification case. This deviation is more prominent for thermocouples placed at the top, since buoyancy effects are dominant in these positions.

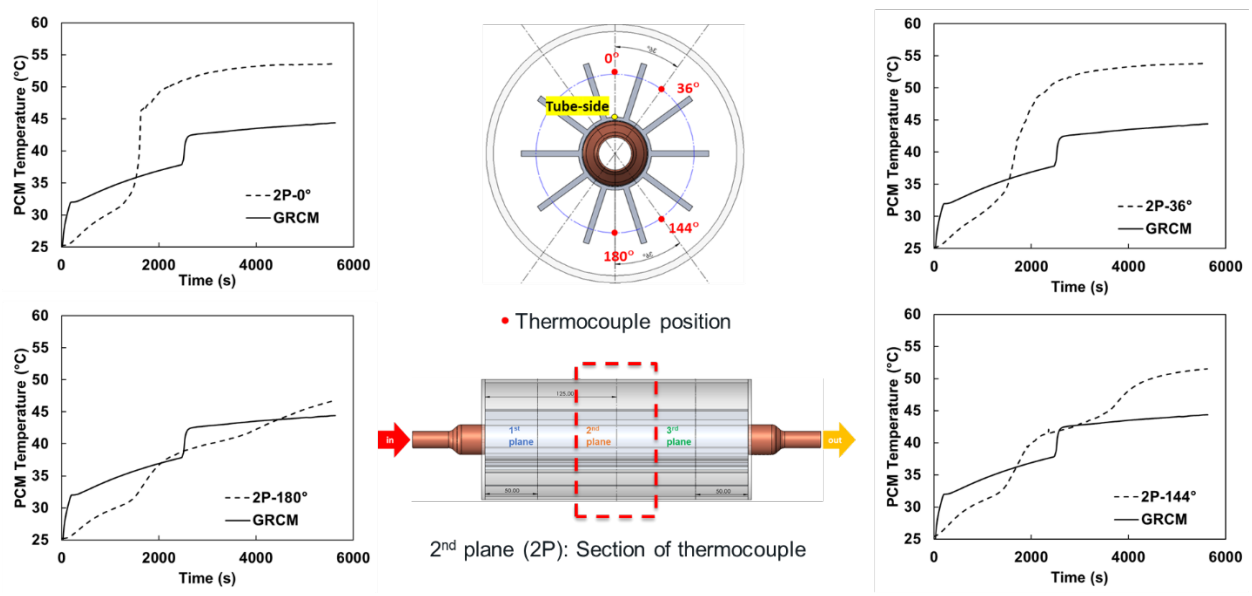

Figure 45: GRCM vs. experimental PCM temperature at each thermocouple position during PCM melting

Longitudinal Fin PCM-HX – Water Outlet Temperature and Instantaneous Heat Transfer

For model validation, the water outlet temperature predicted by the GRCM was compared with experimental measurements for both melting and solidification processes, as shown in Figure 46. The green line represents the inlet water temperature, the solid black line indicates the GRCM-predicted outlet temperature, and the dashed line corresponds to the experimental data. The model shows excellent agreement, with mean temperature deviations of 0.17 K for melting and 0.22 K for solidification. However, this strong agreement is partially attributed to the low temperature difference between inlet and outlet water at the tested mass flow rate of 30 g/s. To gain deeper insight into the PCM charging and discharging behavior, instantaneous heat transfer rates were also analyzed. Specifically, heat transfer from the water from experimental data was compared with the heat absorbed or released by the PCM from GRCM.

As illustrated in Figure 46, greater deviation in instantaneous heat transfer is observed during melting compared to solidification. This is primarily due to the GRCM's neglect of natural convection effects, which play a more significant role during the melting process. The larger deviation during melting also reflects the higher temperature gradients within the PCM during this phase, compared to the more uniform temperature profile observed during solidification.

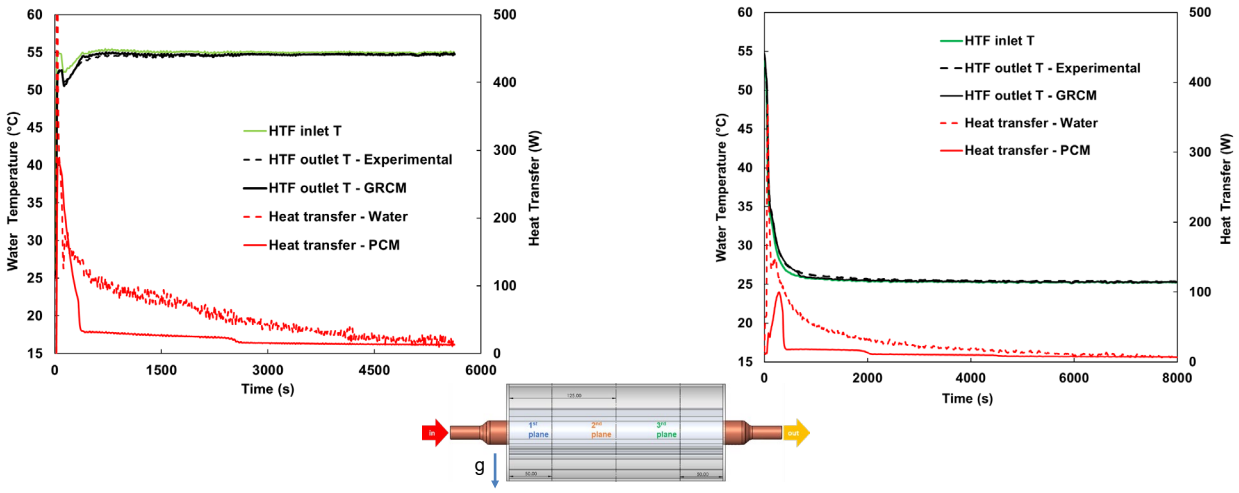

Figure 46: Outlet water temperature and instantaneous heat transfer comparison from water (experiment) and PCM (GRCM) for melting case (left) and solidification case (right)

As can be seen from Figure 47, using water mass flow rate of 30 g/s gives temperature difference below 1K. Higher mass flow rate was used in this case to mimic constant heat flux along the tube. To validate the model, a second, lower water mass flow rate (10 g/s) was considered, allowing for higher temperature change (~5 K) in the heat transfer fluid (water), as shown in Figure 47. Since melting case is convection dominant, higher water temperature deviations are found compared to solidification case, which is conduction dominant. The average water outlet temperature difference of between GRCM and experiment for melting and solidification cases are 1.73K and 0.6K, respectively.

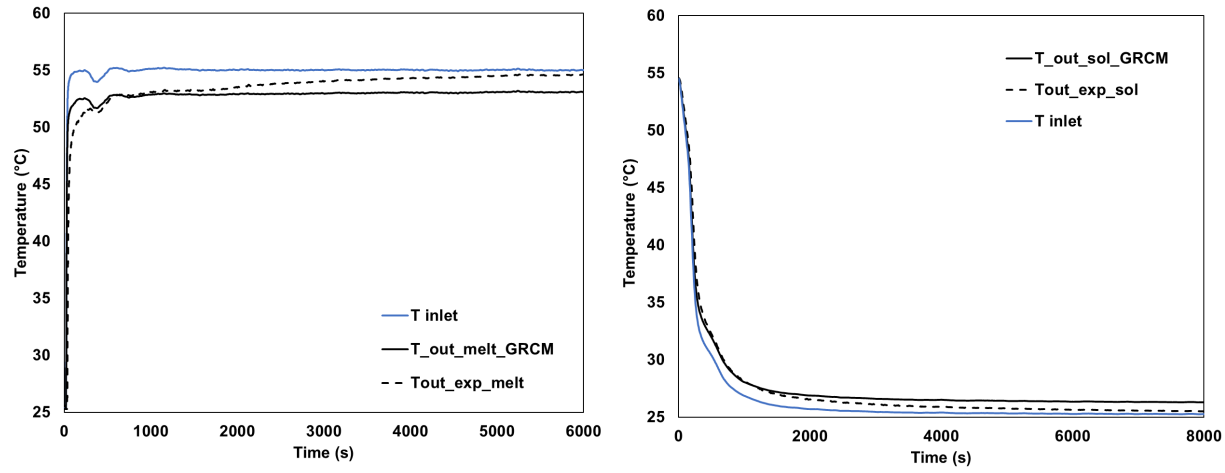

Figure 47: GRCM vs. experimental water outlet temperature; (Left) PCM melting; (Right) PCM solidification

Performance Maps for Fast & Accurate Building Energy Simulations (M3.2)

Introduction

Thermal energy storage (TES) using phase change materials (PCMs) has attracted increased attention as a viable solution for managing the fluctuating nature of energy

demand and shifting peak building loads. PCM-embedded heat exchangers (PCM-HXs) offer high energy storage density and low temperature variation during phase change, making them effective for thermal management. However, assessing PCM-HX component-level performance is typically done using fully transient, and computationally expensive, Computational Fluid Dynamics (CFD) simulations, which presents significant challenges when the ultimate goal is to assess the performance of PCM-HX integrated thermal energy storage systems in the full building context. In this section, we present a methodology to generate highly accurate and computationally efficient PCM-HX performance maps which can be easily integrated into building energy simulation tools to analyze the feasibility of space conditioning systems with latent heat PCM-based TES. The performance maps are generated using a computationally efficient PCM-HX simulation tool based on a Generalized Resistance-Capacitance Model (GRCM) which can simulate arbitrary PCM-HXs with high accuracy and significantly less computational effort compared to full CFD simulations. The methodology was verified for a case study considering an integrated dual-mode heat pump-thermal energy storage system (HP-TES) which was co-simulated in Modelica for a DOE prototype small-office building using the Spawn of EnergyPlus™. The GRCM-based performance maps provided accurate predictions of PCM-HX behavior, with a maximum deviation of 4.1% in PCM-HX discharge rate when compared to full GRCM simulations. This work highlights the importance of robust PCM-HX models for efficient and high-fidelity building-level simulations while also presenting future research opportunities for investigating optimized HP-TES designs in a computationally-efficient manner.

PCM-HX Design

The PCM-HX is the most critical component in the integration and must be sized to meet the required storage capacity (i.e., the operating time) and charge/discharge rate in both cooling and heating modes (i.e., the building load). Here, the PCM-HX was sized to meet the required space conditioning loads for a DOE prototype small-office building [174] for three hours in three US climate zones: Tampa (2A), New York City (4A) and International Falls (7). Table 33 shows the heating and cooling load for the office building, with values based on the design day in the target locations in the paper. These calculations were based on ASHRAE Standard 90.1-2022 [174]. Therefore, the PCM-HX capacity was changed by scaling up or down the number of unit cells in the heat exchanger, while maintaining the same geometric design to achieve the design load.

Table 33. Calculated heating and cooling design load for target cities in different ASHRAE climate zones

City	Calculated Design Load – Heating (kW)	Calculated Design Load – Cooling (kW)
Tampa, FL (2A)	5.9	16.3
New York City, NY (4A)	12.3	14.7
International Falls, MN (7)	16.5	14.3

The PCM volume required to achieve this demand is demonstrated in Equation (32):

$$V_{PCM} = \frac{\int_{t_i}^{t_f} \dot{Q} dt}{\rho_{PCM} H_{Latent}} \quad (32)$$

In which $\dot{Q}$ represents the building load demand, ρ_{PCM} and H_{Latent} are the PCM density and latent heat, respectively. The PCM-HX design is based on staggered finned-tubes HX units (Figure 48), which are widely applied for air conditioning applications and have shown good performance for PCM-HX applications [175]. The PCM-HX container is assumed to be well-insulated, and thus the container walls are considered adiabatic.

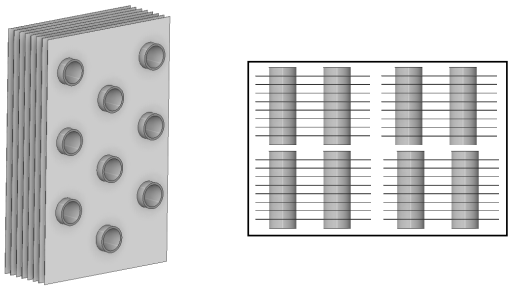

Figure 48. Round-tube plate-fin heat exchanger configuration and sample schematic of thermal battery array

Based on the building load requirements, the PCM-HX size for heating and cooling demand is showed in Table 34.

Table 34. Thermal battery geometry metrics for heating and cooling modes

Measure	Unit	Heating PCM-HX	Cooling PCM-HX
Horizontal Spacing (HS)	m	0.03125	0.03025
Vertical Spacing (VS)	m	0.02875	0.0265
Tube Length	m	0.95	0.9
Outer Tube Diameter (OD)	m	0.00925	0.00925
Inner Tube Diameter (ID)	m	0.0089	0.0089
Tube thickness	m	0.00033	0.00033
FPI	-	13	14
Fin thickness	m	0.0001	0.0001
Porosity	%	87.4	86.2
Distance between tubes (L)	m	0.0145	0.0134

The dimension L represents the equivalent distance between HX tubes, as shown in Equation (33):

$$L = \frac{\sqrt{(VS - OD)^2 + (HS - OD)^2}}{2} \quad (33)$$

The thermophysical properties of all PCMs used in this work are given in Table 35. Organic PCM A36 was the PCM used for heating mode, while A12 was used for cooling mode. For each PCM, a temperature glide of 4 K is assumed for numerical purposes. The PCM is fully charged (Melt Fraction = 1) PCM is at T = $T_{nominal}$ + 2 and fully discharged

(Melt Fraction = 0) for PCM at T = $T_{nominal}$ – 2. Therefore, the PCM energy stored includes a small portion of usable sensible heat capacity.

Table 35. PCM thermophysical properties [176]

Property	Unit	A36	A12
k_{solid}	W/mK	0.22	0.22
k_{liquid}	W/mK	0.22	0.22
$c_{p,solid}$	kJ/kgK	2.3	2.16
$c_{p,liquid}$	kJ/kgK	2.3	2.16
Latent Heat	kJ/kg	250	215
Density	kg/m³	790	775
Melting Temperature Range	°C	34-38	10-14

Generating TES Performance Maps using GRCM

Modeling both the charging and discharging performance of PCM storage unit is accomplished in EnergyPlus™ [177] using curve objects that establish the relationships between different parameters in the unit. The present work builds upon the thermal storage model available in EnergyPlus™, developed by Henze and Krarti [178], which is based on a simple ice storage tank with fixed capacity. For this model to be utilized for building simulations, it is essential to create PCM and HX-specific performance maps for each application [179]. To this end, GRCM simulations are utilized to develop TES performance maps, i.e., UA curve fits, for the discharge and recharge processes as a function only of liquid fraction (x_{melt}), as shown in Equation (34).

$$UA_{curve\_fit} = C_1 + C_2 x_{melt} + C_3 x_{melt}^2 + C_4 x_{melt}^3 + C_5 x_{melt}^4 + C_6 x_{melt}^5 \quad (34)$$

The coefficients for the UA_{curve_fit} are calculated using regression, where the GRCM liquid fraction output at each time step is used as input. The UA from GRCM is computed using the UA-LMTD procedure (Equations. (35)-(37)), at each time step. The different boundary conditions for the PCM solidification and melting case require two performance maps per PCM-HX geometry, one for solidification and one for melting.

$$\dot{Q} = \dot{m} c_{p,water} (T_{water\_out} - T_{water\_in}) \quad (35)$$

$$LMTD = \frac{T_{water,in} - T_{water,out}}{\ln\left(\frac{T_{water,in} - T_{PCM}}{T_{water,out} - T_{PCM}}\right)} \quad (36)$$

$$UA_{GRCM} = \frac{\dot{Q}}{LMTD} \quad (37)$$

In which $\dot{Q}$ is the heat transfer rate from the water, T_{PCM} is the nominal PCM temperature, and $\dot{m}$ is the water mass flow rate.

Integration of Performance Maps into Modelica & Spawn of EnergyPlus™

Figure 49 shows the schematic of the air-to-water HX in the Modelica Buildings Library, incorporating the PCM-HX simulation, Spawn of EnergyPlus™, and the DOE small office prototype [177], [180], [181]. The PCM-HX, shown in the upper-left section, circulates water/glycol at a controlled mass flow rate. The building block represents thermal zones,

interacting with the air-to-water heat exchanger to regulate the small office temperature conditions. The air-to-water HX comprises 95% recirculated air and 5% fresh intake, with sensors monitoring air supply temperature and flow rates. The PCM-HX operates continuously to meet dynamic building loads. Spawn of EnergyPlus™ integrates IDF files and weather data for the selected climate zone.

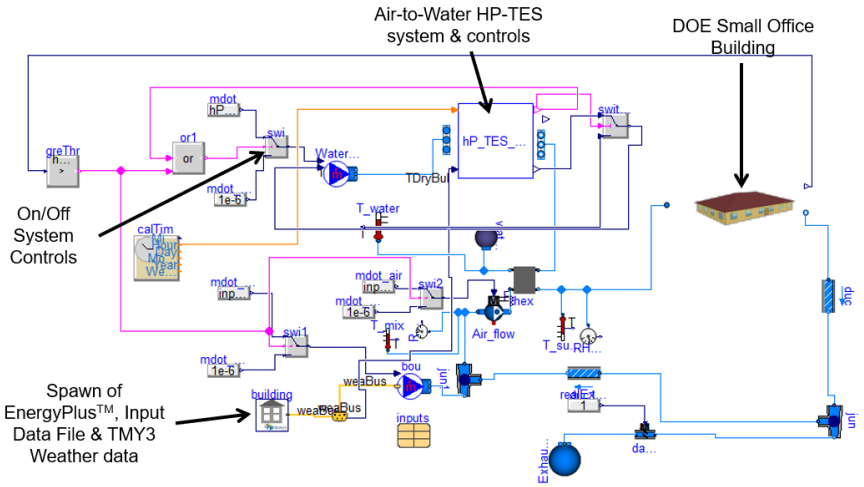

Figure 49. Modelica Buildings Library interface with DOE small office prototype and Spawn of EnergyPlus™

The rule-based control logic dynamically adjusts system operation based on thermal load, enabling efficient PCM utilization for peak load shifting. This simulation framework provides the evaluation of transient thermal storage integration in HVAC systems to enhance building energy efficiency. The HP-TES controller receives two external inputs: daily hours and thermostat setpoints. Daily hours determine the switch between baseline and TES operation based on time-of-use (TOU) schedules. Thermostat setpoints control temperature, and HVAC activation in response to building loads. During TOU hours, the system is either on or off, while off-peak periods introduce TES recharge. TES discharge and recharge are managed using the internal melt fraction (x_{melt}) as input.

The two PCM-HX modules use melt fraction as initial conditions for TES discharging and recharging, based on PCM-HX requirements. TES discharges during TOU hours when the melt fraction is between 5% and 95%. When the melt fraction falls below 5%, the discharge operation is ceased, and a signal triggers the recharge module, which uses the final discharge melt fraction as its initial condition for the recharge operation. Recharge occurs during off-peak hours, manually selecting the coolest nighttime hours for cooling mode (latest nocturnal hours) and the warmest for heating (earliest nocturnal hours), in the rule-based controls, minimizing energy consumption [182]. Once recharge is complete (x_{melt}≥ 95%), the system resets and signals the discharge module to prepare for the next cycle.

Performance Map Verification

After GRCM simulation, six coefficients for the UA equation for both cooling and heating were generated, as shown in Table 36. The resulting UA coefficients are implemented

within the Modelica Buildings Library using Spawn of EnergyPlus™ to represent the PCM-HX [177], [180].

Table 36. UA coefficients for cooling and heating mode

Coefficients	Cooling Mode		Heating Mode	
	Discharge	Recharge	Discharge	Recharge
C1	13270.3	338.4	389.6	7547.5
C2	-67047.3	15188.2	15242.0	-14050.9
C3	238992.9	-34190.9	-29508.2	33122.4
C4	-447786.3	61151.6	45570.5	-55181.3
C5	401688.5	-60562.2	-41845.9	46651.3
C6	-138878.5	26813.1	17699.4	-17699.4

Figure 50 shows the UA comparison of GRCM and curve-fit equation model over time for cooling mode discharge operation. It is clear that curve-fit UA equation matches very well with the GRCM predicted UA, having mean absolute percentage error of 4.1% between these two curves. The maximum error, 38.5%, occurs at the beginning of the solidification process due to the GRCM-predicted water outlet temperature being very close to the nominal PCM temperature. Nevertheless, the estimation of the curve-fit equation is very good and considered acceptable for full system simulation.

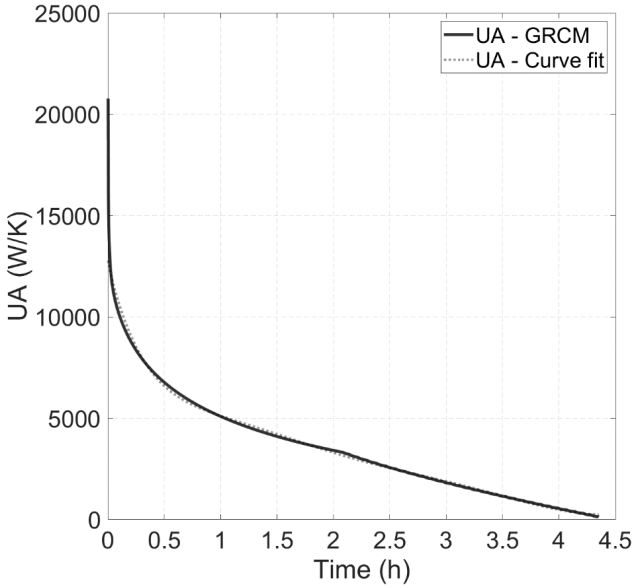

Figure 50. UA comparison from GRCM and performance map equation for PCM melting during cooling mode

Using the UA. Equation (34), from GRCM performance map, PCM-HX performance Maps can be simulated in Modelica Buildings Library. To verify the UA curve-fit, Figure 51 shows the comparison of GRCM prediction and Modelica with curve fitted UA for heat transfer rate (Figure 51a) and liquid fraction (Figure 51b). These results show good agreement between Modelica and GRCM, with a mean absolute percentage error of 2.8% for the heat transfer rate, with a maximum deviation of 13.6%. The largest deviation occurs near the start and end of the solidification phase change process, likely because

the UA curve-fits, as a reduced-order model, do not capture all phase change transients compared to the GRCM. Nevertheless, the agreement is still very good overall.

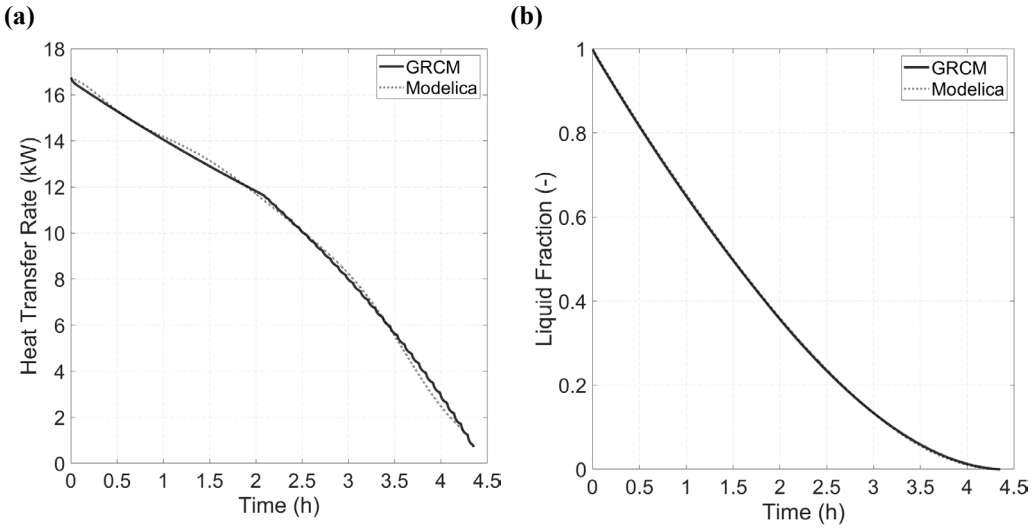

Figure 51. Comparison between GRCM and Modelica: (a) heat transfer and (b) liquid fraction

Seasonal Simulations

A set of numerical simulations was conducted using the validated GRCM model to evaluate the TES performance maps generated for HP-TES systems operating in both cooling and heating modes across various climates. Three ASHRAE climate zones were selected to capture the influence of outdoor air temperature variability: Tampa, Florida (2A); New York City, New York (4A), and International Falls, Minnesota (7). Simulations were carried out for January 8th (heating) and July 15th (cooling), as these dates correspond to periods of TES activation in all locations. The discharge and recharge control strategies for the HP-TES follow the time-of-use hours (TOU) according to electricity companies for each city: 8 AM to 8 PM for New York [183]; 3 PM to 9 PM for Minnesota [184], and 12 PM to 9 PM in Florida [185]. During TOU hours, the system dynamically shifts from the baseline operation to TES discharge, and reverts to baseline or recharges during off-peak periods, thereby mitigating peak electricity demand.

Integrating TES into the conventional HP system enables targeted demand reduction during critical on-peak periods. To quantify this benefit, the on-peak demand reduction is calculated using Eq. (38), in order to evaluate trends in TES regarding outdoor temperature and climate zone. Reported demand reductions represent the maximum compressor power savings achieved during TOU periods, excluding auxiliary loads such as pump and fan power.

$$Demand\ \mathrm{Re}duction = \frac{W_{on-peak,baseline} - W_{on-peak,HP-TES}}{W_{on-peak,baseline}} \times 100 \quad (38)$$

Cooling Mode

An important aspect in evaluating the HP-TES performance maps is the system behavior under discharge and recharge control strategies. In this study, co-simulation was conducted in Modelica using a 10-second time step, with the HP-TES system simulated over 24 hours (midnight to midnight) to capture the system response and TES utilization dynamically. Figure 52 shows New York City simulation, demonstrating the 5-ton unit baseline HP operation and the HP-TES operation, both showing indoor setpoint temperature and outdoor dry bulb temperature. The results indicate that the TES effectively maintains indoor temperatures within the desired range, cycling the system on and off in intervals of approximately 6 minutes, and maintaining indoor temperatures between 23 °C and 25 °C for approximately three hours. Moreover, the TES discharges exclusively during time-of-use (TOU) periods, in accordance with the rule-based control strategy, reducing reliance on the baseline HP during peak demand hours. Specifically, under the simulated conditions for New York City, the TES system achieves a peak demand reduction of up to 39.8%.

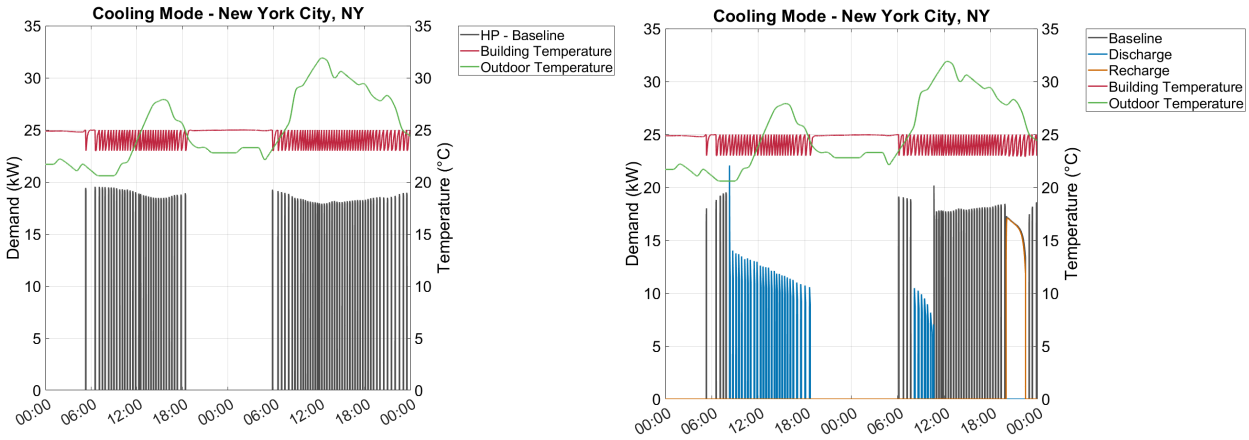

Figure 52. Baseline HP capacity (left); HP-TES cooling capacity, indoor setpoint temperature and dry bulb temperature (right) for cooling mode in New York City, NY

Regarding International Falls, the climate zone presents a mild summer climate, in which outdoor temperatures remain below the indoor setpoint for most of the day. This condition reduces the need for cooling demand by the heat pump, as illustrated in Figure 53. However, during periods when the outdoor temperature reaches its daily peak, the TES effectively maintains the desired indoor temperature. During these peak conditions, the TES discharges for approximately one hour, cycling on and off in 5-minute intervals. Compared to the baseline heat pump operation, the TES system achieves a peak demand reduction of approximately 31%.

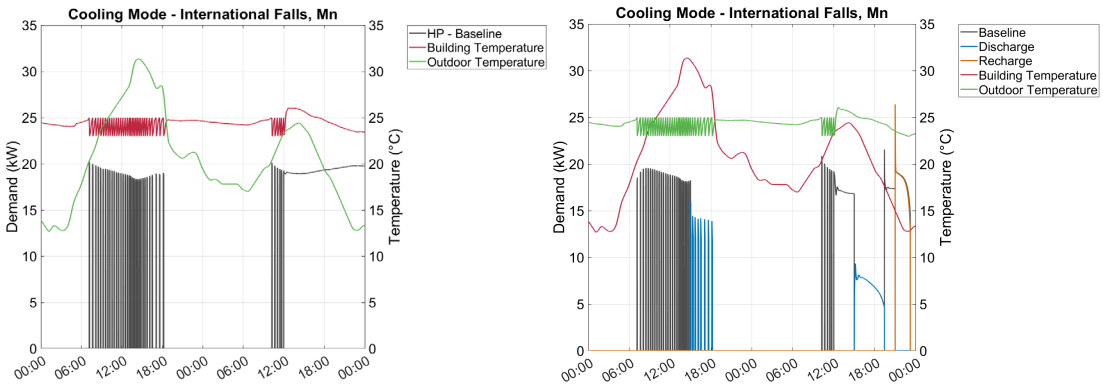

Figure 53. Baseline HP and TES capacity (left); HP-TES cooling capacity, indoor setpoint temperature and dry bulb temperature (right) for cooling mode in International Falls, Mn

It is important to note that a two-day simulation period was used for New York City and International Falls to capture the recharge dynamics of the HP-TES system. Due to temperature reductions and TOU hours control, the system was unable to fully discharge the TES within a single 24-hour cycle. Therefore, an extended simulation was necessary to effectively demonstrate the HP-TES ability to undergo both discharge and recharge operation.

Figure 54 compares the performance of the baseline HP system and an HP-TES system in Tampa, FI. The figure on the left illustrates the operation of the baseline HP, which runs continuously throughout the day to maintain indoor temperature. This results in a significant peak electricity demand during the hottest hours of the day. The results indicates that climate zone 2A imposes a higher cooling demand compared to the other analyzed regions, leading to full discharge of the PCM-HX within the operational window. The right figure depicts the HP-TES system performance. In this scenario, the TES discharges during the afternoon TOU period and recharges during off-peak hours, as indicated by the orange curve. The TES provided approximately 3.8 hours of operation during peak demand, resulting in a notable reduction of on-peak demand by 41%, as compared to the baseline system. Despite the shift in operation strategy, indoor temperature remained well-regulated in both cases, demonstrating the effective thermal management and utilization of the PCM-HX.

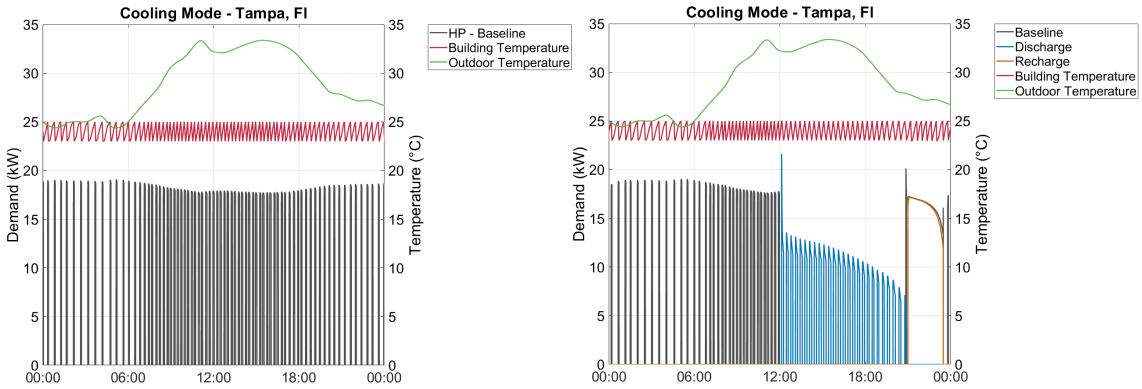

Figure 54. Baseline HP and TES capacity (left); HP-TES cooling capacity, indoor setpoint temperature and dry bulb temperature (right) for cooling mode in Tampa, Fl

As can be seen from all simulations, the baseline HP exhibits higher demand than the TES-integrated system, despite the TES effectively meet the building load. This is primarily due to the baseline HP being sized as ASHRAE Standard 90.1 design day conditions, whereas GRCM co-simulations with Modelica does not represents the design day demand requirement. Nonetheless, the GRCM performance maps accurately captured the PCM-HX behavior across all applications, demonstrating their suitability for rapid evaluation of building integration and HP-TES correctly sized for on-peak demand reduction.

Heating Mode

For heating mode, the same simulation window was utilized to demonstrate TES operation in a day of winter. Figure 55 shows New York City simulation, demonstrating the 5-ton unit baseline HP operation and the HP-TES operation, both showing indoor setpoint temperature and outdoor dry bulb temperature. It is possible to notice that the TES is able to maintain the building temperature between 19 °C – 21 °C throughout the entire day. Since the HP system is design for both cooling or heating, the HTF mass flow rate is oversized for heating mode, leading to a higher TES system capacity compared to cooling mode. To this end, the TES maintains the building load for longer time, discharging at every 15 min for approximately 4.3 hours in New York and International Falls. However, as cooling mode, fully exhausting TES indicates that the TES capacity and HX were properly sized and designed. And this proper simulation highlights the importance of robust PCM-HX models for efficient and high-fidelity building-level simulations.

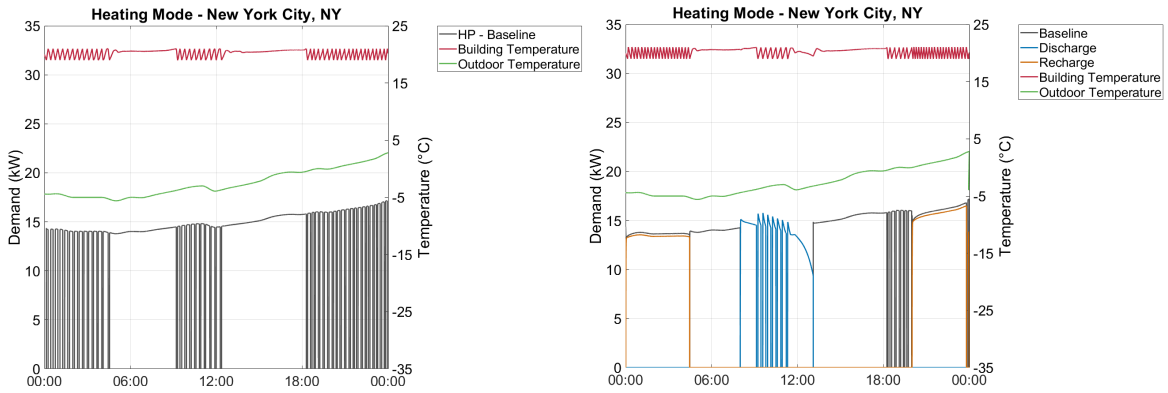

Figure 55. Baseline HP and TES capacity (left); HP-TES cooling capacity, indoor setpoint temperature and dry bulb temperature (right) for heating mode in New York City, NY

International Falls showcase a better utilization of HP-TES systems, demonstrated in Figure 56. Since the climatic conditions in International Falls are extremely cold, in this day the baseline HP operation is not able to meet the required system capacity, since the ambient temperatures are outside of the heat pump operating envelope. Therefore, the system demands backup heating to assist in achieving the building load or only the backup heat will be turned on. From Figure 56(b), the HP-TES system eliminates the need for backup heating during peak hours, providing substantial on peak demand reduction in very cold climate condition. This happens due to the reduced temperature lift in the HP-TES operation, which increases heating capacity compared to the baseline application.

In Tampa, due to the mild summer, the TES basically runs at night, when the temperature drops below 5 °C, as can be seen in Figure 57. Due to mild weather conditions, the TES is only utilized for less than 2h. The results from heating mode also demonstrate that GRCM performance maps accurately captured the PCM-HX behavior, being fully discharged during window operation hours.

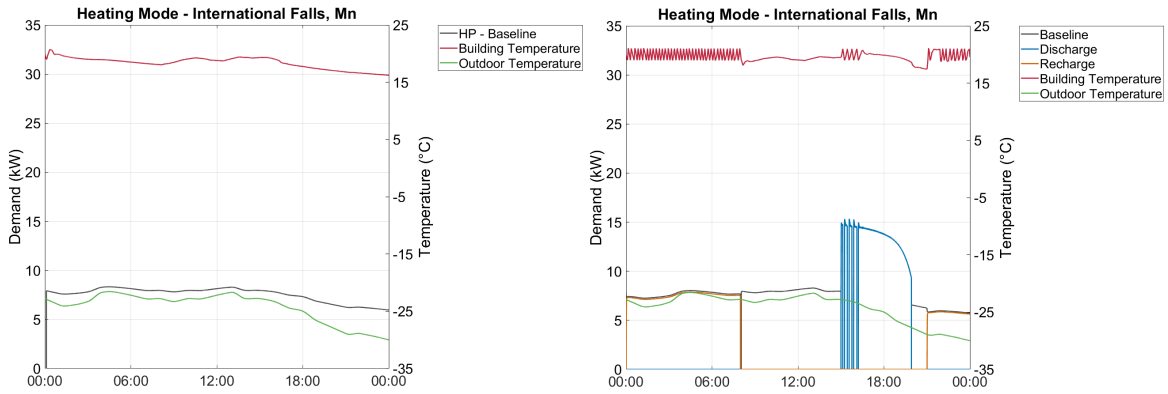

Figure 56. Baseline HP and TES capacity (left); HP-TES cooling capacity, indoor setpoint temperature and dry bulb temperature (right) for heating mode in International Falls, Mn

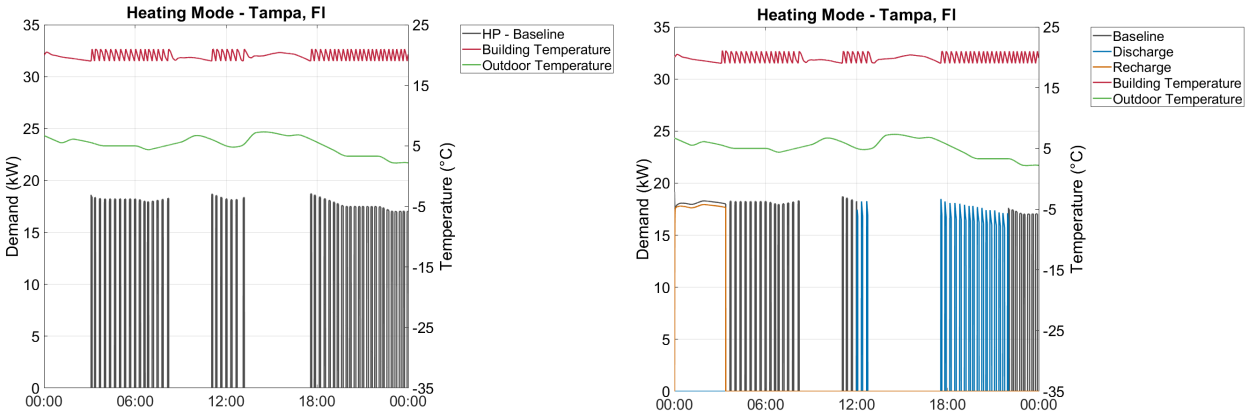

Figure 57. Baseline HP and TES capacity (left); HP-TES cooling capacity, indoor setpoint temperature and dry bulb temperature (right) for heating mode in Tampa, FL

PCM-HX Manufacturing (M1.1, M1.4, M2.2, M3.1)

The manufacturing efforts for this project are listed below. A detailed report on each effort is included in the following section.

- (M1.1) First-order analysis of PCM-HX configurations;
- (M1.4, M2.2, M3.1) Fabrication (and testing) of PCM-HX geometries;
- (M3.3) Cost assessments of at-scale PCM-HX manufacturing.

First Order Analysis of PCM-HX Configurations (M1.1)

To identify the most promising PCM-HX heat transfer enhancement techniques, a first-order analysis was conducted on the configurations shown in Figure 58, to provide a simplified, approximate evaluation of performance trends for rapid comparison of multiple design options. This type of comparative analysis across several PCM-HX configurations is lacking in the existing literature. Two container shapes (circular and rectangular) and various fin shapes were considered. For all configurations, the container volume and material volume (tube + fin) were held constant, thus ensuring the same PCM volume. The goal was to determine which configuration offers the largest heat transfer area without compromising the energy storage capacity of the PCM-HX.

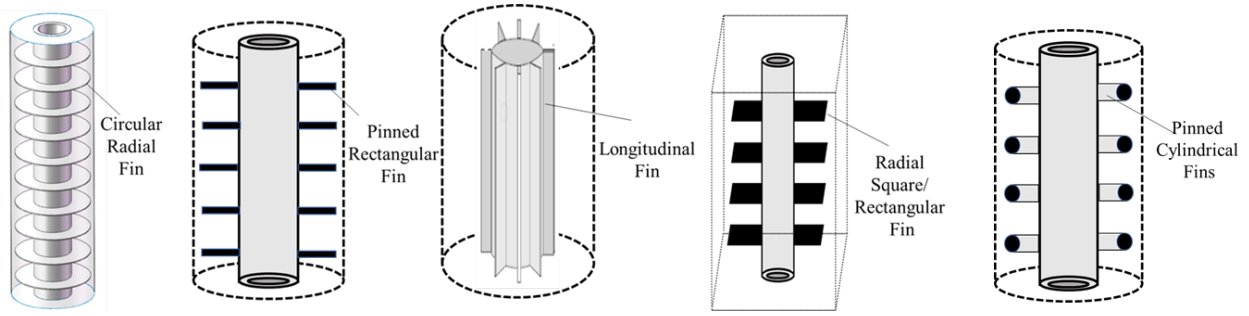

Figure 58: Different PCM-HX configurations for first order analysis

This is illustrated using the compactness parameter, defined as the ratio of total heat transfer area (between metal and PCM) to total container volume. Figure 59 presents the compactness of different configurations as a function of container volume. Results show that the circular radial fin configuration achieves significantly higher compactness at smaller container volumes. Figure 60 compares the effective compactness of all configurations relative to the circular radial case. As container volume increases, both pinned fin configurations (rectangular and cylindrical) exhibit higher compactness than the other designs.

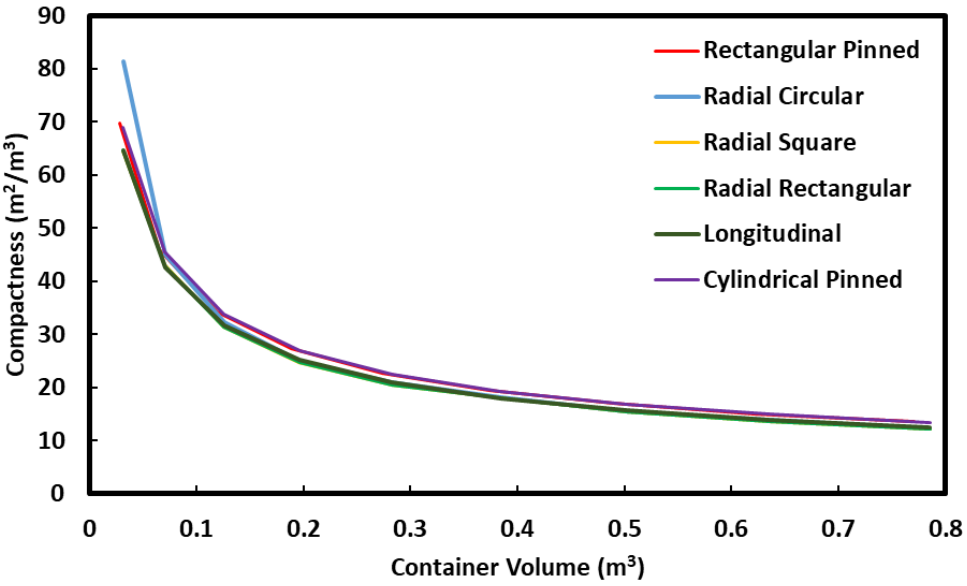

Figure 59: Compactness for different PCM-HX configurations

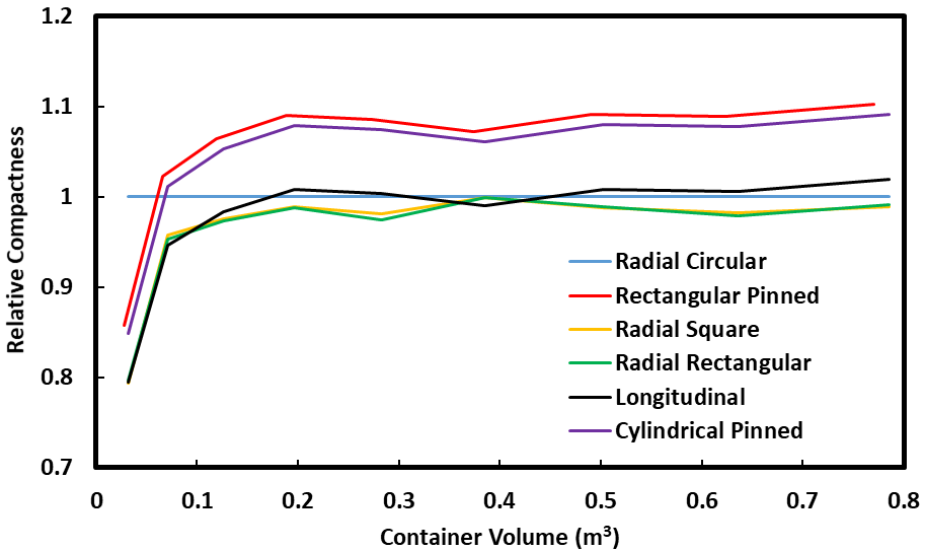

Figure 60: Relative compactness for different PCM-HX configurations compared to radial circular fin

Another first order analysis was performed on various HX geometries to determine the most promising ones apart from cylindrical tube-fin PCM-HXs. An annular finned PCM-

HX, serpentine microchannel, wire fin, crimped fin, spine fin and flat plate HX geometries have been looked into for a first order analysis. The geometries considered in this study are shown in Figure 61.

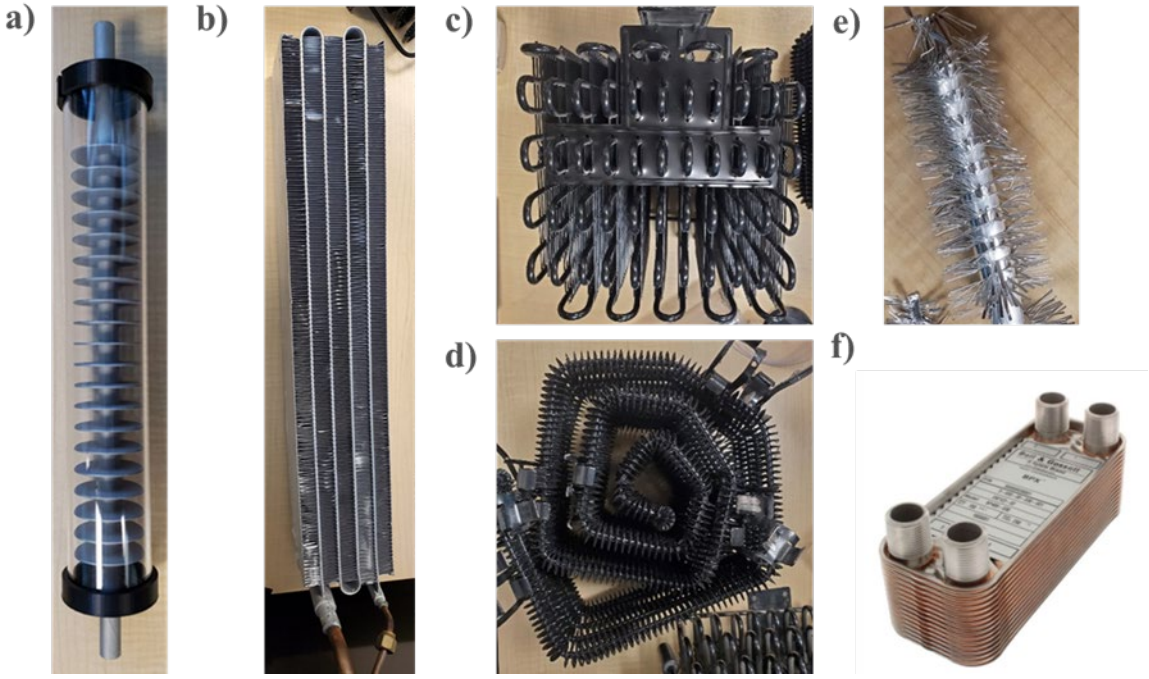

Figure 61: PCM-HX geometries considered for first order analysis a) Annular fins b) Serpentine microchannel c) Wire fins d) Crimped fins e) Spine fins f) Flat plate

This first order analysis considered the following metrics: compactness, material utilization and storage availability, defined as follows:

$$\text{Compactness}=\frac{\text{Heat transfer area}}{\text{Container volume}};\ \text{Material Utilization}=\frac{\text{Heat transfer area}}{\text{Material volume}};\ \text{Storage Availability}=\frac{\text{PCM volume}}{\text{Container volume}}$$

To compare the compactness and material utilization of different geometries, the storage availability of all configurations was fixed at 86%, fixing the same porosity to that of the annular finned PCM-HX. Achieving this required adjusting various geometric parameters, e.g., fins per inch, number of tubes, etc. Figure 62 presents the compactness and material utilization for each geometry under this constraint. The results suggest that the serpentine microchannel and spine fin configurations are especially promising, offering up to three times the compactness and material utilization of the annular finned design. However, it is important to emphasize that this is a first-order analysis intended to guide the selection of candidate geometries; actual performance comparisons may yield different outcomes.

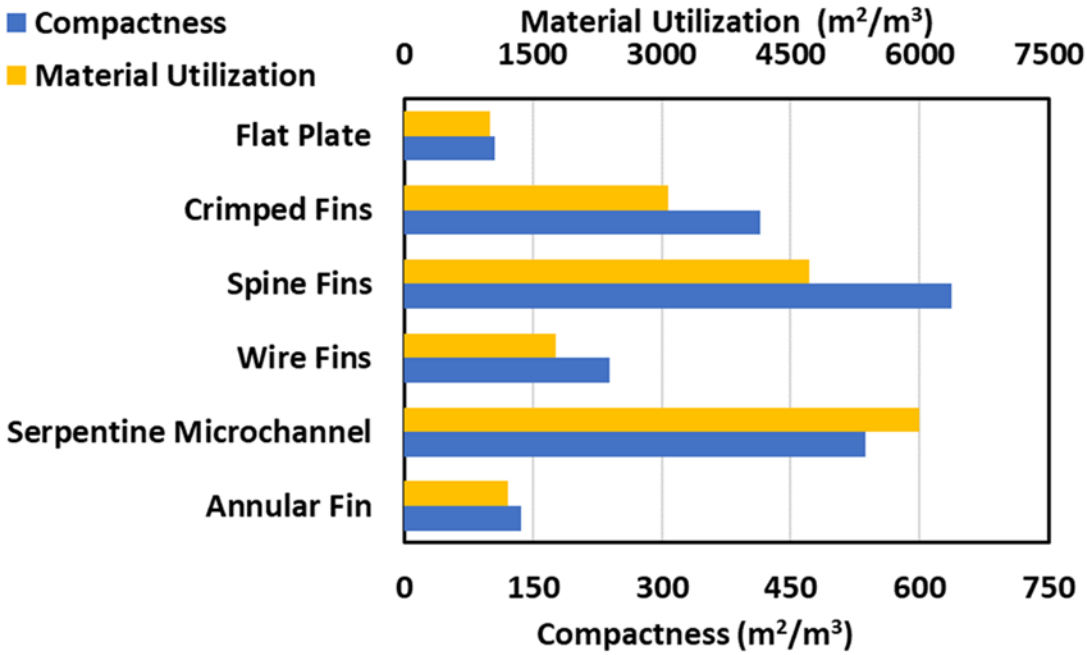

Figure 62:Comparison of compactness and material utilization for different PCM-HX geometries

Recommendations for PCM-Embedded HXs (M1.4, M2.2, M3.1)

Prom past HTT experience, the following HX type and geometry may be most suitable as an embedded HX in PCM: (i) Annular Fin-Tubes, here 3D printed by i.materialise, (Figure 63, top) and (ii) Serpentine Flat-Tube HXs (Figure 63, bottom), which are used in the automotive industry as the evaporator for the cabin air conditioning system. Such design could be optimized for best suitability as an embedded HX in PCM. Fin height and density, tube width and thickness can be varied for best performance as a thermal storage device

Figure 63: (Top) Annular-Fin Tube; (Bottom) Serpentine Flat-Tube HX.

The following heat exchanger types are promising when considered to be embedded in PCM for the low volume they occupy and/or their high thermal efficiency:

- Type 1: Serpentine / Wire condenser is low-cost and will only occupy a small volume when embedded in PCM. This type of HX is used in refrigerators as a condenser (Figure 64, left).
- Type 2: Tube with conical discs HX. This type of HX is used in refrigerators as a condenser unit. This HX will occupy more volume than a wire-HX but will also have higher thermal efficiency (Figure 64, middle).
- Type 3: Serpentine-tube dogbone-fin HX, commonly found as a refrigerator evaporator/freezer. Having flat fins, this heat exchanger will have increased thermal efficiency over prior designs. This type of HX also has low fin density thus will occupy low volume when embedded in PCM. This type of heat exchanger is also low-cost and lightweight (Figure 64, right).

Figure 64: (Left) Serpentine Wire Condenser; (Middle) Conical Disc HX; (Right) Serpentine-tube dogbone-fin HX.

- Type 4: Serpentine flat-tube HX (Figure 63, bottom), which occupy more volume than a tube/cone disc-HX with considerably higher thermal capacity.

For the serpentine-tube dogbone-fin HXs in particular, a brazed version may be more advantageous than the current mechanically-joint type to increase its life in a TES environment. HTT identified a means to braze an existing such mechanically-assembled HX, i.e., to have a brazed joint between the tube and fin, braze alloy needs to be placed near the fin collars, hugging the tubes.

A 1.5mm diameter braze wire with alloy 4045 was located and purchased. This braze wire is then placed along the tubes (Figure 65). When melted, the wire will join the fin collar to the tube all around the fin collar by capillary. The HX will need to be turned over and wire applied to the other side of the dogbone and brazed again.

Figure 65: Proposed Brazing Location for Dogbone-Fin HXs.

A 4-row serpentine-tube dogbone-fin HX was laid with brazing wire and fluxed for brazing (Figure 66). Out of 13 collar joints, 7 are brazed, 6 are partially brazed but still tight on tube (Figure 67). Braze rod did not distribute evenly to collars during melting. Some collars have heavy joint (red), some light (green) and some none (blue).

Figure 66: Dogbone-Fin HX (Pre-Brazing).

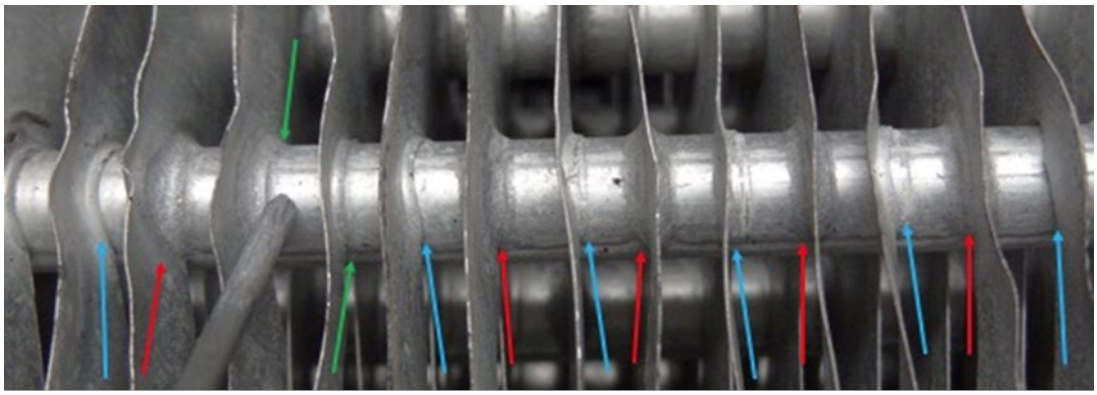

Figure 67: Dogbone-Fin HX (Post-Brazing).

The sample HX was cut in half along tubes (Figure 68) Red dots indicate no braze at that point (two points for each side of collar).

Figure 68: Dogbone-Fin HX Cut in Half (Post-Brazing).

PCM-HX Prototypes Summary (M1.4, M2.2, M3.1)

This project resulted in 9 PCM-HX prototypes fabricated using conventional and additive methods: 1 straight annular tube (finless); 3 annular fin-tube; 1 helix tube; 1 serpentine flat tube; 1 microchannel HX; 2 longitudinal fin tube (Figure 69).

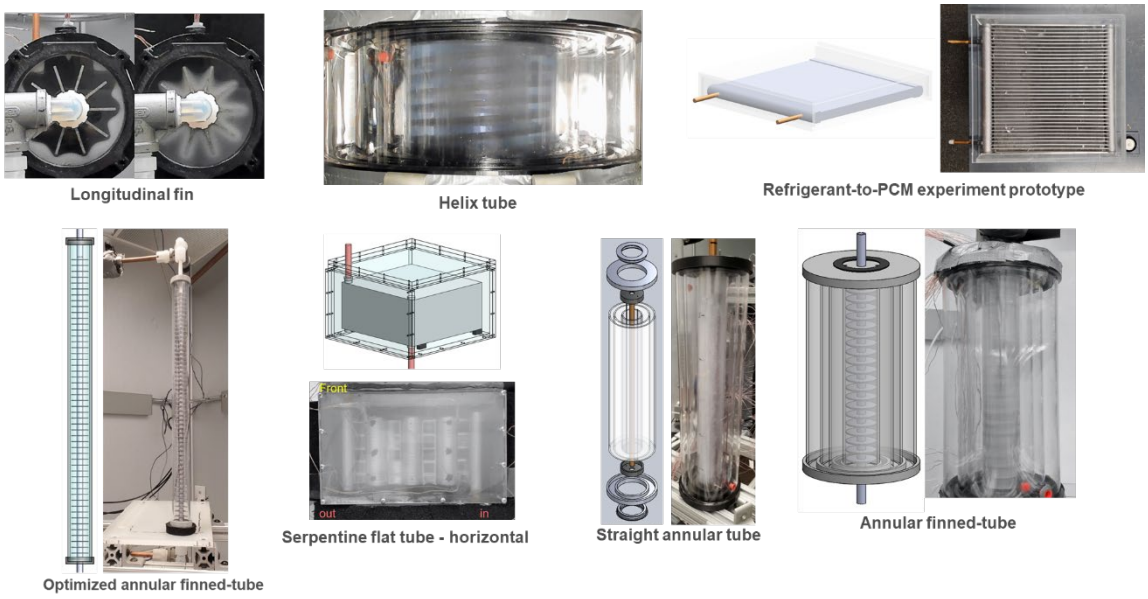

Figure 69:PCM-HX Prototypes

Straight Annular Tube PCM-HXs

A total of 4 straight tube PCM-HXs were constructed: 1 without fins and 3 with annular fins. Since the only difference between the two PCM-HX configurations is whether the tube does or does not have fins, the manufacturing process is very similar. To this end, we do not discuss the finless design and instead focus on the finned designs.

3D-Printed Annular Fin-Tube PCM-HX

An aluminum cylinder with annular fins was 3D printed for use as a PCM-HX. A polycarbonate cylinder was selected as the PCM container, while 3D printed acrylonitrile butadiene styrene (ABS) was used for container covers. Further configuration details can be found in Table 37 and Figure 70.

Table 37: 3D-Printed Annular-Fin Tube PCM-HX Dimensions.

Cylinder length [mm]	285
PCM container diameter [mm]	50.8 [OD], 44.5 [ID]
Tube diameter [mm]	12.7 [OD], 9.7 [ID]
Fin diameter [mm]	42.45
Fin thickness [mm]	1.5
Fin spacing [mm]	12.7
PCM liquid level from the top [mm]	35
Charged PCM mass [g]	246.4
PCM volume up to liquid level [cm^3]	320
PCM inner container volume up to liquid level [cm^3]	388.4
PCM-HX porosity [%]	82.4

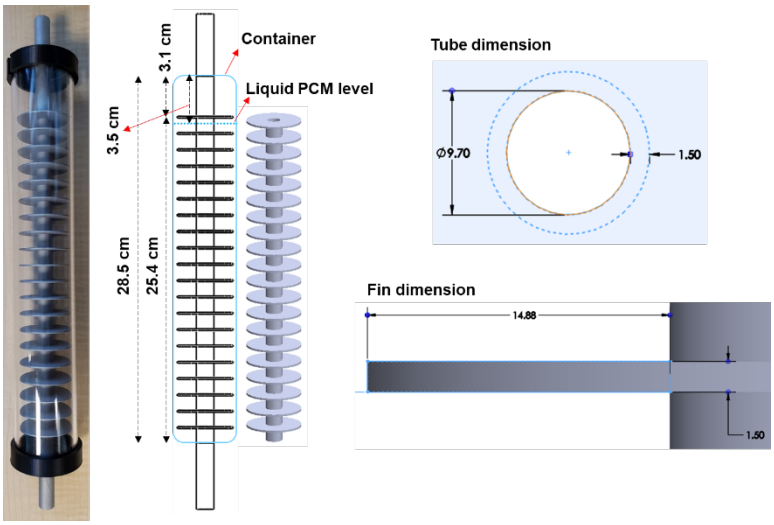

Figure 70: 3D-Printed Annular-Fin Tube PCM-HX schematic.

All PCM-HXs are surrounded by an insulation cylinder during testing to prevent heat loss to the ambient. The 3D-printed annular-fin tube PCM-HX insulation cylinder is described in Table 38 and Figure 71. Polycarbonate cylinders were again used as an insulation cylinder material. Argon gas was charged into the 2nd and 3rd insulation cylinders, while air was used to fill the 1st insulation cylinder. Insulation covers were 3D printed with ABS material. Also, 3D printed rubber gaskets were used to hold the insulation cylinders and PCM-HX container together. Lastly, two pairs of circular insulation sheets (6.35 mm for each sheet) were used to cover the top and bottom side of the assembly.

Table 38. 3D-Printed Annular-Fin Tube PCM-HX: Insulation cylinder dimension.

Length [mm]	285
1st cylinder diameter [mm]	82.1 [OD], 72.4 [ID]
2nd cylinder diameter [mm]	123.2 [OD], 114.1 [ID]
3rd cylinder diameter [mm]	160.3 [OD], 151.1 [ID]

Figure 71: 3D-Printed Annular-Fin Tube PCM-HX Insulation cylinder assembly: (L) 3D model and (R) actual assembly.

Copper Sponge Annular Fin-Tube PCM-HX Prototype

A second annular fin-tube PCM-HX prototype was manufactured by adding copper foam to the 3D-printed annular fin PCM-HX above (Figure 70). The copper sponges were evenly distributed inside the spaces between the fins. The setup was prepared that the PCM-HX porosity was almost identical to the value of the previous regular finned-tube setup (89.7%). The ratio of total added mass of copper sponges to the PCM mass were 10.3%, as shown in Table 39 and Figure 72.

Table 39: PCM-HX dimensions

Cylinder length [mm]	285
PCM container diameter [mm]	50.8 [OD], 44.5 [ID]
Tube diameter [mm]	12.7 [OD], 9.7 [ID]
Fin diameter [mm]	42.45
Fin thickness [mm]	1.5
Fin spacing [mm]	12.7
PCM liquid level from the top [mm]	32
Charged PCM mass [g]	247
PCM volume up to liquid level [cm^3]	324.2
PCM domain total volume up to liquid level [cm^3]	361
PCM-HX porosity [%]	89.8
Copper sponge to PCM mass ratio [%]	10.3

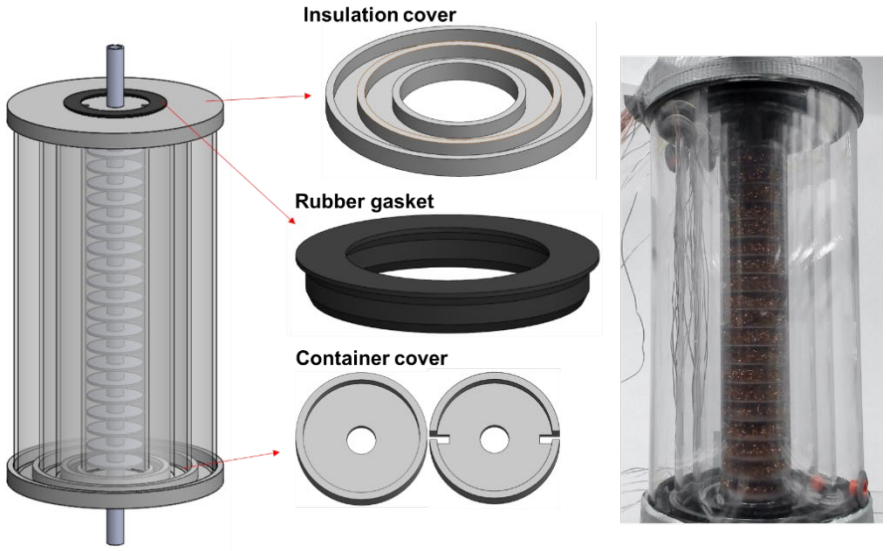

Figure 72: Copper Sponge Annular Fin-Tube PCM-HX Prototype

Optimized Annular Fin-Tube PCM-HX

A single unit of the PCM-HX design from the annular fin-tube PCM-HX optimization for domestic water heater application discussed herein was prototyped for experimental assessment. The PCM-HX dimensions are described in Table 40.

Table 40: Optimized Annular Fin-Tube PCM-HX dimensions & Schematic

Container Length [mm]	475.2
Container Diameter [mm]	31.75 [ID], 38.1 [OD]
HX Tube Diameter [mm]	7.75 [ID], 9.53 [OD]
Fin Diameter [mm]	27.75
Fin Thickness [mm]	0.25
Fin Pitch [mm]	8.67
Number of Fins	52
PCM Mass [g]	272.6
Charged Liquid PCM level [mm]	460.2
Ratio of PCM Volume to Container Inner Volume [%]	89

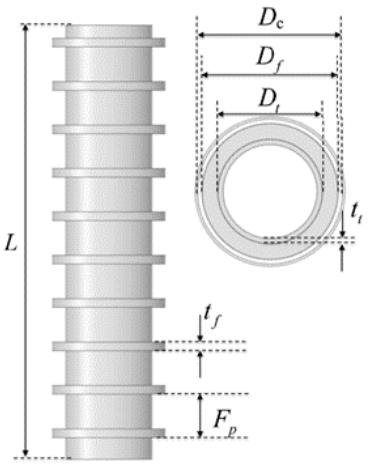

An annular fin-tube was built and brazed by HTT, as follows:

- The HX has 52 “disc fins” (supplied by UMD) on a 3/8” OD aluminum tube.
- A slotted aluminum “C” channel jig was made in order to hold the disc fins at the correct pitch (Figure 73)
  - The slots were made with a 0.4mm thin blade so to hold the discs straight.
  - Special braze clips were made with a specially-made tool to ensure the braze wire is in contact with the disc so the braze alloy is where it is needed.
  - Extra tube length is provided on each end per design.

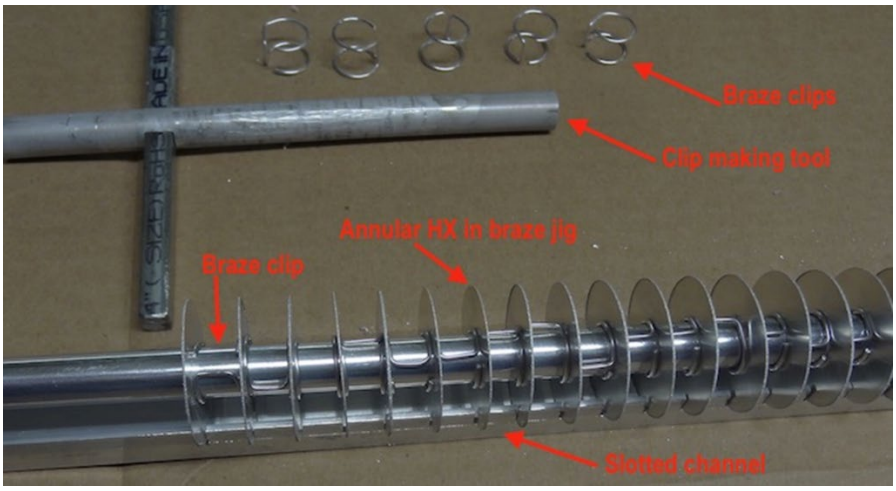

Figure 73: Optimized annular fin-tube assembly

- The annular fin-tube was fluxed and placed in the nitrogen atmosphere furnace (Figure 74).

Figure 74: Optimized annular fin-tube assembly in brazing furnace.

The completed annular fin-tube brazed very well, with nice braze fillets around each disc to tube joint (Figure 75). After shipping to UMD, the part was checked for quality before integration into the test facility. An impact resistant polycarbonate cylinder (Figure 76) was used as the container material for the PCM-HX. Container covers and turbulator inserts were 3D printed using ABS material. The setup was mock assembled before the charging the PCM into the container for leak checks.

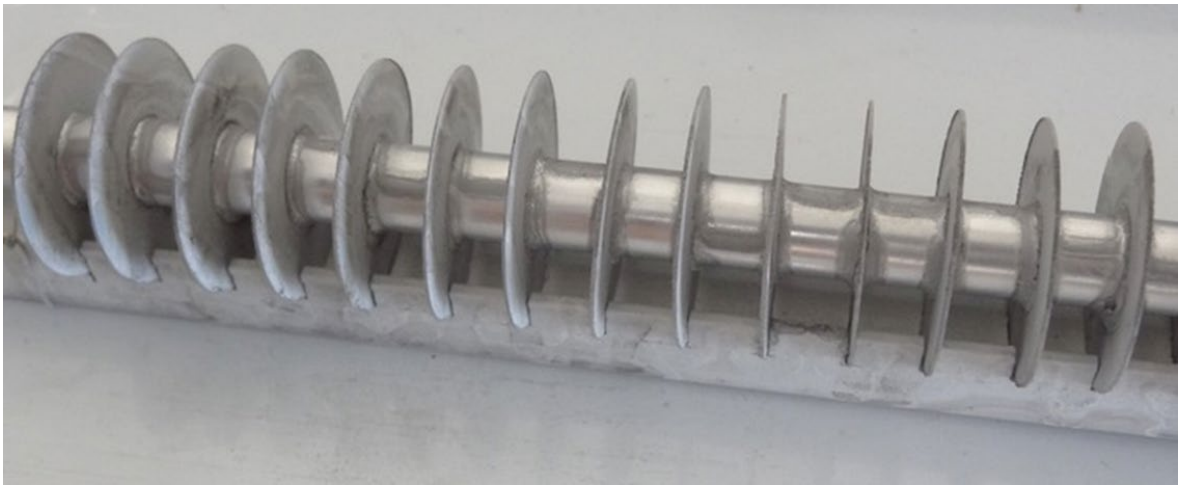

Figure 75: Optimized annular fin-tube assembly: post-brazing.

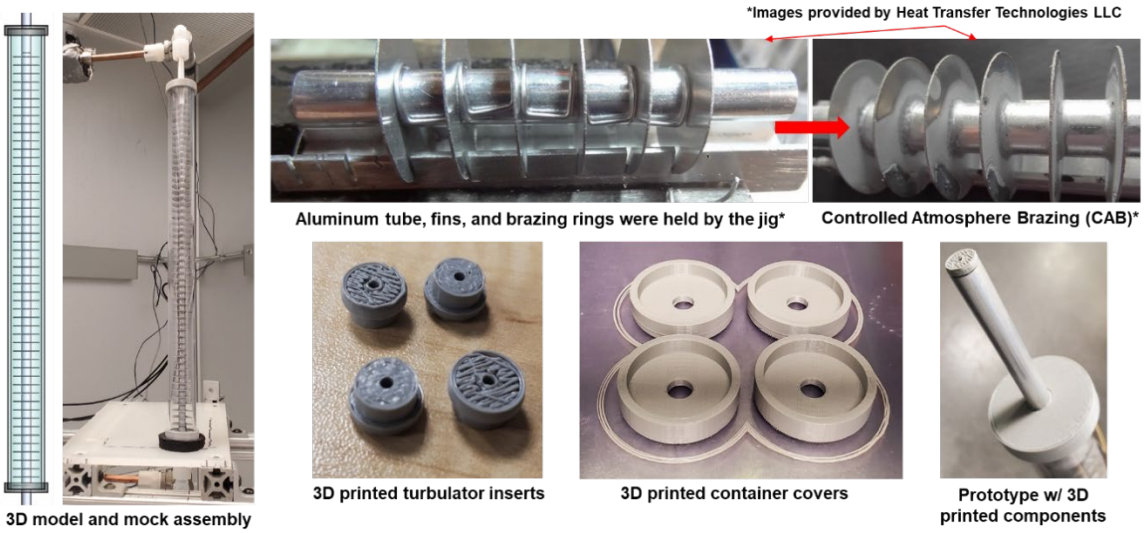

Figure 76: Optimized annular fin-tube PCM-HX components & final assembly.

Helix Tube PCM-HX

A PCM-HX with a copper helix tube was constructed by HTT per the following procedure:

- A custom base was constructed (Figure 77) to ensure a good seal with the inner and outer PVC cylinders.

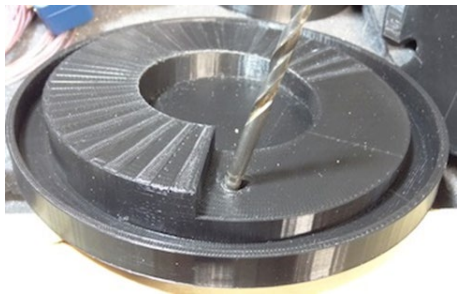

Figure 77: Helix Tube PCM-HX base.

- A copper winding tool was 3D-printed to aid in the production of the copper coil, which fit exactly when centered inside the PCM-HX (Figure 78).

Figure 78: Helix Tube PCM-HX: Coiled copper tube.

- Thermocouples were added by machining channels into the clear PVC pipes to embed the wires (Figure 79).
    - The thermocouple end tip was bent using a tool to ensure all thermocouples extend into the PCM the same amount.
    - Thermocouple wires were laid and glued inside the channels, while temporary tape was used to hold the thermocouples and wires in place.

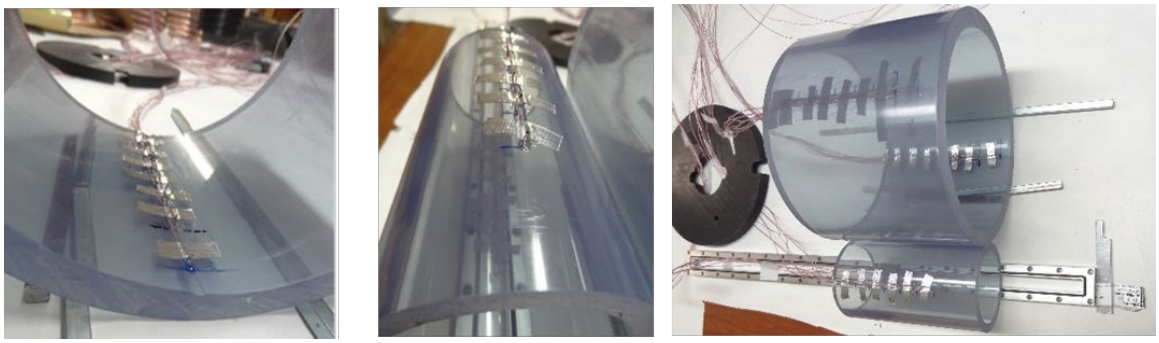

Figure 79: Helix Tube PCM-HX: Thermocouple Installation.

- Once cured, the PVC pipes were placed and glued to the bottom cap (Figure 80).

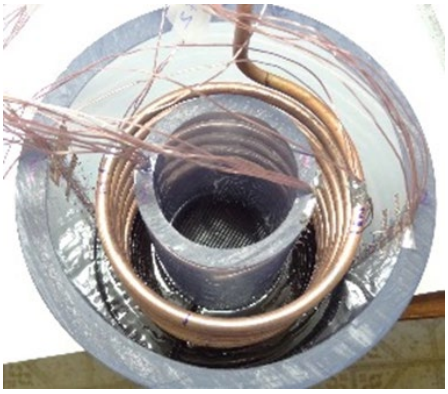

Figure 80: Helix Tube PCM-HX: Final assembly.

Serpentine Flat-Tube PCM-HX Prototype

A commercially-available serpentine tube HX consisting of 21 individual rectangular channels was utilized as a PCM-HX. The detailed dimensions and its configuration is shown in Table 41 and Figure 81. It is important to mention that the header-side aluminum tubes that were part of the original configuration were later removed and replaced with straight copper tubing to reduce unnecessary tube lengths before the HX inlet and outlet measurement points and to make the overall PCM-HX assembly simpler.

Table 41: Serpentine Flat-Tube HX dimensions.

Width [mm]	210
Length [mm]	210
Height [mm]	100
Single rectangular channel dimension [mm]	3 x 4

Number of rectangular channels	21
Fin thickness [mm]	0.15
Regular fin pitch [mm]	2.3
End-side fin pitch [mm]	1.7
Number of regular fins	518
Number of end-side fins	192
Header-side copper tube diameter [mm]	12.7 [OD], 11.1 [ID]

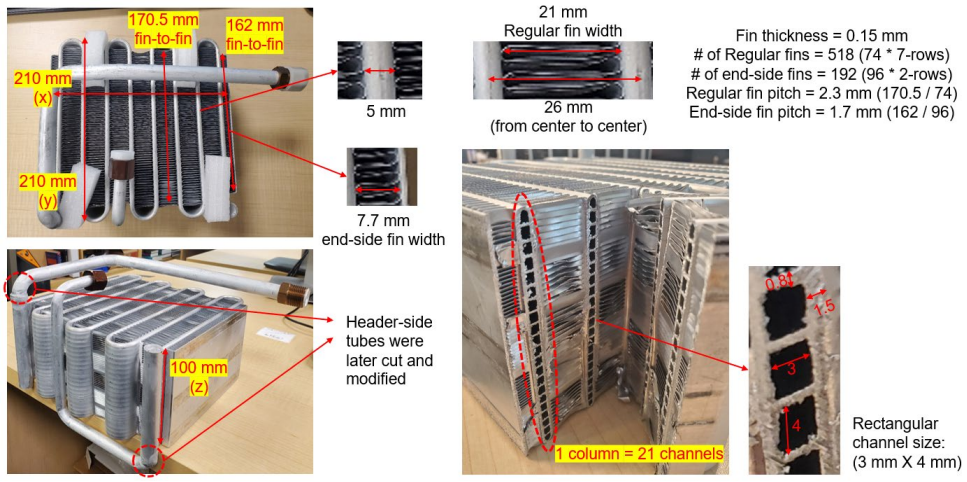

Figure 81: Serpentine Flat-Tube HX: specifications.

Clear high-strength acrylic plates were used as container walls, cut to the designed dimensions using a laser cutting machine, while the screw holes on the plates were made by the accurate milling machine. Modified acrylic plates were later assembled with the screws and acrylic epoxy for the container construction. The detailed dimensions of the container's inner volume are shown in Table 42. A 10 mm gap between the heat exchanger surfaces and the inner wall of the container was given around all heat exchanger surfaces except for the top surface. For the bottom gap, small 3D-printed blocks were attached to the bottom surface of the heat exchanger. The height of the container's inner volume was designed to have at least a 15 mm air gap at the top to prevent any unexpected PCM leakage through the top plate.

Table 42. Serpentine Flat-Tube HX Container Dimensions

Width [mm]	230
Length [mm]	230
Height [mm]	140
Acrylic plates thickness [mm]	8.73
Gaps between the inner walls and the heat exchanger surfaces – front, back, left, right, and bottom [mm]	10
PCM liquid level [mm]	125

A 3D model of the container and heat exchanger assembly is shown in Figure 82. The front and top surfaces, which were used for visual observation angles, were double-plated to increase the thermal resistance while maintaining transparency. The rest of the single acrylic plates were later covered with 1" thick insulation sheets.

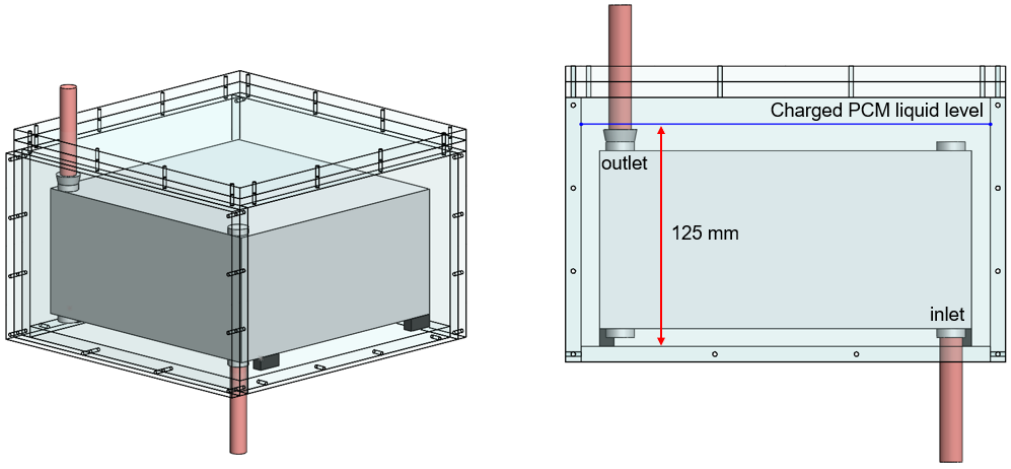

Figure 82: 3D model of Serpentine Flat-Tube PCM-HX assembly.

Microchannel PCM-HX Prototype

A Danfoss microchannel HX was configured into a PCM-HX in a similar manner as the serpentine flat-tube PCM-HX. As displayed in Figure 83, the 3D model of the designed PCM-HX assembly is shown along with the acrylic plates that were laser-cut to match the designed dimensions.

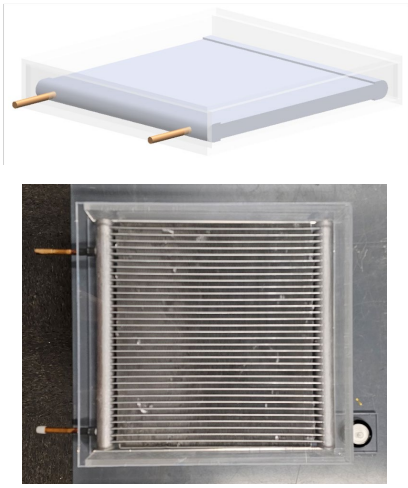

Figure 83: (TOP) Schematic view of Microchannel PCM-HX; (BOTTOM) Microchannel PCM-HX inside acrylic container.

Longitudinal-Fin PCM-HX Prototypes

Two longitudinal fin PCM-HXs, a baseline design and melting-case topology optimized design described by Pizzolato et al. [186], were fabricated via 3D printing from i.materialise in aluminum (AlSi10Mg). The authors reported that the optimized design had 37% shorter melting time compared to the baseline design. The 3D printing order was made and received by Heat Transfer Technologies, LLC, then the units were shipped

again to CEEE. The CAD designs of both units that were created based on the study from by Pizzolato et al. [186] and the actual fabricated units are shown in Figure 84 and Figure 85. The 3D-printed tubes were measured digital caliper, showing a close match to the designed dimensions. The 3D design of the final PCM-HX assemblies with the individual components and its cross-sectional images are shown in Figure 86.

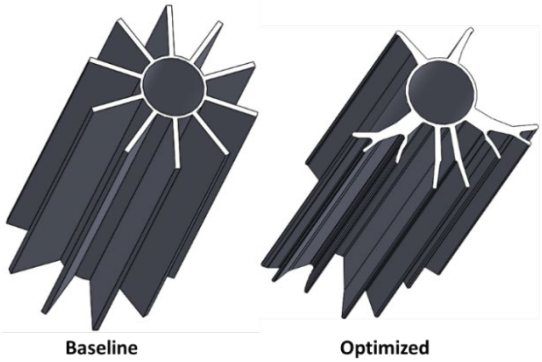

Figure 84: Longitudinal Fin 3D models: (Left) Baseline; (Right) Topology-optimized [186]

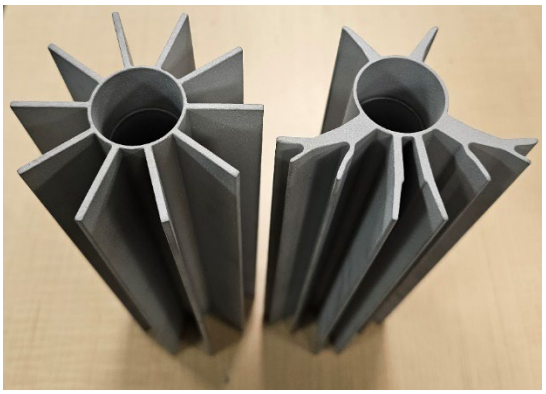

Figure 85: 3D-Printed Longitudinal Fin Tubes.

Figure 86: (L) 3D Model of Longitudinal Fin PCM-HX Assembly; (R) Acquired parts.

Cost Assessment of At-Scale PCM-HX Manufacturing (M3.3)

Initial Cost Assessment of Relevant Storage Tanks

An initial cost comparison study of relevant storage tanks was performed by HTT using past experience and cost (Figure 87). Using the heat pump water tank (Column D) as the baseline:

TES Cost Comparison by System

8-Jul-21	C	D	E	F	G	H
Technology	**Sensible**	**Sensible**	**Latent**	**Latent**	**Latent**	**Latent**
Storage material	**Water storage tank**	**Heat Pump Water Heater Storage tank**	**PCM + RTPF HX storage tank**	**PCM in Graphite block + RTPF HX storage tank**	**PCM with Graphite shavings + AlMC HX storage tank**	**PCM + ALMC HX storage tank**
Description	Coated steel tank	Coated steel tank with outer coil	Copper HX in PCM	Copper tube HX embedded in graphite PCM block	AlMC HX embedded in graphite shavings+PCM	AlMC HX embedded in PCM
kJ/kg	75.6	75.6	256.2	227.2	227.2	256.2
Material Density [kg/l]	1	1	0.82	0.925	0.925	0.82
Energy density [kWh/m3]	**23.10**	**23.10**	**50.75**	**50.76**	**50.76**	**50.75**
kg needed per kWh	47.61	47.61	14.05	15.84	15.84	14.05
Cost per kg	$ 0.00054	$ 0.00054	$ 2.64	$ 5.00	$ 3.00	$ 2.64
Storage Material per kWh	$ 0.02	$ 0.02	$ 37.09	$ 79.20	$ 47.52	$ 37.09
Steel tank	$ 13.25	$ 13.25				
Container			$ 11.88	$ 11.88	$ 11.88	$ 11.88
HX		$ 7.57	$ 39.25	$ 39.25	$ 13.00	$ 13.00
Insulation	$ 4.00	$ 4.00	$ 4.00	$ 4.00	$ 4.00	$ 4.00
Total, $ per kWh	**$ 17.27**	**$ 24.84**	**$ 92.21**	**$ 134.33**	**$ 76.40**	**$ 65.96**
10kWh storage, [$]	$172.70	$248.41	$922.11	$1,343.28	$763.97	**$659.61**
10kWh storage, [m3]	**0.43**	**0.43**	**0.20**	**0.20**	**0.20**	**0.20**

kJ/kg: Graphite block occupies 20% of volume

kJ/kg: Graphite shavings occupy 20% of volume

Notes: Materials for a 8kWh storage:		**Source:**
Average $1.52 per 1000 gal. water		
Steel tank $106	$106.00	(Golden Dragon)
Cu-Al HX $314	$314.00	(New Eenergy)
AL MC HX $104	$104.00	(HTT)
Copper tube winding in HPWH $6	$60.57	(Golden Dragon)
Insulation $32	$32.00	(Golden Dragon)
Metal container for PCM	$95.00	(New Energy)

Figure 87: TES Cost Comparison by System

- Energy Density: Temperature range used is the useful 58C to 40C. Water (Columns C, D) has only sensible Cp_w (58-40). PCM has sensible and latent heat: Cp_p (52-40) + Latent heat at 53°C for Puretemp RT53.
- Volume: PCM + aluminum MCHX (Columns G, H) is 46% smaller than baseline.
- Cost: The overall objective is to achieve a simple payback period of no more than 5 years. The PCM+aluminum MCHX (Column H) cost is ~2.7x higher than the baseline for the same capacity (10kW).
    - However, a PCM system occupying a smaller space in a building has significant value.

The average U.S. Construction cost for apartment buildings is: (i) Mid-rise (<10 stories, 50-200 units) = $175 – $250 per sq ft and (ii) High-rise (>12 stories 4-20 units/floor) = $225 – $400 per sq ft (Figure 88, top left), which scales depending upon the city and energy efficiency ratings of interest (Figure 88, top right & bottom), e.g.,

- Construction cost in major cities like London, Hong Kong, New York can range 2X higher than the average (Figure 88, bottom).
- E.g., in Washington, D.C., construction costs per sq ft increase from 12% with LEED Platinum, 24% with Net Zero Energy, 30% with Living (Figure 88, top right).

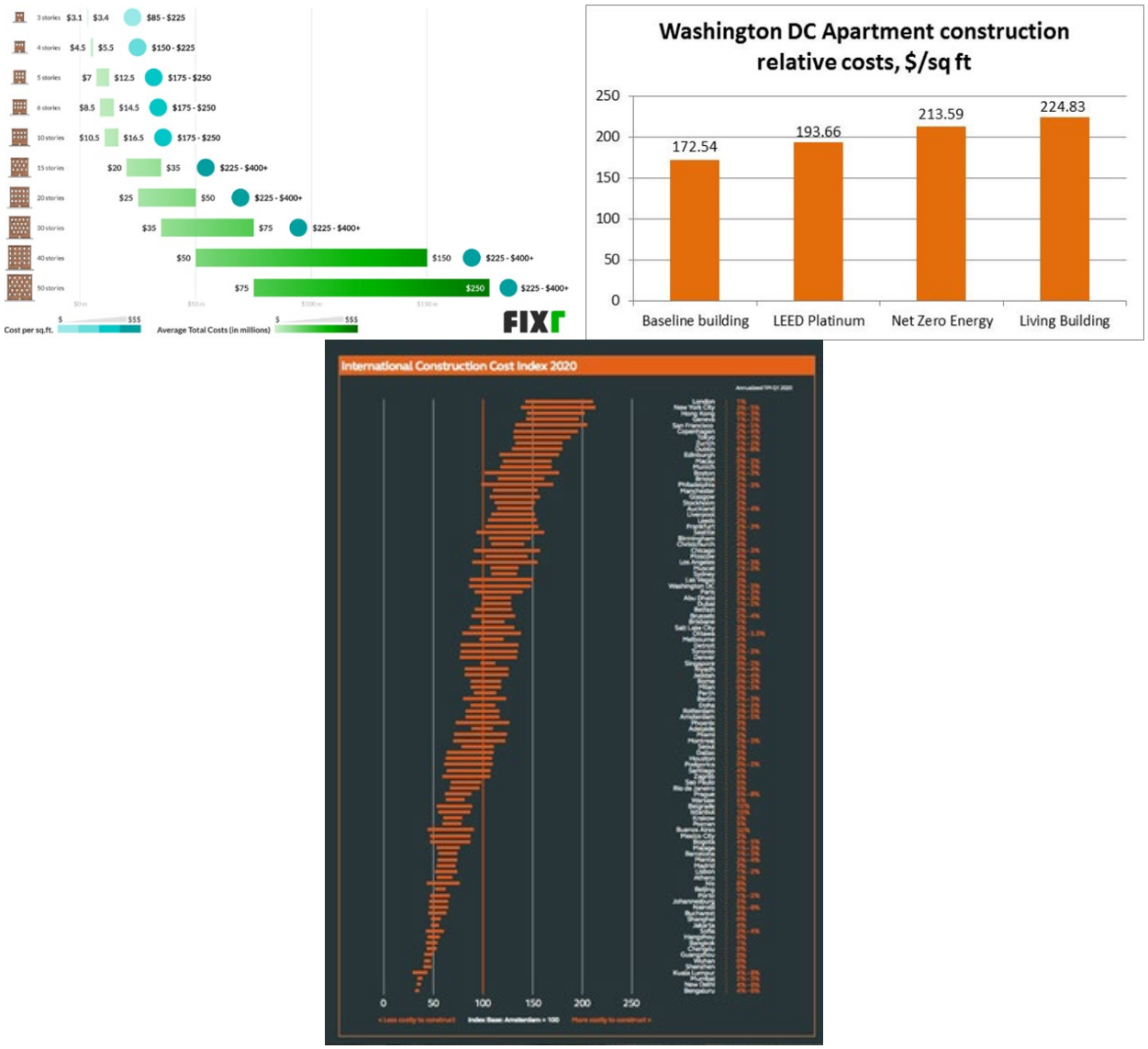

Figure 88: (Left) 2021 Apartment Construction Cost by Stories (source: fixr.com); (Right): Relative construction cost per sq ft in Washington D.C in 2021.

Economy of Scale for PCM-HX Prototypes

Aluminum MCHX-based PCM-HXs

The economy of scale for the production of controlled atmosphere brazed (CAB) aluminum microchannel heat exchangers is a critical factor influencing their widespread adoption, especially in cost-sensitive industries like residential HVAC and automotive.

- High Initial Manufacturing Cost:
  - Complexity: Microchannel heat exchangers (MCHEs) are inherently complex due to their intricate designs, small channel networks, and tight tolerances.1 This complexity drives up manufacturing costs.1, 2

  - Specialized Processes: They require specialized manufacturing techniques, advanced machinery, and skilled labor. Controlled Atmosphere Brazing (CAB) itself is a precise process involving specific furnaces, fluxing, drying, brazing (typically with aluminum-silicon clad material), and controlled cooling in an oxygen-free nitrogen atmosphere.3
  - Capital Investment: Setting up dedicated manufacturing facilities for extrusion (for the microchannels), brazing (CAB furnaces), and coating processes involves significant capital expenditure.
  - Material Costs: While aluminum is generally more affordable than copper, the specific alloys and cladding materials used in CAB, along with potential fluctuations in aluminum prices, contribute to the overall expense.
  - Comparison to Conventional HXs: Industry data suggests that MCHEs can be 20% to 30% higher in cost than conventional heat exchangers due to these factors.
- Economy of Scale - How Volume Reduces Cost:
  - Fixed Cost Amortization: The high initial capital investment in specialized equipment (like large, continuous CAB furnaces) is a fixed cost. As production volume increases, this fixed cost is spread over more units, significantly reducing the cost per unit.
  - Continuous Production Lines: CAB furnaces designed for high-volume production (e.g., continuous conveyor lines) are highly efficient.4 Once set up, they can process large quantities of heat exchangers with precise control over temperature and atmosphere. This continuity minimizes batch-related inefficiencies and labor costs per unit.
  - Throughput: Some manufacturers aim for very high throughputs, such as 500,000 units/year for automotive or residential applications, to drive down costs.
  - Labor Efficiency: In large-scale, often automated, production, the labor cost per unit decreases as workers become more specialized and processes are streamlined.5
  - Bulk Material Purchasing: Higher production volumes allow manufacturers to purchase raw materials (aluminum sheet, tubes, fins, flux, brazing alloys) in larger quantities, often at discounted rates.
  - Process Optimization: With higher volumes, there's more opportunity to fine-tune the manufacturing process, identify and eliminate bottlenecks, reduce scrap rates, and improve overall efficiency.
  - "Manufactured Cost" Estimates: For extruded microchannels, manufactured costs of ~$2–$4/lb (excluding capital cost/markup) have been cited for high-volume production (e.g., 500,000 units/year). This suggests that for larger, heavier units, the cost per unit would be higher, but still benefiting from scale.
- Market Growth and Cost Trends:
  - The global microchannel heat exchanger market is growing significantly (projected from USD 16.1 billion in 2023 to USD 26.3 billion by 2028, with a CAGR of around 10%).6 This growth is driven by demand for energy-

efficient, compact, and lightweight solutions in HVAC, automotive, and other industries.7
    - Increased demand leads to higher production volumes, which in turn helps to realize economies of scale and drive down unit costs.
    - Regions with high industrial expansion and lower labor costs (e.g., Asia-Pacific, particularly China, Japan, and India) are seeing rapid adoption and large-scale production facilities, further contributing to cost reduction.
- Conclusion
    - Controlled atmosphere aluminum microchannel heat exchangers are initially more expensive to manufacture than traditional heat exchangers due to their complexity and specialized processes (like CAB).
    - However, they exhibit strong economies of scale. As production volumes increase significantly, the cost per unit drops considerably due to the amortization of high fixed capital costs, efficient continuous manufacturing lines, bulk material purchasing, and optimized processes.
    - This makes them a more viable and competitive option for large-scale applications such as automotive cooling, residential HVAC, and commercial refrigeration, where their performance benefits (higher efficiency, lower refrigerant charge, compactness) can justify the initial investment.

References:

- https://www.china-sunco.com/product/microchannel-heat-exchanger/
- https://www.marketsandmarkets.com/Market-Reports/microchannel-heat-exchanger-market-32760657.html
- https://www.elconprecision.com/controlled-atmosphere-brazing-a-deep-dive-into-benefits-and-techniques/#:~:text=By%20maintaining%20precise%20control%20over,a%20wide%20range%20of%20critical
- https://blog.lucasmilhaupt.com/en-us/about/blog/benefits-of-controlled-atmosphere-brazing-in-automotive-manufacturing
- https://www.investopedia.com/terms/e/economiesofscale.asp
- https://www.marketsandmarkets.com/Market-Reports/microchannel-heat-exchanger-market-32760657.html
- https://www.kaltra.com/single-post/2020/02/24/microchannel-heat-exchangers-manufacturing-process

3D-Printed Metal PCM-HXs

The economy of scale for 3D printed metal heat exchangers is a complex topic, as additive manufacturing (AM) fundamentally changes the traditional cost curves associated with mass production. While AM offers significant advantages, it's not a straightforward "cheaper with higher volume" scenario as with conventional manufacturing methods like stamping or injection molding. Here's a breakdown of the economy of scale considerations for 3D printed metal heat exchangers:

- Demolishing Traditional Economies of Scale (for low to mid-volumes):
    - No Tooling Costs: Traditional manufacturing relies heavily on expensive tooling (molds, dies, jigs). These fixed costs are amortized over high production volumes, making each part cheaper as quantity increases. 3D printing largely eliminates tooling, meaning the per-part cost doesn't drop drastically with volume increases in the early stages.

  - Cost-Per-Part Linearity: For 3D printing, the cost-per-part curve tends to be more linear and only slightly decreasing as quantity increases, especially for complex designs. This means that the cost for a single highly complex heat exchanger can be almost the same as producing hundreds or even thousands of them (within the capacity of one machine).
  - Low-Volume Efficiency: This makes 3D printing highly competitive and cost-effective for:
    - Prototyping: Rapid and low-cost iteration of designs.
    - Low-Volume Production: Ideal for specialized heat exchangers used in aerospace, medical devices, high-performance computing, or niche industrial applications where quantities are not in the millions.
    - Customization: Producing bespoke heat exchangers tailored to specific application requirements without incurring significant re-tooling costs.
- Factors Influencing Cost at Scale in AM:
  - While traditional economies of scale are altered, other factors become critical for cost at higher volumes:
  - Machine Utilization: Maximizing the uptime and build volume of expensive 3D printing machines is key. Running multiple parts in one build (nesting) can optimize machine utilization and reduce per-part costs.2
  - Material Costs: Metal powders (e.g., Inconel, Titanium, Stainless Steel, Aluminum alloys) are significantly more expensive than raw materials used in traditional manufacturing. While AM reduces material waste, the base material cost remains a substantial factor. For example, titanium alloys can be over $360/kg, and Inconel around $145/kg (as of 2021 estimates).
  - Build Time: The speed at which parts can be printed (build rate) directly impacts cost. More complex parts, finer resolutions, and certain materials require slower build rates, increasing print time and operational costs. For heat exchangers with intricate internal structures, build times can be long.
  - Post-Processing: Metal 3D printed parts often require significant post-processing steps, including:
    - Support structure removal
    - Heat treatment (stress relief, strengthening)3
    - Surface finishing (e.g., machining, polishing, chemical treatment) to achieve desired roughness for fluid flow.4
    - These steps can be manual, time-consuming, and add considerable cost, impacting scalability.
  - Labor Costs: While AM can automate the printing process, skilled labor is still needed for machine operation, maintenance, design optimization, and post-processing.
  - Capital Expenditure (CAPEX): Industrial metal 3D printers are very expensive (e.g., Selective Laser Melting (SLM) printers can cost between €0.5-1.5 million). This high upfront investment needs to be amortized over the production volume.

  - Design Optimization for AM: Parts designed specifically for AM (topology optimization, lattice structures) can often reduce material usage and improve performance, which indirectly affects cost.
  - Energy Consumption: Metal AM processes are energy-intensive, and electricity costs contribute to the overall expense.
- Comparison to Traditional Manufacturing at High Volumes:
  - Break-Even Point: For very large production volumes of relatively simple heat exchanger designs, traditional manufacturing methods (like brazed plate-fin or tube-fin heat exchangers) are still generally more cost-effective due to their ability to leverage massive economies of scale from tooling and high-speed assembly.
  - Complexity vs. Cost: The key differentiator is complexity. If a heat exchanger design is so complex and optimized that it cannot be manufactured efficiently (or at all) by traditional methods, then 3D printing becomes the only viable option, and its cost becomes justified by the performance gains (e.g., 20% increase in efficiency and reduced weight/size reported by the University of Maryland).
- Future Outlook
  - The global market for 3D printed heat exchangers is growing rapidly (projected from USD 1.2 billion in 2023 to USD 4.8 billion by 2032).
    - As AM technologies mature, material costs decrease, and processes become faster and more automated, the cost-effectiveness of 3D printed metal heat exchangers will continue to improve.
    - Innovation in hybrid manufacturing processes (combining AM with traditional methods) and new polymer-based 3D printing with plating techniques also aim to reduce costs for high volumes.
  - For **high-performance, complex, and customized metal heat exchangers, 3D printing already offers significant value proposition regardless of high volume due to its unique design freedom and performance gains**.
    - However, achieving true "economy of scale" for commodity-level heat exchangers at extremely high production volumes (millions of units) is still a challenge for additive manufacturing compared to highly optimized traditional methods, though the gap is narrowing.

References:

- https://www.researchgate.net/publication/380660702_Potential_of_3D_Printing_for_Heat_Exchanger_Heat_Transfer_Optimization-Sustainability_Perspective
- https://www.weerg.com/guides/what-is-3d-part-nesting#:~:text=3D%20Nesting%3A%20Cut%20Costs%20by,20%2B%20Finishes
- https://www.eplus3d.com/heat-treatment-influence-on-metal-3d-printing-products.html
- https://www.tandfonline.com/doi/full/10.1080/17452759.2024.2364222
- https://www.emerald.com/insight/content/doi/10.1108/rpj-02-2021-0041/full/html#:~:text=The%20designs%20achieved%20in%20this,manufactured%20geometry%20designed%20using%20more
- https://library.fiveable.me/additive-manufacturing-and-3d-printing/unit-9/energy-consumption-additive-manufacturing/study-guide/dkLudRhGG0VhbbWV
- https://dataintelo.com/report/3d-printed-heat-exchanger-market

Annular Fin-Tube PCM-HX

The economy of scale for the annular fin HX is relatively simple: It is the cost of the metal + 20% in large scale production. Due to the simplicity of this type of heat exchanger, its high-volume cost is similar to costing tube production, which is the material cost + 10%, and an additional 10% is added for the brazing operation.

PCM-HX Experimentation

Note: The contents of this section have been published in the following citations: Yang et al. [187]*; Yang et al.* [187]*; Yang et al.* [188]*; Yang et al.* [158] *and Alam et al.* [142]

The experimental efforts for this project are listed below. A detailed report on each effort is included in the following section.

- (M1.4, M2.2, M3.1) (Fabrication and) Testing of PCM-HX geometries, including development of PCM-HX test facilities for single-phase and two-phase fluid to PCM heat transfer

PCM-HX Test Facility Development

Single-Phase HTF-to-PCM Experimental Facility

A test rig was developed to evaluate different types of PCM-HXs using single-phase fluids, e.g., water and/or glycols, as the heat transfer fluid. The test rig was installed inside a temperature-controlled environmental chamber. As shown in Figure 89, both the schematic diagram and actual images of the setup are presented. The major components of the test facility include a gear pump, Coriolis mass flow meter, air-to-HTF heat exchanger with a fan, electric heater, and the PCM-HX test section. Multiple resistance temperature detectors (RTDs), thermocouples, and pressure transducers were installed to enable detailed system performance analysis and to support PID control of both the HTF temperature and mass flow rate.

It is important to note that the HTF can travel in any direction in both vertical and horizontal orientation depending on the PCM-HX orientation with the help of the ball valves and 3-way valves near the PCM-HX test section. During the melting process, the HTF inlet temperature is controlled by the heater through PID logic. For the solidification process, the HTF inlet temperature is maintained by adjusting the ambient temperature in the chamber and operating the air-to-HTF heat exchanger with a fan.

To improve measurement accuracy, the test section includes subcomponents such as 90° elbows, RTD guides with multi-cord grips, and orifice-type turbulator inserts at both the inlet and outlet of the PCM-HX. Each temperature measurement location is instrumented with two sets of three RTDs to minimize systematic uncertainties. The in-house 3D-printed RTD guides support the RTDs concentrically inside the flow channel, preventing contact with the inner tube walls. The orifice-type turbulators locally increase the HTF velocity by narrowing the flow area, thereby enhancing mixing and improving temperature measurement accuracy, particularly under laminar flow conditions.

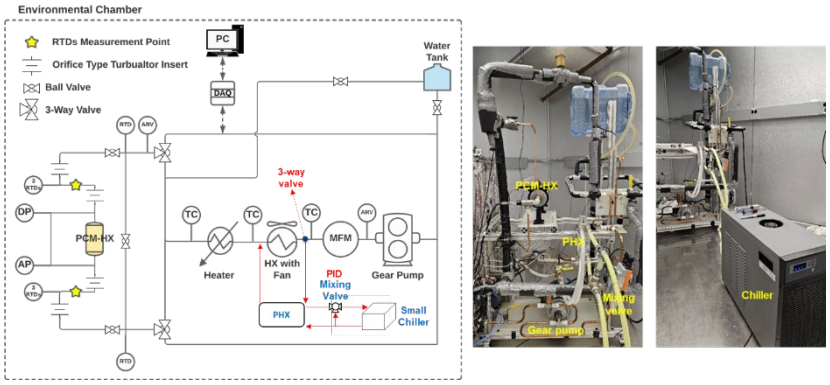

Figure 89: PCM-to-HTF Experimental Setup.

Two-Phase Refrigerant-to-PCM Experimental Test Facility

The schematic diagram of the test facility with utilizing two-phase refrigerant, shown in Figure 90 (top), comprises three main sections: the PCM-HX section, the refrigerant cart section, and the water/glycol section. The outdoor chiller, alongside automatically controlled diverging valves and an immersive heater, ensures precise temperature control of the water/glycol tank. This, in turn, regulates the temperature of the oversized condenser and its system pressure. The oversized condenser's substantial refrigerant volume allows it to function effectively as a large receiver, facilitating this temperature and pressure control of the system loop. Heat exchange within the water/glycol loop and its connected components is facilitated by plate HXs and circulation pumps. A small chiller cools the subcooler HX after the oversized condenser to prevent the refrigerant pump from running dry. The refrigerant flows through the mass flow meter and is heated to the desired target temperature before entering the PCM-HX test section. Initially, the refrigerant can bypass the main PCM-HX loop until the desired inlet conditions are achieved, controlled by solenoid valves. Once conditioned to target values, the solenoid valves open the PCM-HX loop, allowing the refrigerant to exchange heat with the PCM-HX before exiting. An in-line post heater is positioned after the PCM-HX outlet to superheat the refrigerant if it exits the PCM-HX in the two-phase region. This process enables the back-calculation of the specific enthalpy of the refrigerant at the PCM-HX outlet. The watt meter records the power input of the post heater. Finally, the refrigerant re-enters the oversized condenser to initiate the loop once again. It is worth noting that a back-pressure valve, which is installed to ensure stable system pressure in case of pressure control issues, is only used for evaporating tests, and not utilized during the condensing tests.

Images of the PCM-HX test section and a portion of the refrigerant cart are shown in Figure 90 (bottom). It is important to highlight that the PCM-HX is enclosed within a local chamber capable of regulating temperatures ranging from 30°C to 80°C. This controlled environment allows for adjustment of initial temperature conditions for the PCM-HX, a setup referred to as a “box-in-box” configuration. The primary function of the local chamber is to pre-melt the PCM for conducting an evaporator test. Thus, for the condenser test, the local chamber is simply utilized to provide a stable environment where temperature fluctuations were minimized compared to the outside room temperature.

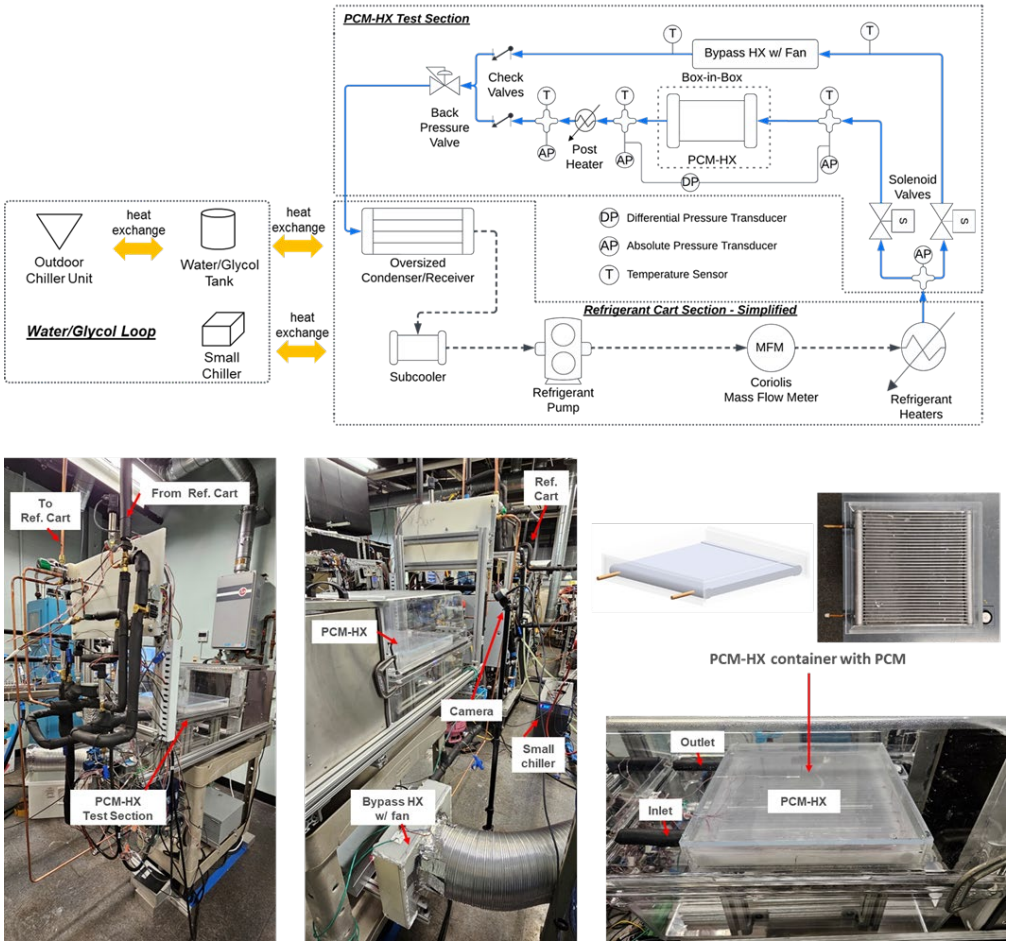

Figure 90: PCM-to-Refrigerant Experimental Setup.

Summary of PCM-HX Experimental Work

Table 43 summarizes the PCM-HX experimental work, where 10 total tests were conducted using 9 PCM-HX prototypes; 9 tests used deionized water as HTF, while 1 test used refrigerant (R410A). These tests were primarily conducted to support validation of simulation results. To ensure reliable data, each experiment included comprehensive instrumentation, and repeatability tests were performed. Energy balances between the fluid and PCM sides were also evaluated in several studies. The cases marked with (***) are discussed in detail in this report.

It is worth noting that most of the prototypes were designed to allow visual observation, although not all included this feature. For fabrication, a combination of techniques such as 3D printing, laser cutting, water jetting, and use of a brazing furnace were applied to produce research-specific heat exchanger configurations and enclosures. Figure 91 presents images from several of the PCM-HX tests conducted.

Table 43. Summary of PCM-HX Experimental Work

PCM-HX List	Orientation	Ref.
Straight annular tube	Vertical	IIR 2021

		[189]
Helix tube	Vertical	Internal Study (A)
Annular finned-tube***	Vertical	Herrick 2022 [190]
Annular finned-tube with copper sponge***	Vertical	Internal Study (B)-
Serpentine flat tube	Horizontal	HPC 2023 [191]
Serpentine flat tube	Vertical	Internal Study (C)
Optimized annular finned-tube with resistance capacitance model (RCM) approach***	Vertical	Herrick 2024 [192]
Refrigerant-to-PCM experiment prototype with microchannel HX***	Horizontal	Herrick 2024 [193]
Topology optimized prototypes from literature [172] (baseline and melting topology-optimized units)***	Horizontal	Internal Study (D)

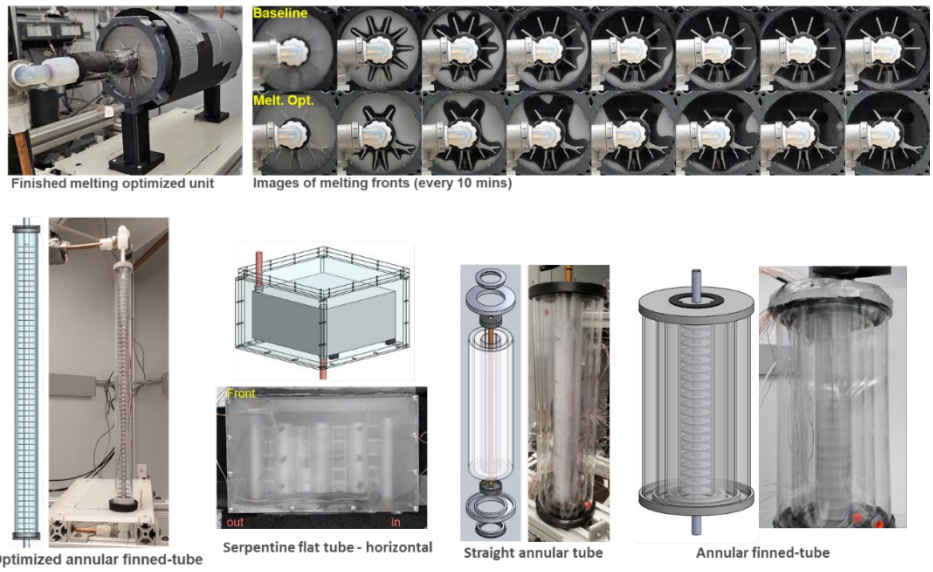

Figure 91: Selected images of tested PCM-HX TES units

3D-Printed Annular-Fin Tube PCM-HX Testing

The 3D printed annular-fin tube PCM-HX (Table 37, Figure 70) was tested with water as the HTF. In total, calibrated 78 T-type thermocouples were installed in pairs the test section: 30 inside the container to capture PCM temperature and 48 for calculating the heat loss to the ambient and thermal mass of the container (Figure 92). All yellow thermocouples follow the top right image in Figure 92 with an average human error deviation of ±0.6 mm from the designed positions, while the green thermocouple pairs were located at the tube wall and end tip of the fin. The blue thermocouple pair was installed at the bottom container cover, and the red thermocouple pair was installed in the top compartment. Figure 93 shows the positions of the 14 thermocouple pairs that were installed to estimate the heat loss and the thermal mass of the test setup.

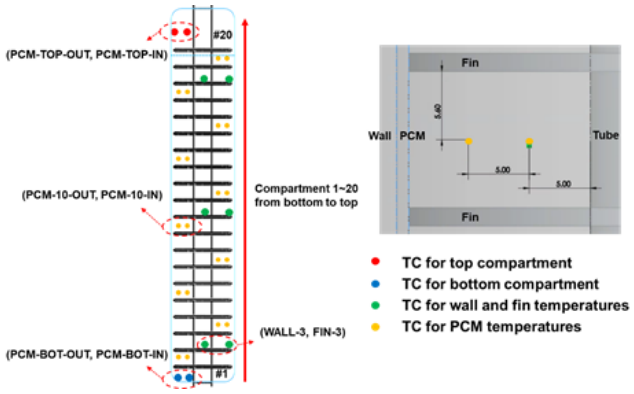

Figure 92: PCM side thermocouple positions [mm] and naming convention.

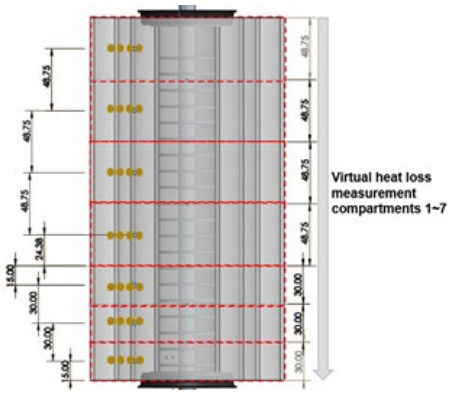

Figure 93: Insulation cylinder side thermocouple positions [mm].

Six tests (Table 44) were conducted using deionized water as the HTF. Two main groups were formed based on the HTF direction (vertical up vs. vertical down). Then, the melting inlet HTF temperature was varied incrementally to create additional test conditions.

Table 44: Summary of test conditions.

Test	Flow Direction	MFR [g/s]	Ambient T [°C]	Avg. Inlet T HTF [°C] (M/S)	Avg. Initial PCM T [°C] (M/S)	Test Duration [min] (M/S)
1	Up	2.5	25.1	44.0 / 27.3	25.3 / 41.6	38.2 / 90.2
2			25.2	48.5 / 27.7	25.5 / 44.8	26.5 / 92.7
3			25.1	52.6 / 27.9	25.3 / 47.6	19.8 / 94.3
4	Down		25.1	44.0 / 27.5	25.3 / 41.8	42.0 / 84.3
5			25.1	48.3 / 27.8	25.4 / 45.1	28.3 / 88.0
6			25.1	52.6 / 28.1	25.5 / 48.2	21.0 / 90.2
M = Melting, S = Solidification						

Test condition 2 (Table 44) was repeated three times to verify the reliability of the test results. As shown in Figure 94(a), the ambient temperature for all three tests were ~25.15°C. Furthermore, the ΔT between the PCM-HX inlet and outlet and HTF inlet temperature during the repeatability tests are shown in Figure 94(b) and (c), where the red dotted lines highlight melting operation and blue dotted lines highlight the solidification operation. The melting / solidification were considered complete once all the PCM

thermocouples in the container reached the liquidus / solidus temperatures (Table 44). Additionally, the onset of PCM solidification is when the ΔT between the PCM-HX inlet and outlet from Figure 94(b) became negative. The average temperature of all PCM thermocouples inside the container is shown in Figure 94(d), where it is clear that the average PCM temperature profiles had almost negligible deviations across each test, confirming the repeatability of the test facility with the finned-tube PCM-HX setup.

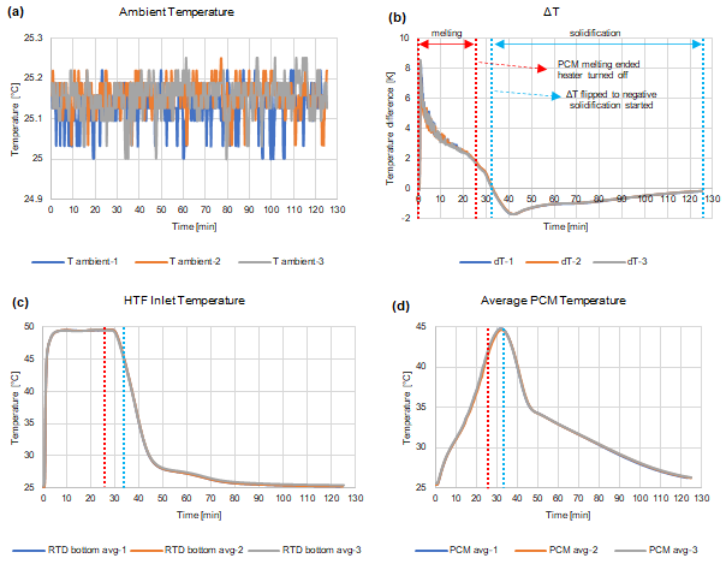

Figure 94: Repeated plots of test condition 2: (a) ambient temperature, (b) ΔT, (c) HTF inlet temperature, and (d) average PCM temperature.

Next, consider the impact of flow direction, by examining the temperature readings from the outer yellow thermocouples installed on the left side of the container (Figure 95(a)) for both upward and downward HTF flow. As expected, the PCM temperature profile follows the HTF flow direction. However, the main mode of heat transfer during the solidification process is conduction, and thus the temperature differences among the selected thermocouples were relatively smaller compared to the melting process.

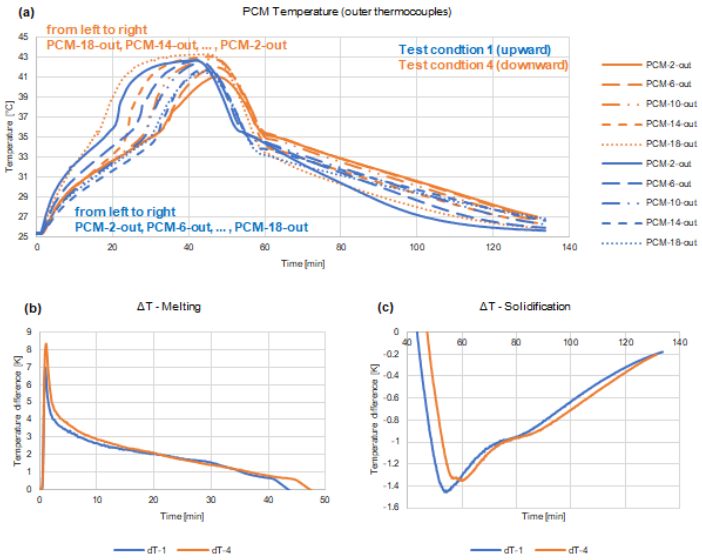

Figure 95: Test conditions 1 and 4 comparison plots: (a) selected PCM temperature profiles, (b) ΔT during melting, and (c) ΔT during solidification.

A summary of the energy balance results for each test condition's melting [M] and solidification [S] process is presented in Table 45, all well within ±10%. For both HTF directions, the energy balance deviation was decreased as the inlet temperature of the HTF increased for both phase change processes.

Table 45. Summary of energy balance estimation

Test	Theoretical Storage [kJ]	Q_{water} [kJ]	Thermal Mass [kJ]	Heat Loss [kJ]	Charged / Discharged Energy [kJ]	Deviation [%]
1	46.6 [M], 46.7 [S]	51.9 [M], 42.8 [S]	8.1 [M], 8.4 [S]	9.1 [S]	43.8 [M], 43.5 [S]	5.9 [M], 6.7 [S]
2	47.6 [M], 48.5 [S]	53.4 [M], 46.1 [S]	8.4 [M], 9.9 [S]	10.1 [S]	45.1 [M], 46.3 [S]	5.2 [M], 4.6 [S]
3	47.9 [M], 50.2 [S]	56.2 [M], 49.4 [S]	8.5 [M], 11.3 [S]	10.8 [S]	47.7 [M], 48.9 [S]	0.5 [M], 2.6 [S]
4	47.0 [M], 46.7 [S]	57.0 [M], 41.1 [S]	9.0 [M], 8.7 [S]	10.1 [S]	48.0 [M], 42.5 [S]	-2.0 [M], 9.0 [S]
5	48.3 [M], 48.8 [S]	58.4 [M], 44.4 [S]	9.4 [M], 10.4 [S]	11.1 [S]	49.0 [M], 45.1 [S]	-1.4 [M], 7.5 [S]
6	49.3 [M], 50.6 [S]	59.5 [M], 47.1 [S]	9.6 [M], 11.9 [S]	11.9 [S]	49.9 [M], 47.2 [S]	-1.2 [M], 6.8 [S]
M = Melting, S = Solidification						

Copper Sponge Finned-Tube PCM-HX Testing

The copper sponge finned-tube PCM-HX (Table 39, Figure 72) setup was the same as the 3D-Printed annular-fin tube PCM-HX described above, including the use of deionized water as the HTF. The only change is the addition of copper sponge into the PCM matrix. The test conditions are summarized in Table 46.

When comparing the no-sponge and with-copper-sponge PCM-HXs (Table 44 vs. Table 46, respectively), it is clear that the addition of copper sponge to the PCM-HX did not

have a significant effect on the melting test duration. However, the copper sponge PCM-HX solidified 4% to 11.1% faster compared with the no-sponge PCM-HX. This is because the copper foam increases the PCM thermal conductivity, reducing the PCM thermal resistance. This is especially important for the solidification case, where conduction is the dominant heat transfer mode.

Table 46. Summary of test conditions – Copper Sponge Fin-Tube PCM-HX

Test	Flow Direction	MFR [g/s]	Ambient T [°C]	Avg. Inlet T HTF [°C] (M/S)	Avg. Initial PCM T [°C] (M/S)	Test Duration [min] (M/S)
1	Up	2.5	25.2	44.0 / 27.8	25.3 / 42.0	38.3 / 80.7
2			25.2	48.5 / 28.1	25.3 / 45.3	27.7 / 84.3
3			25.2	52.6 / 28.4	25.3 / 48.1	19.5 / 83.8
4	Down		25.2	44.1 / 28.0	25.4 / 42.0	41.3 / 81.0
5			25.1	48.5 / 28.4	25.4 / 45.4	26.7 / 83.3
6			25.1	52.7 / 28.6	25.4 / 48.6	19.5 / 82.5
M = Melting, S = Solidification						

A comparison of the no-sponge and copper sponge PCM-HX performance for both the upward and downward HTF directions was also conducted (Figure 96). Interestingly, the copper sponge PCM-HX melting and solidification durations are approximately constant regardless of flow direction. This is a deviation from the melting result for the no-sponge PCM-HX, where it is likely that the copper foam is inhibiting natural convection effects which would speed up melting for the no-sponge upward flow case. This impact is not expected during solidification, where conduction heat transfer is dominant.

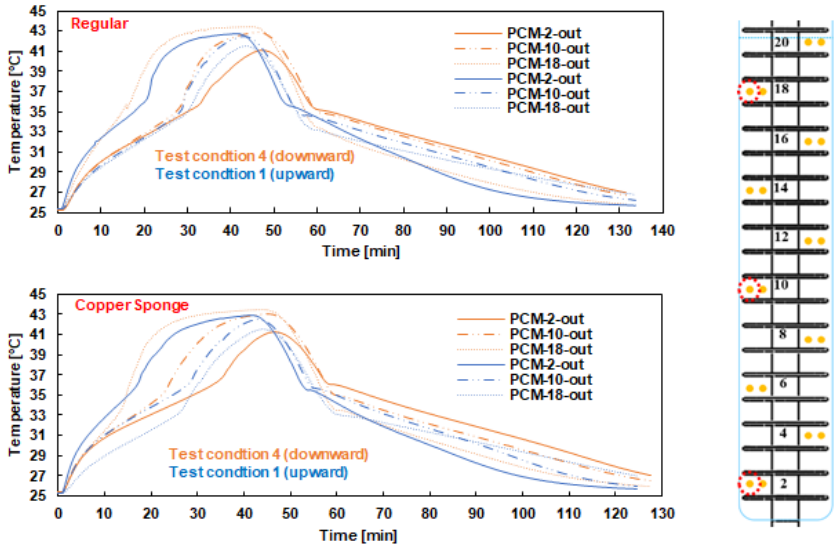

Figure 96: Test conditions 1 and 4 comparison plots for selected PCM temperature profiles: (top) regular finned-tube setup and (bottom) copper sponge finned-tube setup.

Finally, a summary of the energy balance results for each test condition's melting [M] and solidification [S] process is presented in Table 47, with all test conditions having energy

balances within ±6% deviation.

Table 47. Energy balance estimation for the copper sponge finned-tube setup

Test	Q_{HTF} [kJ]	Q_{HTF} Uncertainty [±%]	Theoretical Storage [kJ]	Estimated Charged / Discharged Energy [kJ]	Deviation [%]
1	55.0 [M], 42.8 [S]	1.1 [M], 2.9 [S]	49.1 [M], 49.1 [S]	47.2 [M], 46.7 [S]	3.9 [M], 5.0 [S]
2	56.6 [M], 46.2 [S]	0.8 [M], 2.8 [S]	50.6 [M], 51.6 [S]	49.2 [M], 50.1 [S]	2.6 [M], 3.0 [S]
3	57.8 [M], 48.7 [S]	0.5 [M], 2.6 [S]	51.2 [M], 53.7 [S]	50.7 [M], 52.6 [S]	0.9 [M], 2.1 [S]
4	58.8 [M], 44.0 [S]	1.1 [M], 2.8 [S]	49.7 [M], 49.3 [S]	49.2 [M], 47.3 [S]	1.2 [M], 4.0 [S]
5	59.7 [M], 47.1 [S]	0.7 [M], 2.7 [S]	51.4 [M], 51.8 [S]	51.4 [M], 50.6 [S]	-0.1 [M], 2.3 [S]
6	61.4 [M], 50.9 [S]	0.5 [M], 2.5 [S]	52.5 [M], 54.2 [S]	53.6 [M], 54.5 [S]	-2.1 [M], -0.5 [S]
M = Melting, S = Solidification					

Serpentine Tube PCM-HX Testing: Horizontal

The serpentine tube PCM-HX (Table 41, Figure 81) was configured with 78 pre-calibrated T-type thermocouples with ±0.5 K absolute uncertainty as shown in Figure 97. After calibration, the measured maximum temperature deviation across all thermocouples was observed to be about 0.15 K.

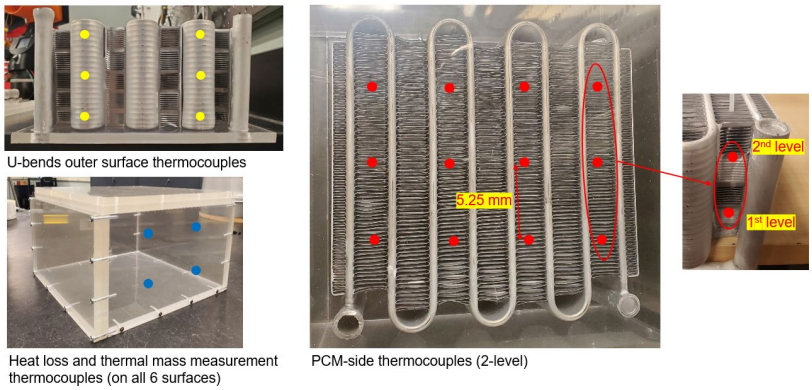

Figure 97: Thermocouple distributions.

The test matrix (Table 48) was designed to test a combination of two melting inlet temperatures and three mass flow rate using deionized water as the HTF. The ambient temperature for all test conditions was controlled as ±25.1°C. The solidification cases had lower Reynolds number (for the same inlet mass flow rate) due to differences in water thermophysical properties. The test durations and average charge and discharge rates are also shown, where it is clear that higher mass flow rates yielded both faster melting / solidification due to higher average charge and discharge rates.

Table 48: Summary of test conditions

Test	MFR [g/s]	Re (1 channel)	Avg. Inlet T [°C]	Initial Avg. PCM T [°C]	Test Duration [hr]	Avg. Charge / Discharge Rate [W]
1	5	143.7 [M], 78.7 [S]	59.0 [M], 26.3 [S]	25.2 [M], 56.7 [S]	1.3 [M], 4.8 [S]	259.8 [M], 61.3 [S]
2	10	287.3 [M], 156.0 [S]	59.0 [M], 25.9 [S]	25.1 [M], 56.3 [S]	1.1 [M], 4.1 [S]	298.7 [M], 70.0 [S]
3	15	431.0 [M], 232.9 [S]	59.0 [M], 25.7 [S]	25.1 [M], 56.6 [S]	1.0 [M], 3.9 [S]	312.3 [M], 73.3 [S]
M = Melting, S = Solidification						

In Figure 98, the temperature at multiple thermocouple locations in the PCM during Test #2 (melting) are displayed. Traveling along the fluid flow path, from thermocouple location #1 near the inlet to thermocouple location #10 near the outlet, the temperature stratification across the HX clearly follows the serpentine fluid path. For the multiple thermocouples installed in the PCM domain at the same flow-path location (but at different depths), it is clear that the "top" temperatures were generally higher, likely due to the effect of natural convection.

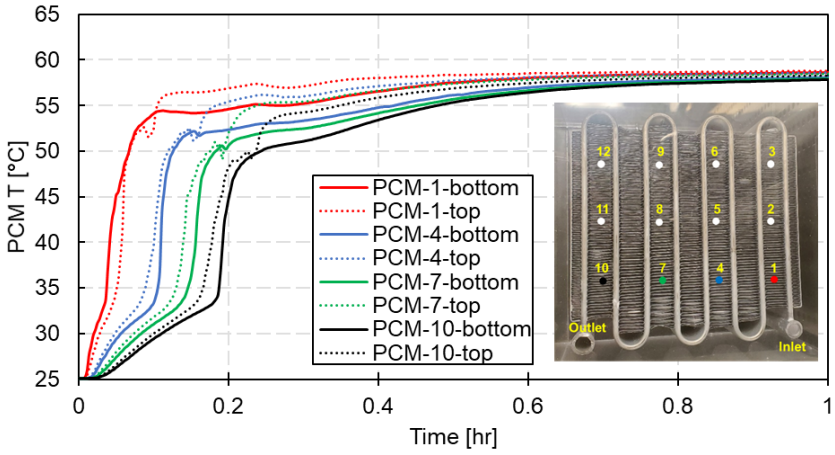

Figure 98: Test #2 temperature profiles at selected PCM locations – melting.

Similarly, the Test #2 solidification temperature profiles are presented in Figure 99. As mentioned previously, conduction is the dominant heat transfer mode during solidification, so the temperature gaps between the top and bottom thermocouples are relatively smaller compared to the melting case. Lastly, a small supercooling phenomenon was observed near 31°C for all PCM locations.

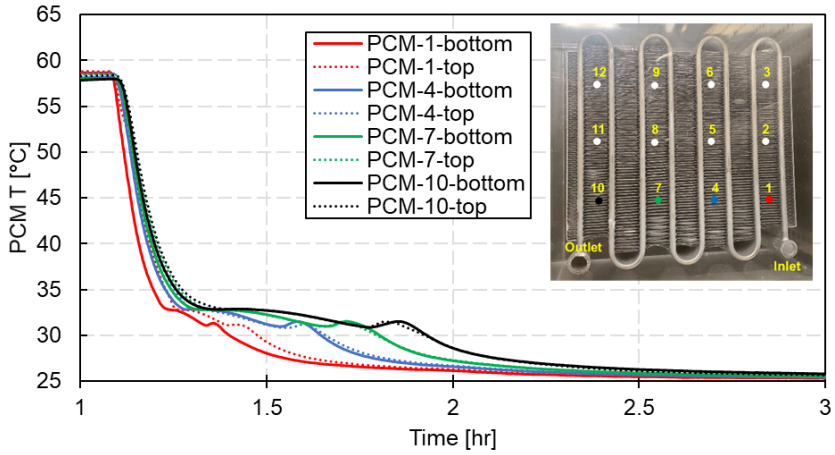

Figure 99: Test #2 temperature profiles at selected PCM locations – solidification.

In Figure 100, the U-bend surface temperature profiles from Test #2 are presented. It was evident that the temperature measurements in all three levels were very close at the beginning of the melting process. However, as the PCM melted around outer tubes along the flow path, temperature stratification begins to occur due to natural convection, which impacts the HTF temperature. Unsurprisingly, such temperature gaps did not occur during the solidification process.

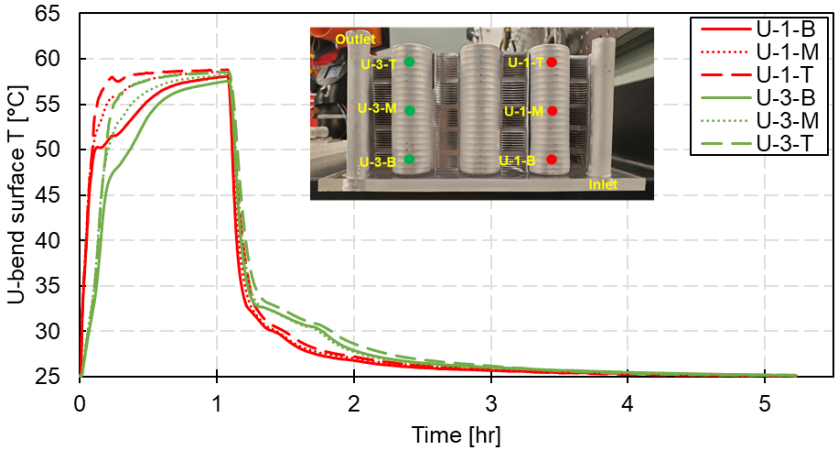

Figure 100: Test #2 temperature profiles at selected U-Bend locations.

Serpentine Tube PCM-HX Testing: Vertical

The serpentine tube PCM-HX was then installed so the fluid flow path started at the top of the PCM-HX and exited at the bottom of the PCM-HX (Figure 101). The PCM was RT35 and the same amount of PCM mass (3,979 g) was added to the container as for horizontal tests. The setup was completely insulated during the tests.

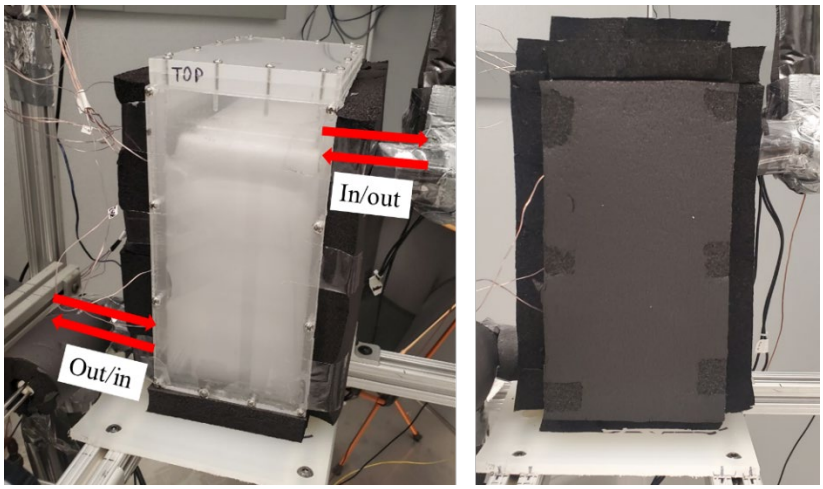

Figure 101: Vertical test setup configuration.

The test matrix for the vertically oriented serpentine tube PCM-HX is described in Table 49. Three different mass flow rates (MFR) were tested with both upward and downward HTF directions. The ambient temperature was controlled to be around 25.0~25.1°C during the tests. When the melting was completed, the heater was turned off and the heat exchanger with a fan cooled down the HTF temperature for solidification processes.

Table 49: Test matrix

HTF Direction	Test	MFR [g/s]	Avg. Inlet T [°C]	Test Durations [min]	Total Charge/Discharge (Q_{water}) [kJ]	Avg. Charge/Discharge Rate [W]
Upward	1	5	59.0 [M], 26.4 [S]	91.5 [M], 248.5 [S]	1029.6 / 923.1	188.1 / 61.9
	2	10	59.0 [M], 25.9 [S]	84.2 [M], 234.3 [S]	1004.8 / 909.2	199.4 / 64.6
	3	15	59.0 [M], 25.8 [S]	76.3 [M], 215.7 [S]	980.2 / 904.9	214.0 / 69.9
Downward	4	5	59.0 [M], 26.4 [S]	98.5 [M], 267.5 [S]	1064.9 / 939.5	180.5 / 58.5
	5	10	59.0 [M], 26.0 [S]	85.5 [M], 235.7 [S]	1017.9 / 917.6	198.8 / 64.9
	6	15	59.0 [M], 25.8 [S]	81.2 [M], 234.0 [S]	1004.1 / 912.9	206.2 / 65.0
M = Melting, S = Solidification						

A comparison of horizontal and vertical fluid flow is summarized in Table 50. Unsurprisingly, increasing mass flow rate resulted in faster melting and solidification and higher charge / discharge rates. However, more interesting results are seen when examining the impact of changing HTF flow direction. As with the annular fin-tube PCM-HX, upward flow tests yielded faster test duration, while the solidification results did not follow the same trend, i.e., upward flow solidification was always faster than downward flow solidification.

Table 50: Test results comparison: Horizontal vs. Vertical Fluid Flow

MFR changing, HTF inlet T fixed						HTF direction changing, MFR fixed					
MFR Change [g/s]	Test	Melt. Time	Sol. Time	Avg. Charge Rate	Avg. Discharge Rate	HTF Direction	Test	Melt. Time	Sol. Duration	Avg. Charge rate	Avg. Discharge rate
5 → 10	1→2 (up)	↓8.0%	↓5.7%	↑6.0%	↑4.4%	Down → Up	**4→1**	**↓7.1%**	**↓7.1%**	**↑4.2%**	**↑5.8%**
	4→5 (down)	↓13.2%	↓11.9%	↑10.1%	↑10.9%		**5→2**	**↓1.5%**	**↓0.6%**	**↑0.3%**	**↓0.5%**
5 → 15	1→3 (up)	↓16.6%	↓13.2%	↑13.8%	↑12.9%		**6→3**	**↓6.0%**	**↓7.8%**	**↑3.8%**	**↑7.5%**
	4→6 (down)	↓17.6%	↓12.5%	↑14.2%	↑11.1%						

Further efforts were made to better understand the unintuitive solidification test results. Additional tests were conducted, with insulation removed, to visually examine the solidification front in the PCM (Figure 102). Interestingly, a clear difference between the downward and upward solidification was observed, where more PCM solidified at the top fins of the HX for the downward solidification case. This suggests that that air cavities may have been created at the lower section of the container as PCM contracts during the solidification process. Such air cavities would worsen the heat transfer and slow the solidification process. For the upward solidification process, as PCM shrinks from the bottom, allowing liquid PCM from the upper section to fill the potential air cavities.

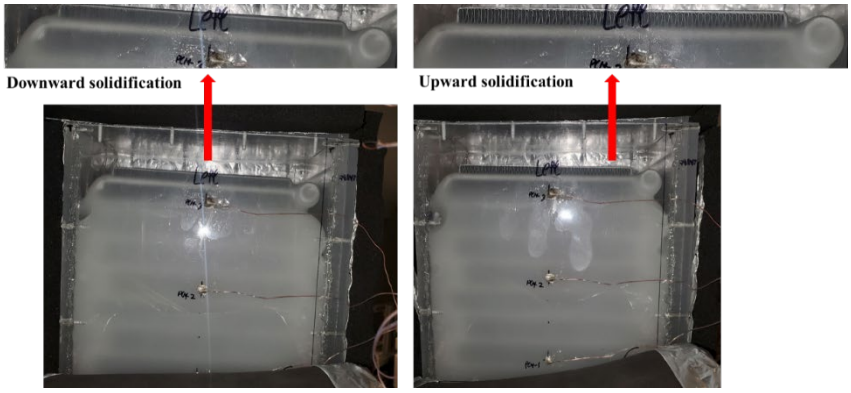

Figure 102: Side view of the PCM-HX after removing the insulation sheet

The test setup was cut into multiple sections using a bandsaw after a downward run to check whether air cavities were indeed forming inside the container (Figure 103). However, air cavities near the HX were very hard to identify because friction from the bandsaw blade melted the PCM and the residues of the aluminum fins could not be removed entirely after the cut. However, multiple air cavities were seen at the bottom surface of the container, somewhat confirming the air cavity hypothesis.

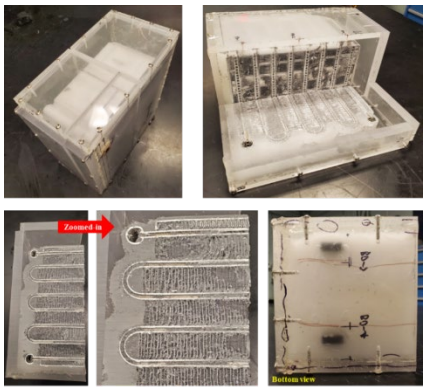

Figure 103: PCM-HX container after cut in multiple sections

Optimized Annular Finned-Tube PCM-HX Testing

The optimized annular finned-tube PCM-HX (Table 40, Figure 76) was tested with water as the HTF. Figure 104-(L) depicts the positions of the installed thermocouple. All temperature sensors were calibrated with highly accurate reference RTDs and a thermal bath. In total, 17 thermocouples were installed in and around the PCM-HX. On the PCM side, three thermocouples were installed between the HX fins using the 3D-printed holders. Ten thermocouples were installed on the outer surface of the container, and two pairs of two thermocouples were installed on the inner and outer sides of the container top and bottom covers. Water-side temperature measurements were recorded using two sets of three RTDs. Figure 104-(R) displays the complete setup with the PCM-HX insulated with three inches of R-13 fiberglass insulation to minimize heat loss through the container to the ambient.

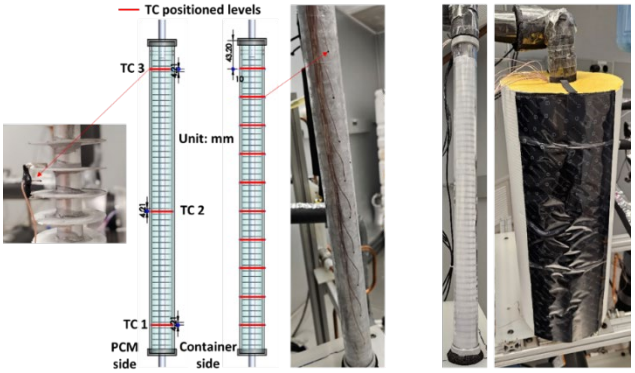

Figure 104: (Left) Installed thermocouple positions; (Right) Completed test setup with PCM & fiberglass insulation.

As described above, the as-designed total water volume flow rate of 6.4 L/min was selected. For a single PCM-HX unit, this is equivalent to a mass flow rate of ~1.5 g/s. The PCM-HX water flow direction was upward. Three repeatability tests were performed, and the temperature reading differences were negligible; thus, the detailed results are omitted for brevity. It is noteworthy that the tube-side pressure drop was not experimentally measured, as the primary focus during RCM validation was to assess the heat transfer

characteristics of the PCM-HX. The comparison of as-designed simulated and experimental PCM-HX performance is summarized in Table 51.

Table 51: Test condition and results with 1.5 g/s mass flow rate.

	Hot Water Supply Time	Discharge Power until Cutoff T
Experimental PCM-HX	23.5 min	45.5 W (±0.4% average uncertainty)
Simulated (as-designed) PCM-HX (Percent error w.r.t. experiment)	20.3 min (-13.6%)(-13.6%)	39.9 W (-12.3%)(-12.3%)

In Figure 105, the “hot water supply time” indicates the total time until the outlet water temperature reaches the cutoff temperature (51.7°C); the average inlet water temperature was ~46.7°C. Meanwhile, “discharge power” indicates the heat transfer rate during the hot water supply period as the pre-melted PCM solidifies. While the original simulation results indicated a hot water supply time of 24.4 minutes, the supply time reported here is 20.3 minutes. Ultimately, the RCM underpredicted the experimental hot water supply time and discharge power by 13.6% and 12.3%, respectively. These discrepancies are attributed to multiple items, i.e., minor design modifications during prototyping (see Section 6.1), the as-designed PCM-HX assuming a constant inlet water temperature while the experimental inlet temperature was not constant, and additional thermal masses introduced by the container, container covers, and insulation. Another potential source of uncertainty may include the assumption of a uniform, constant PCM-HX initial temperature; i.e., the PCM-HX initial temperature is determined as the average of the three internal thermocouples, while the actual PCM-HX temperature is likely vertically-stratified rather than uniformly distributed.

The predicted and experimental hot water supply temperatures are plotted along with the reference cutoff temperature (51.7°C) in Figure 105. It was observed that the maximum deviation occurred at the beginning of the test when the temperatures were rapidly changing. During the remainder of the test, the temperature deviation remained below 2 K, with an average deviation of 1.3 K over the entire PCM discharging process, indicating a strong agreement between the experimental and RCM results.

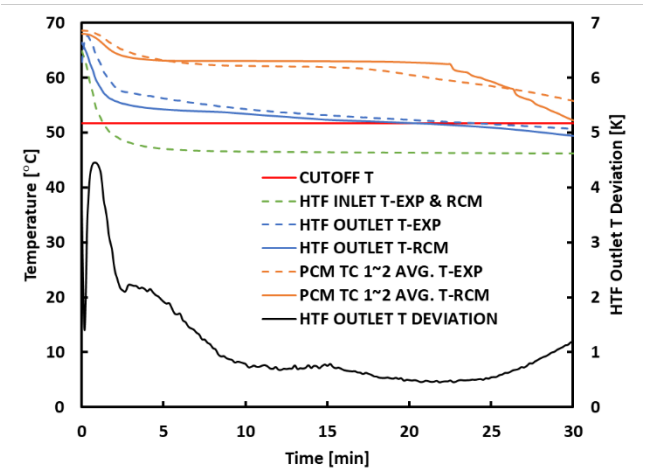

Figure 105: Comparison between experimental and RCM results during hot water drawing test (PCM solidification).

The HTF inlet temperature profile and the PCM average temperature from Thermocouples 1 and 2 are also plotted in Figure 105 for reference. Note that Thermocouple 3 (located near the top of the PCM-HX) was excluded as it became exposed to the air during PCM solidification, and thus cannot provide useful test data. The trends observed in both the experimental and simulation data for the average PCM temperature and hot water supply time were closely aligned. It is important to highlight that the hot water supply time, a critical metric in this context, consistently showed great agreement between the experimental and RCM results.

Longitudinal Fin PCM-HX Testing

The two longitudinal fin PCM-HXs (Figure 84 - Figure 86) were tested using water as HTF. The baseline unit was first prepared for experimentation, with the topology-optimized HX being prepared in a similar manner. In Figure 106(L), the PCM-side thermocouples are marked in red, and the tube surface thermocouples are marked in yellow. The final setup is shown in Figure 106(R).

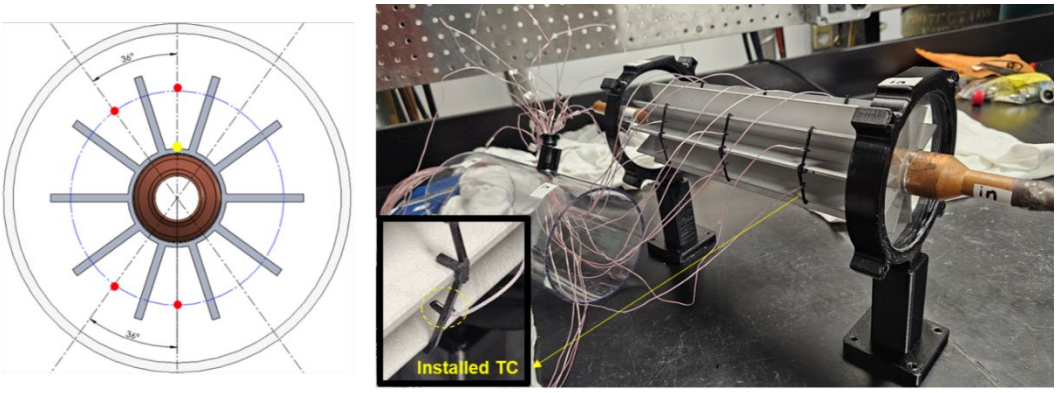

Figure 106: (Left) Thermocouple positions; (Right) Installed thermocouples.

Next, the 3D-printed covers, acrylic round plates, and impact-resistant polycarbonate container cylinder were assembled with the HX using various epoxy glues suited for each material combination. Figure 107(L) shows the curing process with an I-beam level placed on top to ensure proper assembly. In Figure 107(R), the fully charged PCM-HX container with melted PCM is shown with a recorded mass of 1.48 kg. The finished assembly was then leak-checked with water before being integrated with the test facility.

Figure 107: (Left) PCM-HX assembly; (Right) PCM charging / mass measurement

The PCM-HX assembly and test facility shakedown was conducted without insulation to (1) find potential leaks and (2) observe the PCM melting fronts. The environmental chamber ambient temperature was maintained at 25°C, and the water inlet temperature and mass flow rate were set at 55°C and 30 g/s, respectively. Figure 108 shows photos taken during the melting shakedown test. Considerable effort was made to maintain the PCM-HX symmetry, which can be seen in the symmetry of the melting front during the test.

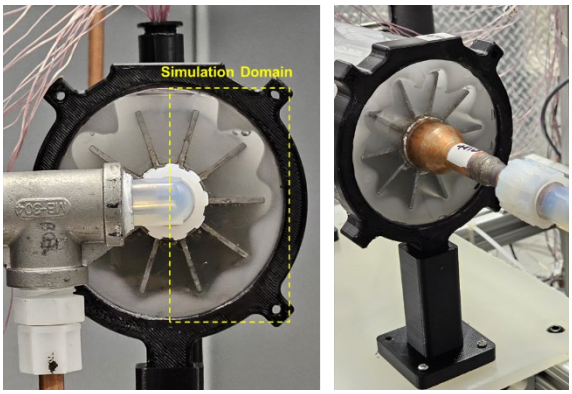

Figure 108: Obtained images from the melting shakedown test

Figure 109 shows the melting-optimized unit, with insulation, ready for testing. The inlet-side cover was left uninsulated for capturing images of the PCM phase change process during the experiments.

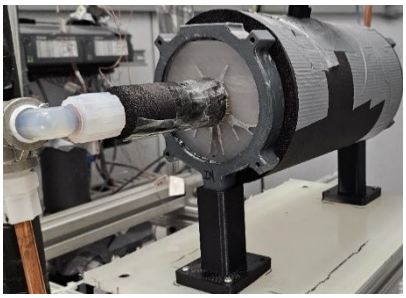

Figure 109: Finished melting-optimized PCM-HX

RT35 PCM (nominal melting temperature = 35°C) was used with 1.47 kg and 1.48 kg charged for the baseline and melting-optimized units, respectively. For the main reference point test condition, a water inlet temperature of 55°C, with ambient and initial PCM temperatures of ~25°C, were used (Figure 110(L)). The water mass flow rate was fixed at 30 g/s. In Figure 110(M), the measured PCM-HX waterside heat rates and accumulated energies are shown. The baseline unit initially shows a higher heat rate due to the uniform fin distribution aiding conduction during the early stages of melting. However, the optimized unit heat rate surpasses the baseline at around the 30-minute mark, as natural convection effects becomes more dominant within the container as more PCM melts.

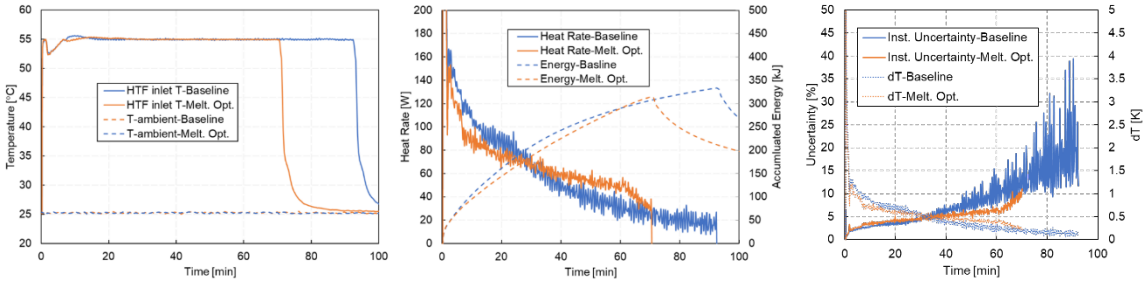

Figure 110: (Left) Water inlet and ambient temperatures; (Middle) Measured water-side heat rates and accumulated energies; (Right) Instantaneous systematic uncertainty for heat rate and temperature difference

It is important to note that due to varying heat loss rates over time between the two units, and increasing uncertainties as the temperature difference between the water inlet and outlet decreased, there was a notable discrepancy in accumulated energy values when the melting tests were terminated. As the temperature difference approaches the RTD measurement error, the uncertainties increase (Figure 110(R)).

Figure 111 presents 10-minute time-lapse images taken during the melting tests, which further support that the baseline unit initially performs better (i.e., melts faster) when conduction is the primary mode of heat transfer. However, as natural convection becomes more dominant, the melting-optimized unit melts faster and surpasses the baseline. The difference between the last two images (60-minute elapsed vs. 70-minutes elapsed), it is clear that melting-optimized unit completed melting faster than the baseline unit.

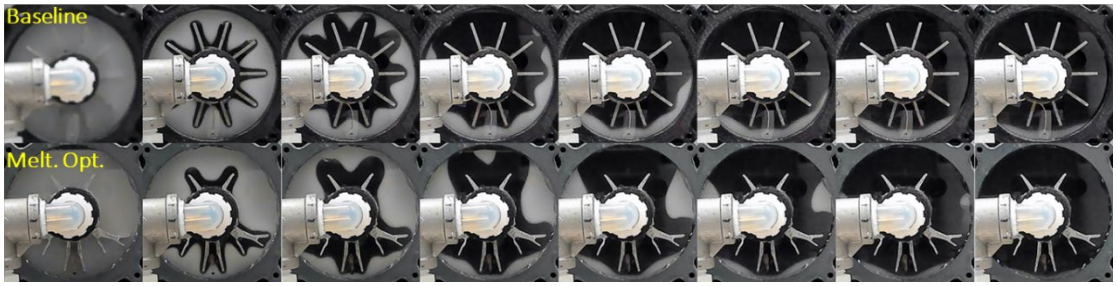

Figure 111: Images of melting fronts every 10 minutes

Microchannel PCM-HX Two-Phase Refrigerant-to-PCM Testing

The PCM selected for the experiment was RT35 [173]. Table 52 displays the manufacturer's property data. The measured mass of the embedded PCM within the container was recorded as 2.6 kg.

Table 52. RT35 thermophysical properties [173]

Nominal Phase Change Temperature [°C]	35
Density [kg/m^3]	860 [solid], 770 [liquid]
Thermal Conductivity [W/m-K]	0.2 [solid], 0.2 [liquid]
Specific Heat [kJ/kg-K]	2 [solid], 2 [liquid]
Heat Storage Capacity [kJ/kg] (Sensible + Latent Heat, 26°C – 41°C)	160 (with ±7.5% accuracy)

The PCM-HX details are illustrated in Figure 112. A commercially-available aluminum MCHX with louvered fins (349 mm x 332 mm, W x H) was selected, and its refrigerant flow path is depicted in Figure 112(L). Thermocouples were installed on both the header side (yellow) and tube side (red), as shown in Figure 112(M). Thin T-type thermocouples were used, and silver epoxy was applied to permanently attach them to the HX surfaces. Figure 112(R) provides a side view of the outlet-side corner, highlighting the locations of thermocouples used to determine the end of PCM melting. Two thermocouples were strategically placed at the bottom side of the outlet corner, as this area was anticipated to be the last portion inside the container to undergo melting. These thermocouples serve to indicate the completion of the PCM full melting process by monitoring their temperatures. The outer container, constructed from acrylic plates, features approximately 5 mm gaps between the HX and the inner walls. This design facilitates more convenient simulation validation in the future, ensuring uniform physical boundaries.

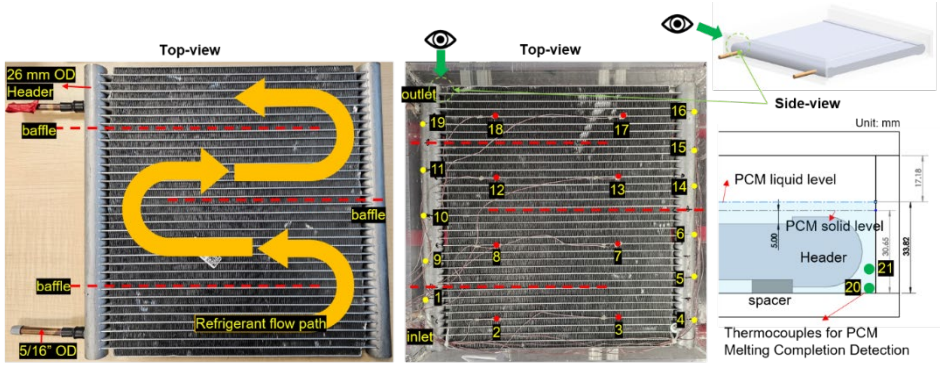

Figure 112: (Left) HX configuration; (Middle) Installed thermocouple locations; (Right) Side view of container with melting completion determining thermocouple locations.

Table 53 summarizes the test conditions conducted in this study. “Initial T” represents the average initial temperatures from the installed thermocouples inside the PCM-HX, which correspond to the ambient temperature. “Avg. Inlet T” and “Avg. Inlet P” denote the average temperature and pressure values of the refrigerant inlet conditions until the PCM inside the container is fully melted. “Avg. Inlet Condensing T” represents the average saturated liquid temperature value based on the measured pressure values at the PCM-HX inlet. The inlet condition of R-410A into the PCM-HX was adjusted to simulate the compressor discharge for a typical residential air-conditioning application.

Table 53. Test conditions under different mass flow rates.

MFR [g/s]	Initial T [°C]	Avg. Inlet T [°C]	Avg. Inlet P [kPa]	Avg. Inlet Condensing T [°C]
3.5	24.6	59.6	2907.7	47.6
4	25.3	59.9	2922.1	47.9
4.5	24.9	60.2	2934.6	48.0
5	25.3	60.1	2936.6	48.1
5.5	25.6	60.6	2949.4	48.3
6	25.0	60.5	2959.7	48.4
8	24.3	60.4	2986.8	48.9

Figure 113(L) shows a plot of the measured power and accumulated energy from R-410A during the condensing tests. A higher mass flow rate corresponded to a higher power and caused the refrigerant more quickly transitioning to the two-phase region. This was

evidenced by the significant decrease in power following the initial stable power supply pattern. Consequently, the slope of the accumulated energy became shallower as the power decreased, reflecting the outlet being two-phase R-410A. It should be noted that the staircase-like patterns correspond to times when the post heater was manually controlled to superheat the refrigerant. This resulted in a back-calculation of the refrigerant outlet condition. In simpler terms, when the power input from the post heater was reduced, the back-calculation occurred instantaneously, while the temperature change at the post heater outlet lagged behind due to the thermal mass of the heater.

Figure 113(R) illustrates the measured inlet, measured outlet, and computed outlet condensing temperature of the refrigerant from the PCM-HX. Notably, the 3.5 g/s test condition exhibits abnormal inlet temperature fluctuations during the first 15 minutes of the test, which was suspected to be caused by insufficient refrigerant flow to properly contact the thermocouple probe in the cross-fitting. By examining the outlet temperature and condensing temperature, we can observe the timing of the refrigerant entering the two-phase region as discussed above for Figure 113(L). Moreover, the higher mass flow rate tests showed the outlet temperature exceeding the condensing temperature, i.e., superheated outlet refrigerant before 30 minutes. A slight bump in condensing temperature was observed as the outlet temperature approached the condensing temperatures, likely due to the increasing temperature of the refrigerant entering the oversized condenser increasing, eventually surpassing the water/glycol tank temperature, and thereby slightly elevating the refrigerant pressure inside the oversized condenser. This minor issue can be addressed in the future by installing an additional subcooler before the oversized condenser to cool the refrigerant before entering.

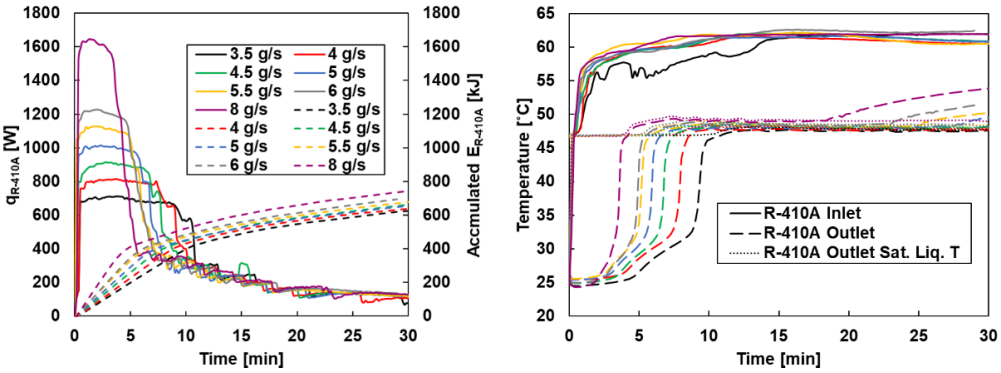

Figure 113: (Left) Measured power and accumulated energy from R-410A; (Right) Measured R-410A inlet, outlet, and outlet condensing temperatures

Figure 114(L) shows the comparison between the time taken for R-410A to reach the two-phase condition and the time required for full PCM melting inside the container. A significant discrepancy between these two values is evident, indicating that portions of the PCM volume were not fully utilized before the R-410A outlet entered the two-phase region. This discrepancy is likely attributed to the PCM volume located in the gap area between the HX surfaces and the container inner wall. This gap volume, which was not in the vicinity of the HX surfaces, accounted for approximately 27% of the total PCM volume embedded inside the container. Therefore, minimizing this gap volume is crucial in practical applications to maximize PCM utilization within a short period.

Figure 114(R) presents the recorded temperatures from selected thermocouples on the PCM-HX surface during the 4 g/s mass flow rate test. The temperatures from both the bank and tube side indicated a gradual increase along the MCHX fluid flow path. Notably, TC10 and TC19 exhibited a rapid temperature increase at the beginning, possibly attributed to heat transfer along the headers from neighboring banks.

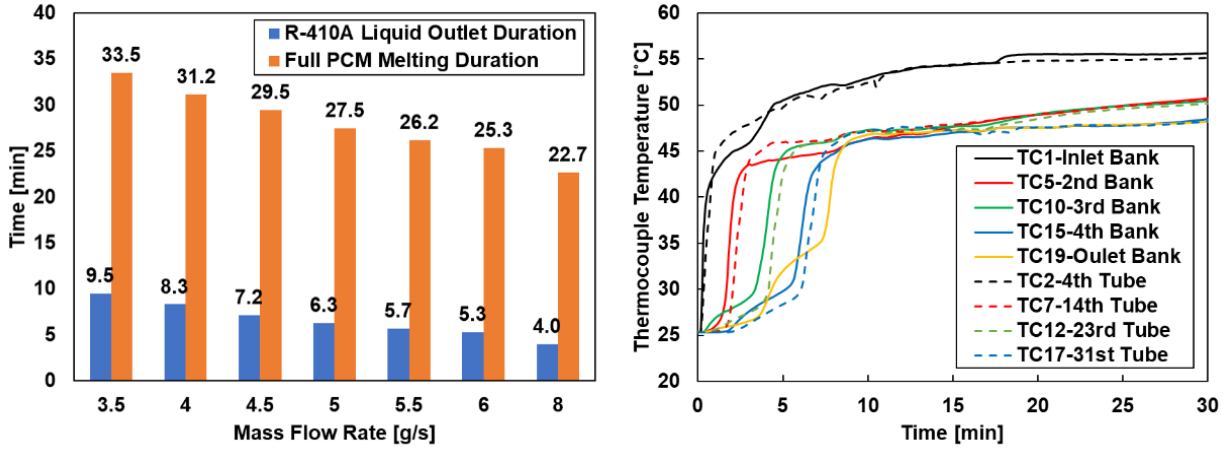

Figure 114: (Left) Test duration up to R-410A subcooled liquid outlet condition only and up to full PCM melting; (Right) Temperature plots of the selected thermocouples on the PCM-HX surfaces from the 4 g/s test.

Figure 115 shows a time-lapse of the PCM melting process as captured by the camera setup during the 4 g/s mass flow rate test. The melting progression was observed to follow the MCHX refrigerant flow path. Additionally, it was clearly that the PCM located away from the HX surface melted last. The recorded thermocouple temperatures and images of the PCM-HX melting process can serve as valuable validation datasets for future simulations of PCM-HX melting with two-phase refrigerant flow.

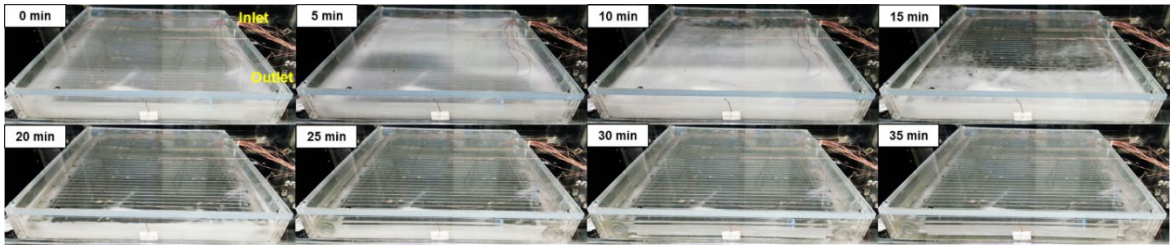

Figure 115: Visual observation of the PCM-HX from the 4 g/s test.

To further assess the PCM-HX performance, we utilize an approach outlined by [194] to generate rate capability curves and Ragone plots. In Figure 116-(L), the rate capability curves between SOC and the refrigerant outlet temperature are depicted. Here, the cutoff temperature line is arbitrarily set as the near-condensing temperature of the refrigerant to illustrate the concept of rate capability curves. The cutoff temperature of the thermal energy storage (TES) is generally application specific and is defined to gauge the extent of useful energy utilization (i.e. higher cutoff temperatures for heating applications and lower cutoff temperatures for cooling applications). In this study, the PCM-HX was fabricated for a general performance assessment, and thus the cutoff temperature was chosen as the near-condensing temperature of the refrigerant, as this corresponds to the

time when the majority of the PCM state of charge is depleted. Typically, the plot becomes more informative when curves of significantly different shapes are observed, indicating varying performance across different mass flow rates reaching the cutoff lines in distinct ways. However, with the available data covering mass flow rates ranging from 3.5 g/s to 8 g/s, the curves do not exhibit significant differences in this context. This suggests that the PCM-HX capacity is too large for the selected mass flow rates to yield meaningful distinctions among the data points. However, it is worth noting that tests with higher mass flow rates beyond 8 g/s were not feasible with the current experimental setup due to limitations in the post heater capacity.

With the same principle in mind, Figure 116-(R) illustrates the rate capability curves plotted against SOC and time. In this scenario, if an application specifies a cutoff time, one can discern which test condition proves most effective for the given time frame. It is important to note that the times at which the maximum capacity of the PCM-HX is reached (0% SOC) differ significantly from the durations required for complete PCM melting (Figure 116(L)), which seems counterintuitive. This disparity arises because the accumulated energy measured from R-410A includes the thermal mass of the acrylic plates and heat loss to the surroundings, while the estimated maximum capacity of the PCM-HX considers only the PCM capacity and the MCHX thermal mass. This discrepancy could be addressed in the future by measuring the thermal mass of the container and implementing robust insulation.

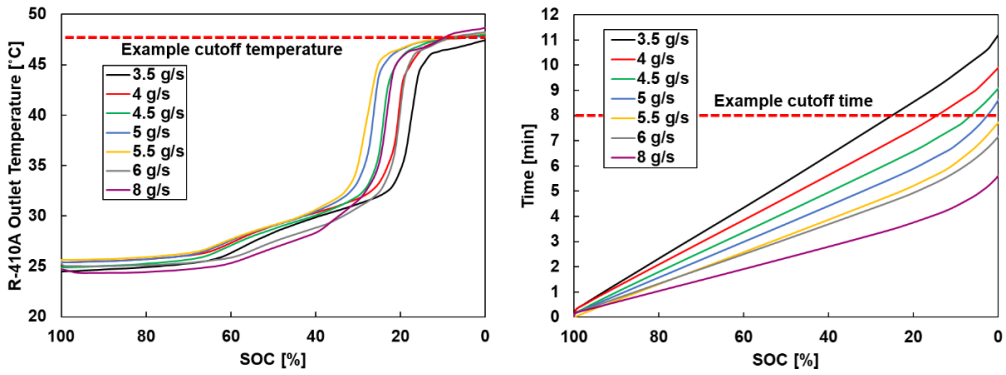

Figure 116: Rate capability plots: (Left) SOC vs. R-410A outlet temperature; (Right) SOC vs. time.

Figure 117 presents the Ragone plots, which illustrate the PCM-HX performance under various mass flow rates, considering average power and accumulated energy values only for the segment where the refrigerant outlet condition remained in the subcooled liquid region. As previously noted, the capacity of the MCHX is too large for the tested mass flow rates. Consequently, the curve ascends vertically rather than trending towards the upper left corner as mass flow rate increases, as achieving near 0% SOC is possible regardless of the mass flow rate. Ideally, to pinpoint the optimal operating condition of the PCM-HX with the most favorable balance between power and energy, a reference data point in red, as shown in Figure 117(L), is necessary. This data point demonstrates a noticeable shift towards the upper left corner compared to the nearly vertical curve observed with the low mass flow rate data points, indicating an increase in power but less utilization of energy. Therefore, the data point preceding this reference point is likely the

optimal operating condition, showcasing high power output while almost fully utilizing the PCM-HX capacity.

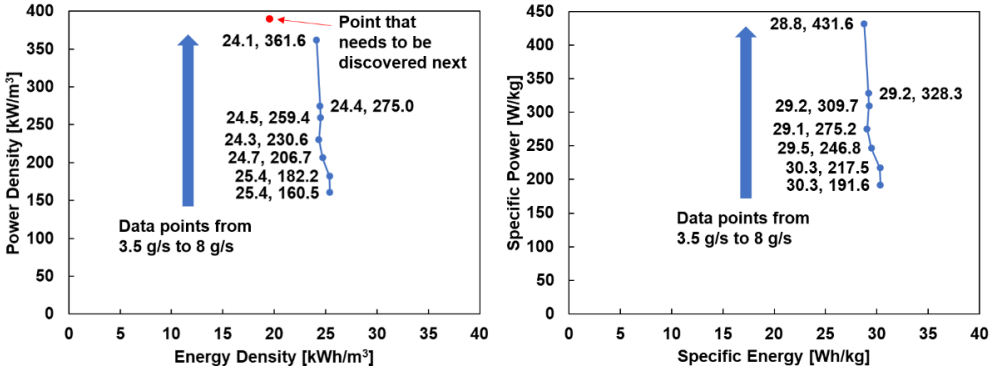

Figure 117: Ragone plots: (Left) Energy density vs. power density; (Right) Specific energy vs. specific power.

Develop Web/Desktop (UI) that incorporates the reduced order models (M1.3, M2.3; M3.2)

As part of this work, a publicly-available PCM web tool was developed which includes a PCM Database (M1.3) and a Thermal Battery Analysis Tool (M2.3, M3.2) for online PCM-HX performance simulation tool to assist the design community on common PCM-HX use-cases, e.g., single/multiple flow path(s) fluid-to-PCM and air-to-fluid-to-PCM configurations. The web tool can be found at the following link:

https://ceeeweb.umd.edu/pcmapp/

Details on the PCM Database and Thermal Battery Analysis Tool are presented in the following section.

PCM Property Database (M1.3)

A comprehensive PCM property database was developed based on commercially-available PCM data in open literature. The PCM property database is summarized in Table 54 and includes 543 total PCM products from 23 OEMs. A screenshot of the PCM Database is shown in Figure 118.

Table 54: Summary of the updated PCM database

PCM Manufacturer	Number of PCMs	Range of Melting Temps [°C]	Range of Latent Heat [kJ/kg]	Range of Energy Storage Capacity [kJ/kg]	Avg. Cost Per Mass [$/kg]	PCM Types
PCM Products Ltd	178	-74 to 885	70 to 602	-	-	organics, inorganics and eutectics
RuhrTech Co.,Ltd.	68	-50 to 100	-	124 to 390	-	organics and inorganics
Rubitherm	58	-50 to 100	-	120 to 260	12.36	organics and inorganics
Pluss	32	-30 to 89	-	140 to 350	-	organics, inorganics and eutectics

AXIOTHERM	25	-36 to 118	-	140 to 360	-	organics and inorganics
PureTemp	24	-37 to 151	-	145 to 301	-	organics
PCM Energy P. Ltd	24	-50 to 89	105 to 335	-	-	inorganics
Tamai Kasei Co., Ltd.	17	-30 to 50	170 to 320	-	-	-
CRODA	13	-23 to 60	205 to 234	-	-	organics
Global-E-Systems	12	7 to 89.3	149 to 260	-	-	organics and inorganics
PHASECHANGE ENERGY SOLUTIONS	12	4 to 29	tunable	tunable	-	organics
Insolcorp	12	-70 to 22	-	180 to 290	-	-
Climator	11	-21 to 77	116 to 288	-	-	inorganics
Microtek	10	-30 to 57	155 to 240	-	-	organics
savENRG®	6	-24 to 37	185 to 252	-	-	organics and inorganics
BOCA PCM-TES	8	-70 to 83	-	-	-	inorganics
Sasol	5	-10.5 to 41.6	200 to 220	-	-	organics and inorganics
Phase Change Material	6	-30 to 22	-	176 to 275	-	organics and inorganics
Temprecision International	6	-21 to 22	200 to 300	229 to 412	-	-
Cryopak	5	-25 to 27	-	-	-	-
Thermal Custom Packaging	4	-21 to 0	222 to 333	-	-	inorganics
Sunamp	4	-30 to 118	-	-	-	-
Inmark	3	-10 to 21	-	-	13.25	-
SUMMARY	531 total	-74 to 885	70 to 602	120 to 412		

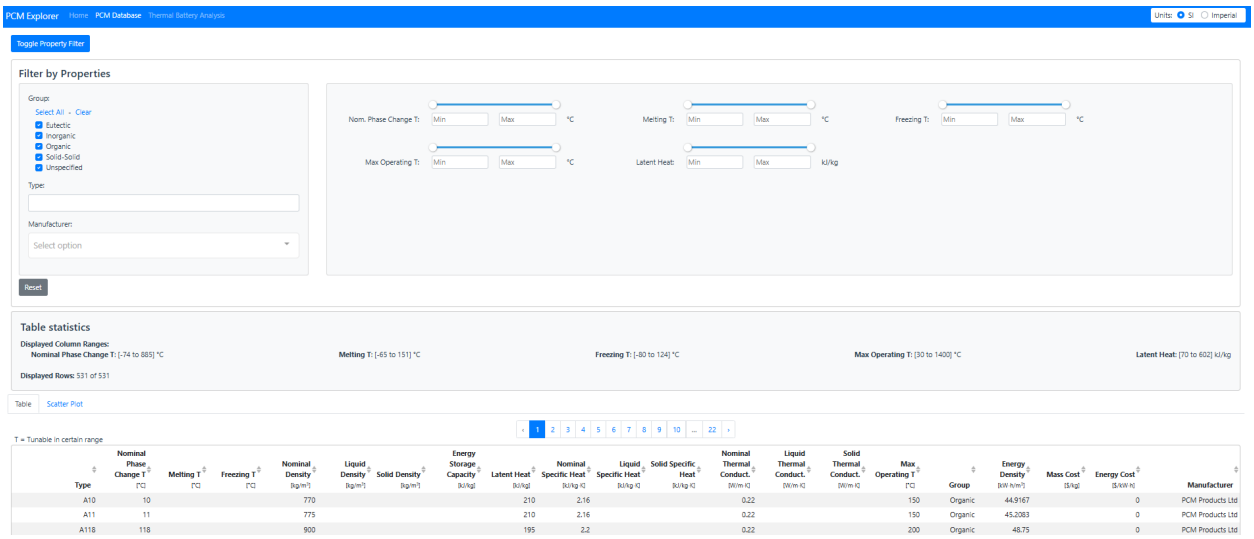

Figure 118: PCM Database UI

Thermal Battery Analysis Tool (M2.3, M3.2)

The thermal battery analysis tool can simulate 4 PCM-HX configurations: (i) Annular-finned PCM-HX; (ii) Serpentine Microchannel PCM-HX; (iii) Longitudinal Fin PCM-HX, (iv) Round tube plate-fin PCM-HX. A screenshot of the web tool UI is shown in Figure 119 for the annular fin-tube PCM-HX geometry. The web tool allows users to connect multiple thermal batteries in parallel for full thermal battery array simulations. Users can also specify any PCM for their simulation (Figure 120).

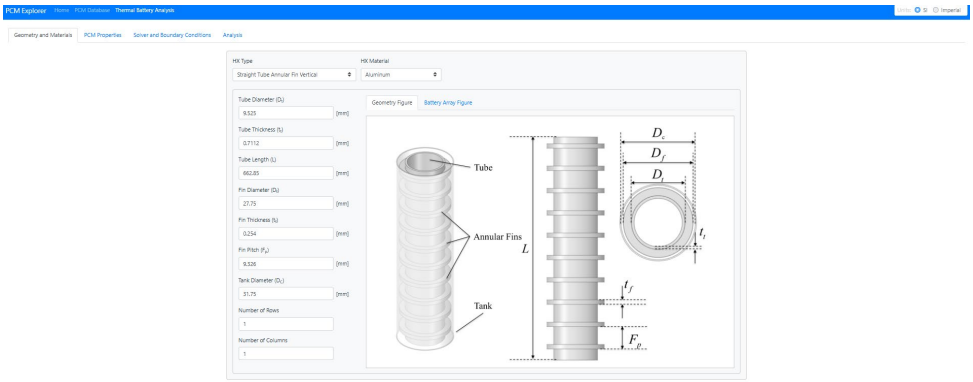

Figure 119: Thermal Battery Analysis Tool UI: Geometry window

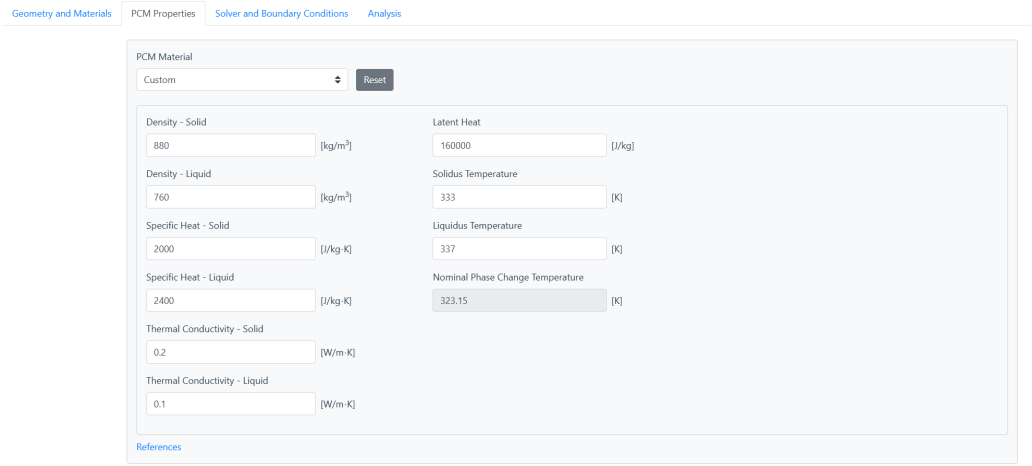

Figure 120: Thermal Battery Analysis Tool UI: PCM Properties window

The available boundary conditions are constant wall temperature, constant heat flux and conjugate heat transfer (Figure 121). For conjugate heat transfer, users can choose between single and two-phase heat transfer fluids using built-in fluids (single-phase: water; two-phase: R134a and R410A). The available heat loss boundary conditions are adiabatic, constant heat flux and convective. The user also chooses one of three grid sizes for model discretization.

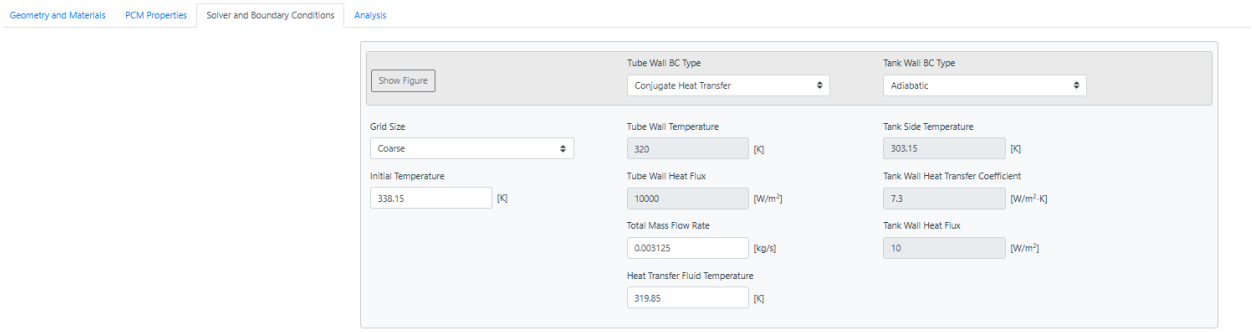

Figure 121: Thermal Battery Analysis Tool UI: Solver & Boundary Conditions window

Figure 122 shows the analysis window of the web tool, where the user selects a time step size and total simulation run time prior to running the simulation. Users can visualize the results as plots for different parameters such as liquid fraction, PCM temperature, energy stored, etc. Users can also download the case file for future use.

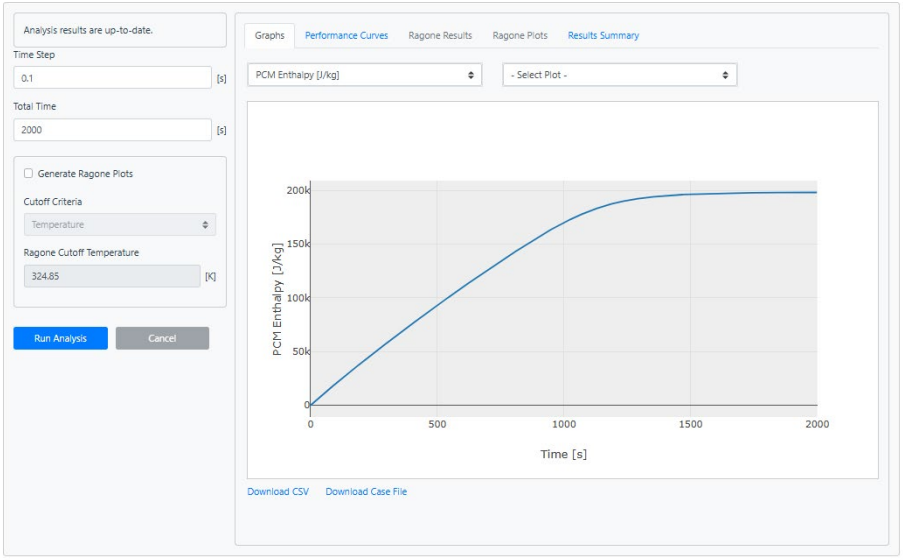

Figure 122: Thermal Battery Analysis Tool UI: Analysis window

For plate-fin and longitudinal fin PCM-HX, performance maps are available when conjugate heat transfer boundary condition is selected. As discussed previously, the performance maps (coefficients for UA equation in W/K) can be downloaded and utilized for full building simulations, e.g., using Spawn of EnergyPlus™ and the Modelica Buildings Library. The performance maps results window is shown in Figure 123.

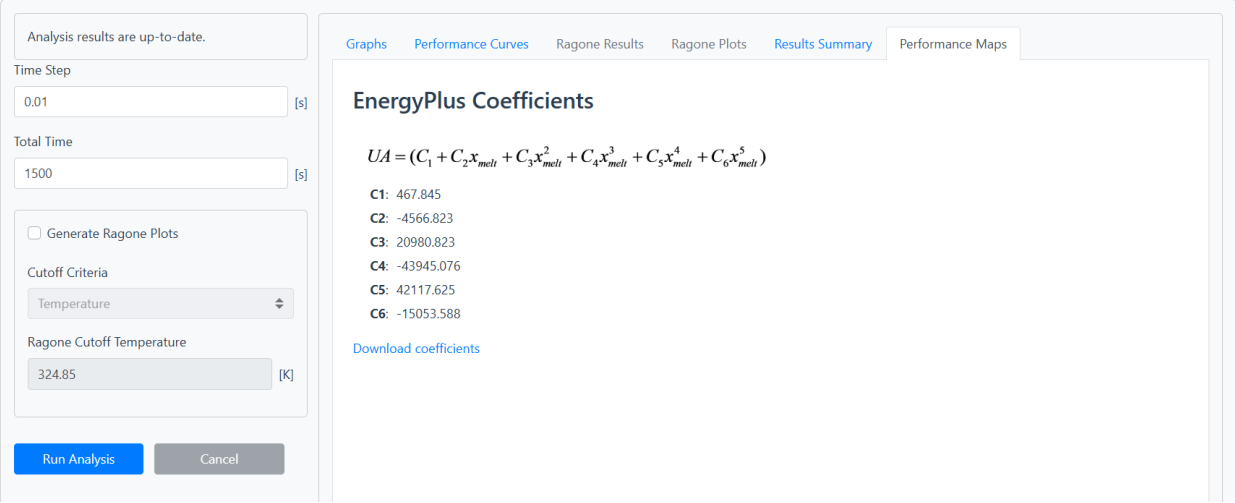

Figure 123: Thermal Battery Analysis Tool UI: Plate-Fin PCM-HX Performance Maps

Significant Accomplishments and Conclusions

PCM-HX Modeling, Analysis and Optimization

- A new comprehensive and experimentally validated PCM-HX design optimization framework based for any PCM-HX configuration on a generalized resistance-capacitance model solver
  - Capable of simulating any working fluid (single-phase and two-phase)
  - Accelerate design and time for HX design optimization: PCM-HX performance assessment up to 1E+05 faster than traditional CFD-based methods with similar accuracy
- The framework utilized to optimize PCM-HXs for a domestic hot water heater application
  - Optimal PCM-HXs can deliver 34-68% of the total daily hot water supply
  - 5-10% package volume increase from the water heater, within U.S. DOE targets for TES systems (<10%)
- Demonstrated an end-to-end workflow for integrating PCM-HX performance maps into building energy simulation tools (i.e., EnergyPlus™) for analyzing the feasibility of space conditioning systems with latent heat PCM-based thermal energy storage
  - Performance map predictions agree with full simulations within ±5% for heat transfer rate, suitable for full building system simulations
- Developed and released a publicly-available PCM web tool
  - https://ceeeweb.umd.edu/pcmapp/
  - PCM property database contains 531 PCMs from 23 OEMs
  - PCM-HX modeling tool for four PCM-HX configurations: Annular Fin-Tube; Serpentine MCHX; Round Tube Plate-Fin HX; Longitudinal Fin-Tube

PCM-HX Manufacturing

- First-order analysis to of promising PCM-HX configurations using 6 of-the-shelf HX products: Flat Plate; Crimped Fins; Spine Fins; Wire Fins; Serpentine MCHX; Annular Fin
  - Serpentine MCHX and Annular Fins identified as the most suitable for PCM-embedded HXs
  - Serpentine-tube Dog-bone fin HXs also an interesting option, but may require additional design changes to extend product lifetime
- 9 PCM-HX prototypes, using additive and conventional manufacturing methods
  - 4 Annular Tubes (1 finless, 3 finned); 1 Helix Tube; 1 Serpentine MCHX; 1 MCHX; 2 Longitudinal Fin-Tube
- Economy-of-scale assessments conducted for aluminum MCHXs, 3D-printed metal PCM-HXs, and Annular Fin-Tubes, good outlook for the next 5-10 years
  - Aluminum MCHXs: Very common in HVAC&R applications with strong economy-of-scale outlook

- 3D Printed Metal HXs: Production growing rapidly, nearly 4x in next 10 years; Still cost-prohibitive at high volumes, but the high design flexibility has significant value proposition, especially for cases where very-high-performance is required
- Annular fin-tube Cost ~ Material Cost + 20% (brazing + additional costing)

PCM-HX Experimentation

- Built two new test facilities for comprehensive PCM-HX component-level testing, including visualizations of PCM melting/solidification
  - PCM-to-single-phase fluid (e.g., water)
  - PCM-to-two-phase fluid (e.g., refrigerant)
- 10 total in-house component-level experiments conducted using the 9 PCM-HX prototypes
  - 9 tests with water as working fluid (single-phase)
  - 1 test with refrigerant (R410A) – to the author's knowledge, the first detailed PCM-HX component-level testing in open literature using phase-changing refrigerant
  - Comprehensive repeatability studies and comparisons of fluid flow direction in the PCM-HX (e.g., downward vs. upward vs. horizontal)
- Experiments used to validate PCM-HX design framework
  - Framework consistently predicted thermal-hydraulic performance within ±10-20% for all cases

Path Forward

Multiple potential avenues for future work have resulted from this work. These are summarized for all three research thrusts (PCM-HX analysis, modeling, & optimization; manufacturing; experimental studies) as below

PCM-HX Modeling, Analysis and Optimization

- Improved PCM-HX modeling
  - Assessments using next-generation working fluids, e.g., R45XX refrigerants, in line with ongoing refrigerant transition
  - Consideration of additional PCM-HX configurations, including 3D GRCM
- Extending PCM-HX optimization capabilities
  - Component-level optimization considering multiple operating conditions, i.e., consider multiple operating conditions / design targets (e.g., capacity, pressure drop)
  - System-level context optimization, e.g., a vapor compression system with a secondary loop integrated with TES
  - Simultaneous optimization of each PCM-HX in a thermal battery array
  - Full PCM-HX topology-optimization
- Address additional physics which may have unforeseen impacts on HX performance and lifespan, including:
  - Surface inhibitors, e.g., internal/external fouling and corrosion
  - Flow maldistribution in TES arrays
- Extending PCM web tool
  - Add new PCM products as new materials / OEMs come online
  - Add new PCM-HX configurations

PCM-HX Manufacturing

- Assess possible future material compatibility issue, e.g., PCM vs. tube/fin material vs. external container
  - E.g., salt hydrate / aluminum compatibility
- Assess conventional manufacturing methods for longitudinal-fin PCM-HXs
  - Depending on the design complexity, longitudinal fin-tubes may be amenable to conventional methods, e.g., extrusion

PCM-HX Experimentation

- Future testing should also consider new next-generation working fluids, e.g., R45XX refrigerants, in line with ongoing refrigerant transition
  - Fluids with high temperature glides might be interesting, especially when matching PCM glides
- TES battery array testing, i.e., multiple TES units in a single PCM bath, toward validating previous assumptions of TES array scaling
- System-level performance assessments, i.e., integrate PCM-HXs with hot water systems, HVAC&R systems, etc.

Products

Journal Publications in Preparation:

Menezes et al. (2025). **Performance Maps based on Resistance-Capacitance Model for Thermal Energy Storage integrated with Heat Pump.** Target Journals: *Applied Thermal Engineering, journal of Energy Storage*

Yang, J., Muehlbauer, J., Lee, C., Hwang, Y. **Two-stage injection air source heat pump with thermal energy storage system**. Target Journal: *International Journal of Heat and Mass Transfer*.

Yang, J., Muehlbauer, J., Lee, C., Hwang, Y., Aute, V. **Experimental validation of the melting topology optimized phase change material embedded heat exchanger**. Target Journal: *International Journal of Heat and Mass Transfer*.

Conference Publications

In Print

Alam, T., et al. (2021). **Numerical Study and Validation of Melting and Solidification in PCM Embedded Heat Exchangers with Straight Tube.** *18th International Refrigeration and Air Conditioning Conference* at Purdue.

Bacellar, D., et al. (2021). **A Study on Computational Cost Reduction of Simulations of Phase-Change Material (PCM) Embedded Heat Exchangers.** *18th International Refrigeration and Air Conditioning Conference* at Purdue.

Bacellar, D., et al. (2021). **Automated Parameterized CFD Simulations of Phase-Change Material Embedded Heat Exchangers.** *20th IEEE Intersociety Conference on Thermal and Thermomechanical Phenomena in Electronic Systems* (iTherm) (pp. 538-543).

Yang, J., et al. (2021). **Experimental Investigation of Melting and Solidification Processes of Phase Change Material Heat Exchanger.** *13th IIR Phase Change Materials and Slurries for Refrigeration and Air Conditioning Conference*, Italy.

Alam, T., et al. (2021). **Effect of thermal expansion coefficient, viscosity and melting range in simulation of PCM embedded heat exchangers with and without fins.** *ASME International Mechanical Engineering Congress and Exposition* (IMECE2021).

Alam, T., et al. (2022). **Development and Validation of Resistance- Capacitance Model for Phase Change Material Embedded in Porous Media.** *21st IEEE Intersociety Conference on Thermal and Thermomechanical Phenomena in Electronic Systems* (iTherm) (pp. 1-7). IEEE.

Alam, T., et al. (2022). **Development and Validation of Resistance-Capacitance Model (RCM) for Phase Change Material (PCM) Embedded in 3D Periodic Structures.** *19th International Refrigeration and Air Conditioning Conference* at Purdue.

Yang, J., et al. (2022). **Experimental Investigation of a Phase Change Material Charged Finned-Tube Heat Exchanger.** *19th International Refrigeration and Air Conditioning Conference* at Purdue.

Yang, J., et al. (2023). **Experimental Investigation of a Phase Change Material Charged Serpentine Heat Exchanger with Louvered Fins.** *14th IEA Heat Pump Conference*, Chicago, IL, USA.

Alam, T. et al. (2024). **Optimization and Experimental Validation of Annular Finned PCM-HX for a Domestic Hot Water Heater Application.** *20th International Refrigeration and Air-Conditioning Conference* at Purdue, July 15-18, 2024.

Menezes, M., et al. (2024). **Development & Experimental Validation of a Generalized Resistance-Capacitance Model for Numerical Simulation of Phase-Change Material Embedded Heat Exchangers.** *20th International Refrigeration and Air-Conditioning Conference* at Purdue.

Yang, J., et al. (2024). **Experimentation on Finned-Tube Microchannel Heat Exchanger Incorporating Phase Change Material and R-410A.** *20th International Refrigeration and Air-Conditioning Conference* at Purdue.

Master Thesis in Print

Alam, T. (2023). **Development, Validation and Application of Resistance-Capacitance Based Models for Phase Change Material Heat Exchangers.** Master Thesis. University of Maryland, College Park.

Project Team & Roles

University of Maryland, College Park (UMCP)

Contribution

PCM-HX design optimization framework & PCM-HX designs

Experimental testing

Project management

Personnel

Vikrant Aute, PI; Research Professor and Director, Center for Environmental Energy Engineering (CEEE)

Yunho Hwang, Co-PI; Research Professor, CEEE

Jan Muehlbauer; Senior Faculty Specialist, CEEE

James Tancabel; Postdoctoral Associate, CEEE

Tanjebul Alam; MS Graduate, CEEE

Jangho Yang, Graduate Research Assistant, CEEE

Mylena Menezes; Graduate Research Assistant, CEEE

Heat Transfer Technologies, LLC (HTT)

Contribution

PCM-HX prototyping

Manufacturing costs / Economy-of-scale assessments

Personnel

Yoram Shabtay, Co-PI; President, HTT

John Black; V.P. Market Development, HTT

Naomi Carmeli-Shabtay; R&D Engineer, HTT

References

[1] Tanjebul Alam, “DEVELOPMENT, VALIDATION AND APPLICATION OF RESISTANCE CAPACITANCE BASED MODELS (RCM) FOR PHASE CHANGE MATERIAL HEAT EXCHANGERS,” Master of Science, University of Maryland, College Park, 2023.

[2] “EIA projects nearly 50% increase in world energy usage by 2050, led by growth in Asia.” [Online]. Available: https://www.eia.gov/todayinenergy/detail.php?id=41433

[3] M. González-Torres, L. Pérez-Lombard, J. F. Coronel, I. R. Maestre, and D. Yan, “A review on buildings energy information: Trends, end-uses, fuels and drivers,” *Energy Rep.*, vol. 8, pp. 626–637, 2022, doi: https://doi.org/10.1016/j.egyr.2021.11.280.

[4] I. Dincer and M. A. Ezan, *Heat Storage: A Unique Solution For Energy Systems*. 2018. doi: 10.1007/978-3-319-91893-8_3.

[5] Patrick E. Hopkins, “Bio-based phase change materials (PCMs) for thermal energy storage,”

[6] I. Sarbu and C. Sebarchievici, “A comprehensive review of thermal energy storage,” *Sustain. Switz.*, vol. 10, no. 1, 2018, doi: 10.3390/su10010191.

[7] G. Karmiris and T. Tengnér, “Peak Shaving Control Method for Energy Storage,” *Electical Energy Storage Appl. Technol.*, pp. 1–6, 2013.

[8] A. Elgafy and K. Lafdi, “Effect of carbon nanofiber additives on thermal behavior of phase change materials,” *Carbon*, vol. 43, no. 15, pp. 3067–3074, 2005, doi: 10.1016/j.carbon.2005.06.042.

[9] P. Lamberg and K. Sirén, “Approximate analytical model for solidification in a finite PCM storage with internal fins,” *Appl. Math. Model.*, vol. 27, no. 7, pp. 491–513, 2003, doi: 10.1016/S0307-904X(03)00080-5.

[10] B. Šarler, “Stefan’s work on solid-liquid phase changes,” *Eng. Anal. Bound. Elem.*, vol. 16, no. 2, pp. 83–92, 1995, doi: https://doi.org/10.1016/0955-7997(95)00047-X.

[11] P. J. Shamberger, “Cooling Capacity Figure of Merit for Phase Change Materials,” *J. Heat Transf.*, vol. 138, no. 2, pp. 1–8, 2016, doi: 10.1115/1.4031252.

[12] H. Hu *et al.*, “Modelling and Simulation in Materials Science and Engineering Mathematical modelling of solidification and melting : a review Mathematical modelling of solidification and melting : a review,” 1996.

[13] K. Yazawa, P. J. Shamberger, and T. S. Fisher, “Ragone Relations for Thermal Energy Storage Technologies,” *Front. Mech. Eng.*, vol. 5, no. June, 2019, doi: 10.3389/fmech.2019.00029.

[14] A. A. Al-Abidi, S. Mat, K. Sopian, M. Y. Sulaiman, and A. T. Mohammad, “Numerical study of PCM solidification in a triplex tube heat exchanger with internal and external fins,” *Int. J. Heat Mass Transf.*, vol. 61, no. 1, pp. 684–695, 2013, doi: 10.1016/j.ijheatmasstransfer.2013.02.030.

[15] A. Ebrahimi, M. J. Hosseini, A. A. Ranjbar, M. Rahimi, and R. Bahrampoury, “Melting process investigation of phase change materials in a shell and tube heat exchanger enhanced with heat pipe,” *Renew. Energy*, vol. 138, pp. 378–394, 2019, doi: 10.1016/j.renene.2019.01.110.

[16] M. Esapour, A. Hamzehnezhad, A. A. Rabienataj Darzi, and M. Jourabian, “Melting and solidification of PCM embedded in porous metal foam in horizontal multi-tube heat storage system,” *Energy Convers. Manag.*, vol. 171, no. January, pp. 398–410, 2018, doi: 10.1016/j.enconman.2018.05.086.

[17] R. Karami and B. Kamkari, “Experimental investigation of the effect of perforated fins on thermal performance enhancement of vertical shell and tube latent heat energy storage systems,” *Energy Convers. Manag.*, vol. 210, no. November 2019, p. 112679, 2020, doi: 10.1016/j.enconman.2020.112679.

[18] M. K. Koukou, M. G. Vrachopoulos, N. S. Tachos, G. Dogkas, K. Lymperis, and V. Stathopoulos, “Experimental and computational investigation of a latent heat energy storage system with a staggered heat exchanger for various phase change materials,” *Therm. Sci. Eng. Prog.*, vol. 7, no. May, pp. 87–98, 2018, doi: 10.1016/j.tsep.2018.05.004.

[19] Z. Liu, Y. Yao, and H. Wu, “Numerical modeling for solid-liquid phase change phenomena in porous media: Shell-and-tube type latent heat thermal energy storage,” *Appl. Energy*, vol. 112, pp. 1222–1232, 2013, doi: 10.1016/j.apenergy.2013.02.022.

[20] M. Longeon, A. Soupart, J. F. Fourmigué, A. Bruch, and P. Marty, “Experimental and numerical study of annular PCM storage in the presence of natural convection,” *Appl. Energy*, vol. 112, pp. 175–184, 2013, doi: 10.1016/j.apenergy.2013.06.007.

[21] M. S. Mahdi *et al.*, “Numerical study and experimental validation of the effects of orientation and configuration on melting in a latent heat thermal storage unit,” *J. Energy Storage*, vol. 23, no. November 2018, pp. 456–468, 2019, doi: 10.1016/j.est.2019.04.013.

[22] S. Mat, A. A. Al-Abidi, K. Sopian, M. Y. Sulaiman, and A. T. Mohammad, “Enhance heat transfer for PCM melting in triplex tube with internal-external fins,” *Energy Convers. Manag.*, vol. 74, pp. 223–236, 2013, doi: 10.1016/j.enconman.2013.05.003.

[23] L. Pu, S. Zhang, L. Xu, and Y. Li, “Thermal performance optimization and evaluation of a radial finned shell-and-tube latent heat thermal energy storage unit,” *Appl. Therm. Eng.*, vol. 166, no. November 2019, p. 114753, 2020, doi: 10.1016/j.applthermaleng.2019.114753.

[24] N. H. S. Tay, F. Bruno, and M. Belusko, “Comparison of pinned and finned tubes in a phase change thermal energy storage system using CFD,” *Appl. Energy*, vol. 104, pp. 79–86, 2013, doi: 10.1016/j.apenergy.2012.10.040.

[25] X. Yang, J. Guo, B. Yang, H. Cheng, P. Wei, and Y. L. He, “Design of non-uniformly distributed annular fins for a shell-and-tube thermal energy storage unit,” *Appl. Energy*, vol. 279, no. July, p. 115772, 2020, doi: 10.1016/j.apenergy.2020.115772.

[26] X. Yang, Z. Lu, Q. Bai, Q. Zhang, L. Jin, and J. Yan, “Thermal performance of a shell-and-tube latent heat thermal energy storage unit: Role of annular fins,” *Appl. Energy*, vol. 202, pp. 558–570, 2017, doi: 10.1016/j.apenergy.2017.05.007.

[27] W. Youssef, Y. T. Ge, and S. A. Tassou, “CFD modelling development and experimental validation of a phase change material (PCM) heat exchanger with spiral-wired tubes,” *Energy Convers. Manag.*, vol. 157, no. December 2017, pp. 498–510, 2018, doi: 10.1016/j.enconman.2017.12.036.

[28] P. Zhang, Z. N. Meng, H. Zhu, Y. L. Wang, and S. P. Peng, “Melting heat transfer characteristics of a composite phase change material fabricated by paraffin and metal foam,” *Appl. Energy*, vol. 185, pp. 1971–1983, 2017, doi: 10.1016/j.apenergy.2015.10.075.

[29] S. Zhang, L. Pu, L. Xu, R. Liu, and Y. Li, “Melting performance analysis of phase change materials in different finned thermal energy storage,” *Appl. Therm. Eng.*, vol. 176, no. April, p. 115425, 2020, doi: 10.1016/j.applthermaleng.2020.115425.

[30] F. Zhu, C. Zhang, and X. Gong, “Numerical analysis and comparison of the thermal performance enhancement methods for metal foam/phase change material composite,” *Appl. Therm. Eng.*, vol. 109, pp. 373–383, 2016, doi: 10.1016/j.applthermaleng.2016.08.088.

[31] D. Bacellar, T. Alam, J. Ling, and V. Aute, “A Study on Computational Cost Reduction of Simulations of Phase-Change Material (PCM) Embedded Heat Exchangers,” in *18th International Refrigeration and Air Conditioning Conference at Purdue*, 2021, pp. 1–9.

[32] D. Bacellar, T. Alam, J. Ling, and V. Aute, “Automated Parameterized CFD Simulations of Phase-Change Material Embedded Heat Exchangers,” *2021 20th IEEE Intersoc. Conf. Therm. Thermomechanical Phenom. Electron. Syst. ITherm*, pp. 538–543, 2021, doi: 10.1109/itherm51669.2021.9503249.

[33] M. S. Mahdi, H. B. Mahood, J. M. Mahdi, A. A. Khadom, and A. N. Campbell, “Improved PCM melting in a thermal energy storage system of double-pipe helical-coil tube,” *Energy Convers. Manag.*, vol. 203, no. September 2019, p. 112238, 2020, doi: 10.1016/j.enconman.2019.112238.

[34] A. Ebrahimi, M. J. Hosseini, A. A. Ranjbar, M. Rahimi, and R. Bahrampoury, “Melting process investigation of phase change materials in a shell and tube heat exchanger enhanced with heat pipe,” *Renew. Energy*, vol. 138, pp. 378–394, 2019, doi: 10.1016/j.renene.2019.01.110.

[35] A. F. Di Rienzo, “Mesoscopic Numerical Methods for Reactive Flows: Lattice Boltzmann Method and Beyond,” 2012.

[36] K.-R. K. Wichmann, “Performance Aspects of Incompressible Navier-Stokes Solvers: Lattice-Boltzmann Method vs. Finite Difference Method,” 2019.

[37] Q. Li, K. H. Luo, Q. J. Kang, Y. L. He, Q. Chen, and Q. Liu, “Lattice Boltzmann methods for multiphase flow and phase-change heat transfer,” *Prog. Energy Combust. Sci.*, vol. 52, no. 0, pp. 62–105, 2016, doi: 10.1016/j.pecs.2015.10.001.

[38] Q. Liu and Y. L. He, “Double multiple-relaxation-time lattice Boltzmann model for solid-liquid phase change with natural convection in porous media,” *Phys. Stat. Mech. Its Appl.*, vol. 438, pp. 94–106, 2015, doi: 10.1016/j.physa.2015.06.018.

[39] D. Gao, Z. Chen, D. Zhang, and L. Chen, “Lattice Boltzmann modeling of melting of phase change materials in porous media with conducting fins,” *Appl. Therm. Eng.*, vol. 118, pp. 315–327, 2017, doi: 10.1016/j.applthermaleng.2017.03.002.

[40] D. Li, Q. Ren, Z. X. Tong, and Y. L. He, “Lattice Boltzmann models for axisymmetric solid–liquid phase change,” *Int. J. Heat Mass Transf.*, vol. 112, pp. 795–804, 2017, doi: 10.1016/j.ijheatmasstransfer.2017.03.127.

[41] E. M. Sparrow, J. W. Ramsey, and R. G. Kemink, “Freezing Controlled by Natural Convection,” *J. Heat Transf.*, vol. 101, no. 4, pp. 578–584, Nov. 1979, doi: 10.1115/1.3451040.

[42] D. Chen, A. Riaz, V. C. Aute, and R. Radermacher, “A solid–liquid model based on lattice Boltzmann method for phase change material melting with porous media in cylindrical heat exchangers,” *Appl. Therm. Eng.*, vol. 207, no. January, p. 118080, 2022, doi: 10.1016/j.applthermaleng.2022.118080.

[43] M. Martinelli, F. Bentivoglio, A. Caron-Soupart, R. Couturier, J. F. Fourmigue, and P. Marty, “Experimental study of a phase change thermal energy storage with copper foam,” *Appl. Therm. Eng.*, vol. 101, pp. 247–261, 2016, doi: 10.1016/j.applthermaleng.2016.02.095.

[44] E. H. Mathews, P. G. Richards, and C. Lombard, “A first-order thermal model for building design,” *Energy Build.*, vol. 21, no. 2, pp. 133–145, 1994, doi: 10.1016/0378-7788(94)90006-X.

[45] A. Zarrella, A. Capozza, and M. De Carli, “Analysis of short helical and double U-tube borehole heat exchangers: A simulation-based comparison,” *Appl. Energy*, vol. 112, pp. 358–370, 2013, doi: 10.1016/j.apenergy.2013.06.032.

[46] N. Zhu, S. Wang, X. Xu, and Z. Ma, “A simplified dynamic model of building structures integrated with shaped-stabilized phase change materials,” *Int. J. Therm. Sci.*, vol. 49, no. 9, pp. 1722–1731, 2010, doi: 10.1016/j.ijthermalsci.2010.03.020.

[47] A. Bontemps, M. Ahmad, K. Johanns, and H. Sallée, “Experimental and modelling study of twin cells with latent heat storage walls,” *Energy Build.*, vol. 43, no. 9, pp. 2456–2461, 2011, doi: 10.1016/j.enbuild.2011.05.030.

[48] J. Gao, T. Yan, T. Xu, Z. Ling, G. Wei, and X. Xu, “Development and experiment validation of variable-resistance-variable-capacitance dynamic simplified thermal models for shape-stabilized phase change material slab,” *Appl. Therm. Eng.*, vol. 146, no. July 2018, pp. 364–375, 2019, doi: 10.1016/j.applthermaleng.2018.09.124.

[49] A. Stupar, U. Drofenik, and J. W. Kolar, “Application of phase change materials for low duty cycle high peak load power supplies,” *2010 6th Int. Conf. Integr. Power Electron. Syst. CIPS 2010*, pp. 16–18, 2011.

[50] P. A. Mirzaei and F. Haghighat, “Modeling of phase change materials for applications in whole building simulation,” *Renew. Sustain. Energy Rev.*, vol. 16, no. 7, pp. 5355–5362, 2012, doi: 10.1016/j.rser.2012.04.053.

[51] C. Pan, S. Hoenig, C. H. Chen, S. Neti, C. Romero, and N. Vermaak, “Efficient modeling of phase change material solidification with multidimensional fins,” *Int. J. Heat Mass Transf.*, vol. 115, pp. 897–909, 2017, doi: 10.1016/j.ijheatmasstransfer.2017.07.120.

[52] M. Parsazadeh, Z. Liu, and X. Duan, “An improved layered thermal resistance model for solid-liquid phase change time estimation,” *Int. J. Therm. Sci.*, vol. 156, no. June, p. 106496, 2020, doi: 10.1016/j.ijthermalsci.2020.106496.

[53] H. Neumann, S. Gamisch, and S. Gschwander, “Comparison of RC-model and FEM-model for a PCM-plate storage including free convection,” *Appl. Therm. Eng.*, vol. 196, no. September 2020, p. 117232, 2021, doi: 10.1016/j.applthermaleng.2021.117232.

[54] J. Vogel, J. Felbinger, and M. Johnson, “Natural convection in high temperature flat plate latent heat thermal energy storage systems,” *Appl. Energy*, vol. 184, pp. 184–196, 2016, doi: 10.1016/j.apenergy.2016.10.001.

[55] E. Fleming, S. Wen, L. Shi, and A. K. Da Silva, “Experimental and theoretical analysis of an aluminum foam enhanced phase change thermal storage unit,” *Int. J. Heat Mass Transf.*, vol. 82, pp. 273–281, 2015, doi: 10.1016/j.ijheatmasstransfer.2014.11.022.

[56] H. Zheng, C. Wang, Q. Liu, Z. Tian, and X. Fan, “Thermal performance of copper foam/paraffin composite phase change material,” *Energy Convers. Manag.*, vol. 157, no. September 2017, pp. 372–381, 2018, doi: 10.1016/j.enconman.2017.12.023.

[57] F. Agyenim, P. Eames, and M. Smyth, “A comparison of heat transfer enhancement in a medium temperature thermal energy storage heat exchanger using fins,” *Sol. Energy*, vol. 83, no. 9, pp. 1509–1520, 2009, doi: 10.1016/j.solener.2009.04.007.

[58] N. H. S. Tay, F. Bruno, and M. Belusko, “Experimental validation of a CFD and an ε-NTU model for a large tube-in-tank PCM system,” *Int. J. Heat Mass Transf.*, vol. 55, no. 21–22, pp. 5931–5940, 2012, doi: 10.1016/j.ijheatmasstransfer.2012.06.004.

[59] V. Saydam, M. Parsazadeh, M. Radeef, and X. Duan, “Design and experimental analysis of a helical coil phase change heat exchanger for thermal energy storage,” *J. Energy Storage*, vol. 21, no. February 2018, pp. 9–17, 2019, doi: 10.1016/j.est.2018.11.006.

[60] L. Jian-you, “Numerical and experimental investigation for heat transfer in triplex concentric tube with phase change material for thermal energy storage,” *Sol. Energy*, vol. 82, no. 11, pp. 977–985, 2008, doi: 10.1016/j.solener.2008.05.006.

[61] J. M. Mahdi and E. C. Nsofor, “Solidification enhancement of PCM in a triplex-tube thermal energy storage system with nanoparticles and fins,” *Appl. Energy*, vol. 211, no. May 2017, pp. 975–986, 2018, doi: 10.1016/j.apenergy.2017.11.082.

[62] J. M. Mahdi and E. C. Nsofor, “Melting enhancement in triplex-tube latent thermal energy storage system using nanoparticles-fins combination,” *Int. J. Heat Mass Transf.*, vol. 109, pp. 417–427, 2017, doi: 10.1016/j.ijheatmasstransfer.2017.02.016.

[63] Z. Hu, A. Li, R. Gao, and H. Yin, “Enhanced heat transfer for PCM melting in the frustum-shaped unit with multiple PCMs,” *J. Therm. Anal. Calorim.*, vol. 120, no. 2, pp. 1407–1416, 2015, doi: 10.1007/s10973-014-4370-6.

[64] M. Akgün, O. Aydin, and K. Kaygusuz, “Experimental study on melting/solidification characteristics of a paraffin as PCM,” *Energy Convers. Manag.*, vol. 48, no. 2, pp. 669–678, 2007, doi: 10.1016/j.enconman.2006.05.014.

[65] M. Faghani, M. J. Hosseini, and R. Bahrampoury, “Numerical simulation of melting between two elliptical cylinders,” *Alex. Eng. J.*, vol. 57, no. 2, pp. 577–586, 2018, doi: 10.1016/j.aej.2017.02.003.

[66] E. Assis, L. Katsman, G. Ziskind, and R. Letan, “Numerical and experimental study of melting in a spherical shell,” *Int. J. Heat Mass Transf.*, vol. 50, no. 9–10, pp. 1790–1804, 2007, doi: 10.1016/j.ijheatmasstransfer.2006.10.007.

[67] C. Zhao, M. Opolot, M. Liu, F. Bruno, S. Mancin, and K. Hooman, “Numerical study of melting performance enhancement for PCM in an annular enclosure with internal-external fins and metal foams,” *Int. J. Heat Mass Transf.*, vol. 150, p. 119348, 2020, doi: 10.1016/j.ijheatmasstransfer.2020.119348.

[68] A. A. Al-Abidi, S. Mat, K. Sopian, M. Y. Sulaiman, and A. T. Mohammad, “Internal and external fin heat transfer enhancement technique for latent heat thermal energy storage in triplex tube heat exchangers,” *Appl. Therm. Eng.*, vol. 53, no. 1, pp. 147–156, 2013, doi: 10.1016/j.applthermaleng.2013.01.011.

[69] X. Y. Zhang, Y. T. Ge, Burra, and P. Y. Lang, “Experimental investigation and CFD modelling analysis of finned-tube PCM heat exchanger for space heating,” *Appl. Therm. Eng.*, vol. 244, p. 122731, May 2024, doi: 10.1016/j.applthermaleng.2024.122731.

[70] M. K. Fahad, S. Subah, N. F. Ifraj, S. H. Tahsin, T. R. Alvi, and Md. J. Hasan, “Comparative analysis on melting performance of PCM using rectangular and branching fin configurations in a shell and tube type thermal energy storing unit,” *J. Energy Storage*, vol. 91, p. 112048, Jun. 2024, doi: 10.1016/j.est.2024.112048.

[71] V. Safari, H. Abolghasemi, L. Darvishvand, and B. Kamkari, “Thermal performance investigation of concentric and eccentric shell and tube heat exchangers with different fin configurations containing phase change material,” *J. Energy Storage*, vol. 37, p. 102458, May 2021, doi: 10.1016/j.est.2021.102458.

[72] J. C. Kurnia and A. P. Sasmito, “Numerical investigation of heat transfer performance of a rotating latent heat thermal energy storage,” *Appl. Energy*, vol. 227, pp. 542–554, Oct. 2018, doi: 10.1016/j.apenergy.2017.08.087.

[73] M. Lacroix, “Numerical simulation of a shell-and-tube latent heat thermal energy storage unit,” *Sol. Energy*, vol. 50, no. 4, pp. 357–367, 1993, doi: https://doi.org/10.1016/0038-092X(93)90029-N.

[74] Z. Liu, Y. Yao, and H. Wu, “Numerical modeling for solid–liquid phase change phenomena in porous media: Shell-and-tube type latent heat thermal energy storage,” *Appl. Energy*, vol. 112, pp. 1222–1232, Dec. 2013, doi: 10.1016/j.apenergy.2013.02.022.

[75] Y. Tian and C. Y. Zhao, “A numerical investigation of heat transfer in phase change materials (PCMs) embedded in porous metals,” *Energy*, vol. 36, no. 9, pp. 5539–5546, Sep. 2011, doi: 10.1016/j.energy.2011.07.019.

[76] V. K. Yadav, M. Jee, J. Sarkar, and P. Ghosh, “Novel metal foam and phase change material integrated multi-tube heat exchanger design for simultaneous charging and discharging,” *J. Energy Storage*, vol. 117, p. 116109, May 2025, doi: 10.1016/j.est.2025.116109.

[77] T.- Rehman, H. M. Ali, A. Saieed, W. Pao, and M. Ali, “Copper foam/PCMs based heat sinks: An experimental study for electronic cooling systems,” *Int. J. Heat Mass Transf.*, vol. 127, pp. 381–393, Dec. 2018, doi: 10.1016/j.ijheatmasstransfer.2018.07.120.

[78] X. Yang, Z. Lu, Q. Bai, Q. Zhang, L. Jin, and J. Yan, “Thermal performance of a shell-and-tube latent heat thermal energy storage unit: Role of annular fins,” *Appl. Energy*, vol. 202, pp. 558–570, Sep. 2017, doi: 10.1016/j.apenergy.2017.05.007.

[79] M. Longeon, A. Soupart, J.-F. Fourmigué, A. Bruch, and P. Marty, “Experimental and numerical study of annular PCM storage in the presence of natural convection,” *Appl. Energy*, vol. 112, pp. 175–184, Dec. 2013, doi: 10.1016/j.apenergy.2013.06.007.

[80] S. Baghaei Oskouei and Ö. Bayer, “Experimental and numerical investigation of melting and solidification enhancement using Fibonacci-inspired fins in a latent thermal energy storage unit,” *Int. J. Heat Mass Transf.*, vol. 210, p. 124180, Aug. 2023, doi: 10.1016/j.ijheatmasstransfer.2023.124180.

[81] A. Najafian, F. Haghighat, and A. Moreau, “Integration of PCM in domestic hot water tanks: Optimization for shifting peak demand,” *Energy Build.*, vol. 106, pp. 59–64, 2015, doi: 10.1016/j.enbuild.2015.05.036.

[82] G. Righetti, R. Lazzarin, M. Noro, and S. Mancin, “Phase change materials embedded in porous matrices for hybrid thermal energy storages: Experimental results and modeling,” *Int. J. Refrig.*, vol. 106, pp. 266–277, 2019, doi: 10.1016/j.ijrefrig.2019.06.018.

[83] R. Dhumane *et al.*, “Improving system performance of a personal conditioning system integrated with thermal storage,” *Appl. Therm. Eng.*, vol. 147, no. August 2018, pp. 40–51, 2019, doi: 10.1016/j.applthermaleng.2018.10.004.

[84] Y. Du, J. Muehlbauer, J. Ling, V. Aute, Y. Hwang, and R. Radermacher, “RECHARGEABLE PERSONAL AIR CONDITIONING DEVICE,” in *ASME 2016 10th International Conference on Energy Sustainability,Charlotte, North Carolina*, Charlotte, North Carolina, 2016.

[85] R. Dhumane *et al.*, “Enhancing the thermosiphon-driven discharge of a latent heat thermal storage system used in a personal cooling device,” *Int. J. Refrig.*, vol. 88, pp. 599–613, 2018, doi: 10.1016/j.ijrefrig.2018.02.005.

[86] Y. Du, “BATTERY POWERED PORTABLE VAPOR COMPRESSION CYCLE SYSTEM WITH PCM CONDENSER,” 2016.

[87] P. Promoppatum, S. C. Yao, T. Hultz, and D. Agee, “Experimental and numerical investigation of the cross-flow PCM heat exchanger for the energy saving of building HVAC,” *Energy Build.*, vol. 138, pp. 468–478, 2017, doi: 10.1016/j.enbuild.2016.12.043.

[88] H. L. Zhang, J. Baeyens, J. Degrève, G. Cáceres, R. Segal, and F. Pitié, “Latent heat storage with tubular-encapsulated phase change materials (PCMs),” *Energy*, vol. 76, pp. 66–72, 2014, doi: 10.1016/j.energy.2014.03.067.

[89] N. Calvet, X. Py, R. Olivès, J. P. Bédécarrats, J. P. Dumas, and F. Jay, “Enhanced performances of macro-encapsulated phase change materials (PCMs) by intensification of the internal effective thermal conductivity,” *Energy*, vol. 55, pp. 956–964, 2013, doi: 10.1016/j.energy.2013.03.078.

[90] R. Velraj, R. V. Seeniraj, B. Hafner, C. Faber, and K. Schwarzer, “Experimental analysis and numerical modelling of inward solidification on a finned vertical tube for a latent heat storage unit,” *Sol. Energy*, vol. 60, no. 5, pp. 281–290, 1997, doi: 10.1016/S0038-092X(96)00167-3.

[91] K. A. R. Ismail, C. L. F. Alves, and M. S. Modesto, “Numerical and experimental study on the solidification of PCM around a vertical axially finned isothermal cylinder,” *Appl. Therm. Eng.*, vol. 21, no. 1, pp. 53–77, 2001, doi: 10.1016/S1359-4311(00)00002-8.

[92] A. Erek, Z. Ilken, and M. A. Acar, “Experimental and numerical investigation of thermal energy storage with a finned tube,” *Int. J. Energy Res.*, vol. 29, no. 4, pp. 283–301, 2005, doi: 10.1002/er.1057.

[93] D. Li, Q. Ren, Z. X. Tong, and Y. L. He, “Lattice Boltzmann models for axisymmetric solid–liquid phase change,” *Int. J. Heat Mass Transf.*, vol. 112, pp. 795–804, 2017, doi: 10.1016/j.ijheatmasstransfer.2017.03.127.

[94] Q. Liu, X. B. Feng, Y. L. He, C. W. Lu, and Q. H. Gu, “Multiple-relaxation-time lattice Boltzmann model for simulating axisymmetric thermal flows in porous media,” *Int. J. Heat Mass Transf.*, vol. 137, pp. 1301–1311, 2019, doi: 10.1016/j.ijheatmasstransfer.2019.03.118.

[95] Z. Ling, W. Lin, Z. Zhang, and X. Fang, “Computationally efficient thermal network model and its application in optimization of battery thermal management system with phase change materials and long-term performance assessment,” *Appl. Energy*, vol. 259, p. 114120, Feb. 2020, doi: 10.1016/j.apenergy.2019.114120.

[96] A. Singh, S. Rangarajan, L. Choobineh, and B. Sammakia, “Experimental investigation and comparative analysis of organic and metallic phase change materials using thermal Ragone plots,” *Appl. Therm. Eng.*, vol. 262, p. 125265, Mar. 2025, doi: 10.1016/j.applthermaleng.2024.125265.

[97] R. Elarem *et al.*, “A comprehensive review of heat transfer intensification methods for latent heat storage units,” *Energy Storage*, vol. 3, no. 1, p. e127, Feb. 2021, doi: 10.1002/est2.127.

[98] B. Buonomo, M. Rita Golia, O. Manca, and S. Nardini, “A review on thermal energy storage with phase change materials enhanced by metal foams,” *Therm. Sci. Eng. Prog.*, vol. 53, p. 102732, Aug. 2024, doi: 10.1016/j.tsep.2024.102732.

[99] A. M. Abdulateef, S. Mat, J. Abdulateef, K. Sopian, and A. A. Al-Abidi, “Geometric and design parameters of fins employed for enhancing thermal energy storage systems: a review,” *Renew. Sustain. Energy Rev.*, vol. 82, pp. 1620–1635, Feb. 2018, doi: 10.1016/j.rser.2017.07.009.

[100] N. I. Ibrahim, F. A. Al-Sulaiman, S. Rahman, B. S. Yilbas, and A. Z. Sahin, “Heat transfer enhancement of phase change materials for thermal energy storage applications: A critical review,” *Renew. Sustain. Energy Rev.*, vol. 74, no. February, pp. 26–50, 2017, doi: 10.1016/j.rser.2017.01.169.

[101] J. C. Choi, S. D. Kim, and G. Y. Han, “Heat transfer characteristics in low-temperature latent heat storage systems using salt hydrates,” *Korean J. Chem. Eng.*, vol. 12, no. 2, pp. 258–263, 1995, doi: 10.1007/BF02705655.

[102] M. Kazemi, M. J. Hosseini, A. A. Ranjbar, and R. Bahrampoury, “Improvement of longitudinal fins configuration in latent heat storage systems,” *Renew. Energy*, vol. 116, pp. 447–457, 2018, doi: 10.1016/j.renene.2017.10.006.

[103] Y. B. Tao and Y. L. He, “Effects of natural convection on latent heat storage performance of salt in a horizontal concentric tube,” *Appl. Energy*, vol. 143, pp. 38–46, 2015, doi: 10.1016/j.apenergy.2015.01.008.

[104] R. Amini, M. Amini, A. Jafarinia, and M. Kashfi, “Numerical investigation on effects of using segmented and helical tube fins on thermal performance and efficiency of a shell and tube heat exchanger,” *Appl. Therm. Eng.*, vol. 138, no. January, pp. 750–760, 2018, doi: 10.1016/j.applthermaleng.2018.03.004.

[105] Z. Khan and Z. A. Khan, “An experimental investigation of discharge/solidification cycle of paraffin in novel shell and tube with longitudinal fins based latent heat storage system,” *Energy Convers. Manag.*, vol. 154, pp. 157–167, 2017, doi: 10.1016/j.enconman.2017.10.051.

[106] U. Stritih, “An experimental study of enhanced heat transfer in rectangular PCM thermal storage,” *Int. J. Heat Mass Transf.*, vol. 47, no. 12–13, pp. 2841–2847, 2004, doi: 10.1016/j.ijheatmasstransfer.2004.02.001.

[107] Z. Liu, X. Sun, and C. Ma, “Experimental investigations on the characteristics of melting processes of stearic acid in an annulus and its thermal conductivity enhancement by fins,” *Energy Convers. Manag.*, vol. 46, no. 6, pp. 959–969, 2005, doi: 10.1016/j.enconman.2004.05.012.

[108] D. Zhao and G. Tan, “Numerical analysis of a shell-and-tube latent heat storage unit with fins for air-conditioning application,” *Appl. Energy*, vol. 138, pp. 381–392, 2015, doi: 10.1016/j.apenergy.2014.10.051.

[109] M. Rahimi, A. A. Ranjbar, D. D. Ganji, K. Sedighi, M. J. Hosseini, and R. Bahrampoury, “Analysis of geometrical and operational parameters of PCM in a fin and tube heat exchanger,” *Int. Commun. Heat Mass Transf.*, vol. 53, pp. 109–115, 2014, doi: 10.1016/j.icheatmasstransfer.2014.02.025.

[110] V. Shatikian, G. Ziskind, and R. Letan, “Numerical investigation of a PCM-based heat sink with internal fins,” *Int. J. Heat Mass Transf.*, vol. 48, no. 17, pp. 3689–3706, 2005, doi: 10.1016/j.ijheatmasstransfer.2004.10.042.

[111] M. Gharebaghi and I. Sezai, “Enhancement of heat transfer in latent heat storage modules with internal fins,” *Numer. Heat Transf. Part Appl.*, vol. 53, no. 7, pp. 749–765, 2008, doi: 10.1080/10407780701715786.

[112] S. F. Hosseinizadeh, F. L. Tan, and S. M. Moosania, “Experimental and numerical studies on performance of PCM-based heat sink with different configurations of internal fins,” *Appl. Therm. Eng.*, vol. 31, no. 17–18, pp. 3827–3838, 2011, doi: 10.1016/j.applthermaleng.2011.07.031.

[113] N. Sharifi, T. L. Bergman, and A. Faghri, “Enhancement of PCM melting in enclosures with horizontally-finned internal surfaces,” *Int. J. Heat Mass Transf.*, vol. 54, no. 19–20, pp. 4182–4192, 2011, doi: 10.1016/j.ijheatmasstransfer.2011.05.027.

[114] I. Jmal and M. Baccar, “Numerical study of PCM solidification in a finned tube thermal storage including natural convection,” *Appl. Therm. Eng.*, vol. 84, pp. 320–330, 2015, doi: 10.1016/j.applthermaleng.2015.03.065.

[115] A. Mills, M. Farid, J. R. Selman, and S. Al-Hallaj, “Thermal conductivity enhancement of phase change materials using a graphite matrix,” *Appl. Therm. Eng.*, vol. 26, no. 14–15, pp. 1652–1661, 2006, doi: 10.1016/j.applthermaleng.2005.11.022.

[116] W. Wang, X. Yang, Y. Fang, J. Ding, and J. Yan, “Enhanced thermal conductivity and thermal performance of form-stable composite phase change materials by using β-Aluminum nitride,” *Appl. Energy*, vol. 86, no. 7–8, pp. 1196–1200, 2009, doi: 10.1016/j.apenergy.2008.10.020.

[117] Y. Tian and C. Y. Zhao, “A numerical investigation of heat transfer in phase change materials (PCMs) embedded in porous metals,” *Energy*, vol. 36, no. 9, pp. 5539–5546, 2011, doi: 10.1016/j.energy.2011.07.019.

[118] N. Dukhan and S. Bodke, “An improved PCM heat storage technology utilizing metal foam,” *2010 12th IEEE Intersoc. Conf. Therm. Thermomechanical Phenom. Electron. Syst. ITherm 2010*, pp. 1–7, 2010, doi: 10.1109/ITHERM.2010.5501364.

[119] P. V. S. S. Srivatsa, R. Baby, and C. Balaji, “Numerical investigation of PCM based heat sinks with embedded metal foam/crossed plate fins,” *Numer. Heat Transf. Part Appl.*, vol. 66, no. 10, pp. 1131–1153, 2014, doi: 10.1080/10407782.2014.894371.

[120] A. Sari and A. Karaipekli, “Thermal conductivity and latent heat thermal energy storage characteristics of paraffin/expanded graphite composite as phase change material,” *Appl. Therm. Eng.*, vol. 27, no. 8–9, pp. 1271–1277, 2007, doi: 10.1016/j.applthermaleng.2006.11.004.

[121] K. Lafdi, O. Mesalhy, and S. Shaikh, “Experimental study on the influence of foam porosity and pore size on the melting of phase change materials,” *J. Appl. Phys.*, vol. 102, no. 8, pp. 1–6, 2007, doi: 10.1063/1.2802183.

[122] A. Siahpush, J. O’Brien, and J. Crepeau, “Phase change heat transfer enhancement using copper porous foam,” *J. Heat Transf.*, vol. 130, no. 8, pp. 1–11, 2008, doi: 10.1115/1.2928010.

[123] Y. Zhong, Q. Guo, S. Li, J. Shi, and L. Liu, “Heat transfer enhancement of paraffin wax using graphite foam for thermal energy storage,” *Sol. Energy Mater. Sol. Cells*, vol. 94, no. 6, pp. 1011–1014, 2010, doi: 10.1016/j.solmat.2010.02.004.

[124] Y. Zhong *et al.*, “Heat transfer enhancement of paraffin wax using compressed expanded natural graphite for thermal energy storage,” *Carbon*, vol. 48, no. 1, pp. 300–304, 2010, doi: 10.1016/j.carbon.2009.09.033.

[125] Z. G. Wu and C. Y. Zhao, “Experimental investigations of porous materials in high temperature thermal energy storage systems,” *Sol. Energy*, vol. 85, no. 7, pp. 1371–1380, 2011, doi: 10.1016/j.solener.2011.03.021.

[126] D. Zhou and C. Y. Zhao, “Experimental investigations on heat transfer in phase change materials (PCMs) embedded in porous materials,” *Appl. Therm. Eng.*, vol. 31, no. 5, pp. 970–977, 2011, doi: 10.1016/j.applthermaleng.2010.11.022.

[127] Z. Li, W. G. Sun, G. Wang, and Z. G. Wu, “Experimental and numerical study on the effective thermal conductivity of paraffin/expanded graphite composite,” *Sol. Energy Mater. Sol. Cells*, vol. 128, pp. 447–455, 2014, doi: 10.1016/j.solmat.2014.06.023.

[128] Z. Chen, D. Gao, and J. Shi, “Experimental and numerical study on melting of phase change materials in metal foams at pore scale,” *Int. J. Heat Mass Transf.*, vol. 72, pp. 646–655, 2014, doi: 10.1016/j.ijheatmasstransfer.2014.01.003.

[129] P. Zhang, X. Xiao, Z. N. Meng, and M. Li, “Heat transfer characteristics of a molten-salt thermal energy storage unit with and without heat transfer enhancement,” *Appl. Energy*, vol. 137, pp. 758–772, 2015, doi: 10.1016/j.apenergy.2014.10.004.

[130] D. S. Mehta, K. Solanki, M. K. Rathod, and J. Banerjee, “Thermal performance of shell and tube latent heat storage unit: Comparative assessment of horizontal and vertical orientation,” *J. Energy Storage*, vol. 23, pp. 344–362, Jun. 2019, doi: 10.1016/j.est.2019.03.007.

[131] L. Pu, S. Zhang, L. Xu, and Y. Li, “Thermal performance optimization and evaluation of a radial finned shell-and-tube latent heat thermal energy storage unit,” *Appl. Therm. Eng.*, vol. 166, p. 114753, Feb. 2020, doi: 10.1016/j.applthermaleng.2019.114753.

[132] R. Karami and B. Kamkari, “Experimental investigation of the effect of perforated fins on thermal performance enhancement of vertical shell and tube latent heat energy storage systems,” *Energy Convers. Manag.*, vol. 210, p. 112679, Apr. 2020, doi: 10.1016/j.enconman.2020.112679.

[133] B. K. Choure, T. Alam, and R. Kumar, “A review on heat transfer enhancement techniques for PCM based thermal energy storage system,” *J. Energy Storage*, vol. 72, p. 108161, Nov. 2023, doi: 10.1016/j.est.2023.108161.

[134] Y. Qiao, Y. Du, J. Muehlbauer, Y. Hwang, and R. Radermacher, “Experimental study of enhanced PCM exchangers applied in a thermal energy storage system for personal cooling,” *Int. J. Refrig.*, vol. 102, pp. 22–34, 2019, doi: 10.1016/j.ijrefrig.2019.03.006.

[135] H. E. Khalifa and M. Koz, “Numerical Investigation of the Freezing of a Phase Change Material in a Thermal Storage Device With an Embedded Evaporator,” in *Volume 2: Heat Transfer in Multiphase Systems; Gas Turbine Heat Transfer; Manufacturing and Materials Processing; Heat Transfer in Electronic Equipment; Heat and Mass Transfer in Biotechnology; Heat Transfer Under Extreme Conditions; Computational Heat Transfer; Heat Transfer Visualization Gallery; General Papers on Heat Transfer; Multiphase Flow and Heat Transfer; Transport Phenomena in Manufacturing and Materials Processing*, Washington, DC, USA: American Society of Mechanical Engineers, Jul. 2016. doi: 10.1115/ht2016-7409.

[136] D. Bacellar, T. Alam, J. Ling, and V. Aute, “Automated Parameterized CFD Simulations of Phase-Change Material Embedded Heat Exchangers,” in *2021 20th IEEE Intersociety Conference on Thermal and Thermomechanical Phenomena in Electronic Systems (iTherm)*, San Diego, CA, USA: IEEE, Jun. 2021, pp. 538–543. doi: 10.1109/itherm51669.2021.9503249.

[137] D. Bacellar, T. Alam, J. Ling, and V. Aute, “A Study on Computational Cost Reduction of Simulations of Phase-Change Material (PCM) Embedded Heat Exchangers”.

[138] T. Alam, D. Bacellar, J. Ling, and V. Aute, “Effect of thermal expansion coefficient, viscosity and melting range in simulation of pcm embedded heat exchangers with and without fins,” in *International Mechanical Engineering Congress and Exposition*, 2021.

[139] T. Alam, D. Bacellar, J. Ling, and V. Aute, “Numerical Study And Validation Of Melting And Solidification In PCM Embedded Heat Exchangers With Straight Tube,” 2021.

[140] T. Alam, D. Bacellar, J. Ling, and V. Aute, “Development and Validation of Resistance-Capacitance Model for Phase Change Material Embedded in Porous Media,” in *2022 21st IEEE Intersociety Conference on Thermal and Thermomechanical Phenomena in Electronic Systems (iTherm)*, San Diego, CA, USA: IEEE, May 2022, pp. 1–7. doi: 10.1109/itherm54085.2022.9899532.

[141] T. Alam, G. Righetti, D. Bacellar, V. Aute, and S. Mancin, “Development and Validation Of Resistance-Capacitance Model (RCM) For Phase Change Material (PCM) Embedded In 3D Periodic Structures,” 2022.

[142] T. Alam, J. Yang, J. Tancabel, J. Muehlbauer, Y. Hwang, and V. Aute, “Optimization and Experimental Validation of Annular Finned PCM-HX for a Domestic Hot Water Heater Application,” *20th Int. Refrig. Air Cond. Conf. Purdue*, pp. 1–10, 2024.

[143] M. Menezes, J. Tancabel, D. Bacellar, and V. Aute, “Development & Experimental Validation of a Generalized Resistance-Capacitance Model for Numerical Simulation of Phase-Change Material Embedded Heat Exchangers,” *20th Int. Refrig. Air Cond. Conf.*, pp. 1–10, 2024.

[144] L. Pu, S. Zhang, L. Xu, and Y. Li, “Thermal performance optimization and evaluation of a radial finned shell-and-tube latent heat thermal energy storage unit,” *Appl. Therm. Eng.*, vol. 166, p. 114753, Feb. 2020, doi: 10.1016/j.applthermaleng.2019.114753.

[145] S. Ebadi, M. Al-Jethelah, S. H. Tasnim, and S. Mahmud, “An investigation of the melting process of RT-35 filled circular thermal energy storage system,” *Open Phys.*, vol. 16, no. 1, pp. 574–580, 2018, doi: 10.1515/phys-2018-0075.

[146] M. Rahimi, A. A. Ranjbar, D. D. Ganji, K. Sedighi, M. J. Hosseini, and R. Bahrampoury, “Analysis of geometrical and operational parameters of PCM in a fin and tube heat exchanger,” *Int. Commun. Heat Mass Transf.*, vol. 53, pp. 109–115, 2014, doi: 10.1016/j.icheatmasstransfer.2014.02.025.

[147] M. Schimmelpfennig, K. Weber, F. Kalb, and K. Feller, “Volume expansion of paraffins from dip tube measurements,” *Synthesewachs.Com*, no. 430 ml, pp. 1–9, 2007.

[148] RUBITHERM GmbH, “RUBITHERM RT35 Phase change material.” [Online]. Available: https://www.rubitherm.eu/media/products/datasheets/Techdata_-RT35_EN_02092022.PDF

[149] Ansys Inc., *ANSYS Fluent, Release 2021 R2, Help System, Fluent Theory Guide*. (2021). Ansys Inc., Canonsburg, PA, USA.

[150] T. Alam, D. Bacellar, J. Ling, and V. Aute, “Development and Validation of Resistance-Capacitance Model for Phase Change Material Embedded in Porous Media,” in *2022 21st IEEE Intersociety Conference on Thermal and Thermomechanical Phenomena in Electronic Systems (iTherm)*, San Diego, CA, USA: IEEE, May 2022, pp. 1–7. doi: 10.1109/iTherm54085.2022.9899532.

[151] T. Alam, G. Righetti, D. Bacellar, V. Aute, and S. Mancin, “Development and Validation Of Resistance-Capacitance Model (RCM) For Phase Change Material (PCM) Embedded In 3D Periodic Structures,” 2022.

[152] K. Deb, “Multiobjective Optimization Using Evolutionary Algorithms. Wiley, New York,” 2001.

[153] US Department of Energy, “Code of Federal Regulations, 2016, Title 10 – Energy, Chapter X - DEPARTMENT OF ENERGY (GENERAL PROVISIONS),” 2016.

[154] A. Najafian, F. Haghighat, and A. Moreau, “Integration of PCM in domestic hot water tanks: Optimization for shifting peak demand,” *Energy Build.*, vol. 106, pp. 59–64, Nov. 2015, doi: 10.1016/j.enbuild.2015.05.036.

[155] X. Yang, Z. Lu, Q. Bai, Q. Zhang, L. Jin, and J. Yan, “Thermal performance of a shell-and-tube latent heat thermal energy storage unit : Role of annular fins,” vol. 202, pp. 558–570, 2017, doi: 10.1016/j.apenergy.2017.05.007.

[156] RUBITHERM GmbH, “RT62HC.” [Online]. Available: https://www.rubitherm.eu/media/products/datasheets/Techdata_-RT62HC_EN_09102020.PDF

[157] T. Alam, D. Bacellar, J. Ling, and V. Aute, “Development and Validation of Resistance-Capacitance Model for Phase Change Material Embedded in Porous Media,” *Intersoc. Conf. Therm. Thermomechanical Phenom. Electron. Syst. ITHERM*, vol. 2022-May, no. 2011, pp. 1–10, 2022, doi: 10.1109/iTherm54085.2022.9899532.

[158] J. Yang, J. Muehlbauer, J. Tancabel, V. Aute, and Y. Hwang, “Experimentation on Finned-Tube Microchannel Heat Exchanger Incorporating Phase Change Material and R-410A. 20th International Refrigeration and Air Conditioning Conference at Purdue, July 15-18, 2024.,” 2024.

[159] H. Zheng, C. Wang, Q. Liu, Z. Tian, and X. Fan, “Thermal performance of copper foam/paraffin composite phase change material,” *Energy Convers. Manag.*, vol. 157, no. September 2017, pp. 372–381, 2018, doi: 10.1016/j.enconman.2017.12.023.

[160] T. Alam, “Development, Validation and Application of Resistance-Capacitance Based Models (RCM) for Phase Change Material Heat Exchangers,” University of Maryland, 2023. doi: https://doi.org/10.13016/dspace/h1ku-eaj4.

[161] M. Momeni, S. Jalilian, and A. Fartaj, “Heat Transfer Analysis of a Crossflow Minichannel Heat Exchanger Based on Air and Liquid Flow,” *Int. Conf. Fluid Flow Heat Mass Transf.*, vol. 10, pp. 86–96, 2023, doi: 10.11159/ffhmt23.110.

[162] S. Jalilian, M. Momeni, and A. Fartaj, “Enhancing thermal performance and optimization strategies of PCM-integrated slab-finned two-fluid heat exchangers for sustainable thermal management,” *J. Energy Storage*, vol. 75, no. August 2023, p. 109587, 2024, doi: 10.1016/j.est.2023.109587.

[163] S. Kahwaji, M. B. Johnson, A. C. Kheirabadi, D. Groulx, and M. A. White, “A comprehensive study of properties of paraffin phase change materials for solar thermal energy storage and thermal management applications,” *Energy*, vol. 162, pp. 1169–1182, 2018, doi: 10.1016/j.energy.2018.08.068.

[164] S. Madruga, N. Haruki, and A. Horibe, “Experimental and numerical study of melting of the phase change material tetracosane,” *Int. Commun. Heat Mass Transf.*, vol. 98, no. September, pp. 163–170, 2018, doi: 10.1016/j.icheatmasstransfer.2018.08.021.

[165] L. Jian-you, “Numerical and experimental investigation for heat transfer in triplex concentric tube with phase change material for thermal energy storage,” *Sol. Energy*, vol. 82, no. 11, pp. 977–985, 2008, doi: 10.1016/j.solener.2008.05.006.

[166] S. Zhang, L. Pu, L. Xu, R. Liu, and Y. Li, “Melting performance analysis of phase change materials in different finned thermal energy storage,” *Appl. Therm. Eng.*, vol. 176, no. March, p. 115425, 2020, doi: 10.1016/j.applthermaleng.2020.115425.

[167] L. Klimeš *et al.*, “Computer modelling and experimental investigation of phase change hysteresis of PCMs: The state-of-the-art review,” *Appl. Energy*, vol. 263, no. August 2019, p. 114572, 2020, doi: 10.1016/j.apenergy.2020.114572.

[168] Y. Qiao, T. Cao, Y. Hwang, and R. Radermacher, “Investigation on Phase change material (PCM)-to-refrigerant Heat Exchanger in Air-conditioning Systems,” 2021.

[169] R. Dhumane *et al.*, “Enhancing the thermosiphon-driven discharge of a latent heat thermal storage system used in a personal cooling device,” *Int. J. Refrig.*, vol. 88, pp. 599–613, 2018, doi: 10.1016/j.ijrefrig.2018.02.005.

[170] V. Gnielinski, “On heat transfer in tubes,” *Int. J. Heat Mass Transf.*, vol. 63, pp. 134–140, 2013, doi: 10.1016/j.ijheatmasstransfer.2013.04.015.

[171] M. M. Shah, “General correlation for heat transfer during condensation in plain tubes: Further development and verification,” *ASHRAE Trans.*, vol. 119, no. PART 2, pp. 3–11, 2013.

[172] A. Pizzolato, A. Sharma, K. Maute, A. Sciacovelli, and V. Verda, “Design of effective fins for fast PCM melting and solidification in shell-and-tube latent heat thermal energy storage through topology optimization,” *Appl. Energy*, vol. 208, no. October, pp. 210–227, 2017, doi: 10.1016/j.apenergy.2017.10.050.

[173] “RT35 Data Sheet,” Rubitherm Technologies. [Online]. Available: https://www.rubitherm.eu/media/products/datasheets/Techdata_-RT35_EN_09102020.PDF

[174] “Standard 90.1.” Accessed: Jun. 29, 2025. [Online]. Available: https://www.ashrae.org/technical-resources/bookstore/standard-90-1

[175] W. Delgado-Diaz, A. Stamatiou, S. Maranda, R. Waser, and J. Worlitschek, “Comparison of Heat Transfer Enhancement Techniques in Latent Heat Storage,” *Appl. Sci.*, vol. 10, no. 16, p. 5519, Aug. 2020, doi: 10.3390/app10165519.

[176] “PlusICE Range 2021-1 - PCM Products Ltd.”

[177] M. Wetter, K. Benne, H. Tummescheit, and C. Winther, “Spawn: coupling Modelica Buildings Library and EnergyPlus to enable new energy system and control applications,” *J. Build. Perform. Simul.*, vol. 17, no. 2, pp. 274–292, Mar. 2024, doi: 10.1080/19401493.2023.2266414.

[178] Gregor P. Henze and Moncef Krarti, “Predictive Optimal Control of Active and Passive Building Thermal Storage Inventory,” University of Nebraska, DE-FC-26-01NT41255, Sep. 2001.

[179] H. Selvnes, Y. Allouche, R. I. Manescu, and A. Hafner, “Review on cold thermal energy storage applied to refrigeration systems using phase change materials,” *Therm. Sci. Eng. Prog.*, vol. 22, p. 100807, May 2021, doi: 10.1016/j.tsep.2020.100807.

[180] M. Wetter, W. Zuo, T. S. Nouidui, and X. Pang, “Modelica Buildings library,” *J. Build. Perform. Simul.*, vol. 7, no. 4, pp. 253–270, Jul. 2014, doi: 10.1080/19401493.2013.765506.

[181] Dept. of Energy Building Technologies Office, “Prototype Building Models | Building Energy Codes Program,” 2022, Accessed: Nov. 03, 2022. [Online]. Available: https://www.energycodes.gov/prototype-building-models

[182] A. Othman, V. Aute, and J. Tancabel, “Recharge Demand Mitigation for Latent Heat Thermal Energy Storage at Off-Peak Hours,” *Int. High Perform. Build. Conf.*, Jan. 2024, [Online]. Available: https://docs.lib.purdue.edu/ihpbc/453

[183] conEdison, “Time-of-Use Rates.” Accessed: Jun. 02, 2025. [Online]. Available: https://www.coned.com/en/accounts-billing/your-bill/time-of-use

[184] Xcel Energy, “Time of Use Rates.” Accessed: Jun. 02, 2025. [Online]. Available: https://mn.my.xcelenergy.com/s/business/rate-plans/time-of-use

[185] FPL Northwest FL, “Time of Use Rates.” Accessed: Jun. 02, 2025. [Online]. Available: https://www.fpl.com/northwest/rates/business-options.html

[186] A. Pizzolato, A. Sharma, K. Maute, A. Sciacovelli, and V. Verda, “Design of effective fins for fast PCM melting and solidification in shell-and-tube latent heat thermal energy storage through topology optimization,” *Appl. Energy*, vol. 208, no. June, pp. 210–227, 2017, doi: 10.1016/j.apenergy.2017.10.050.

[187] YANG J, MUEHLBAUER J, BACELLAR D, LING J, AUTE V, and HWANG Y, “Experimental investigation of melting and solidification processes of phase change material heat exchanger.” International Institute of Refrigeration (IIR), 2021. doi: 10.18462/IIR.PCM.2021.2034.

[188] J. Yang, J. Muehlbauer, D. Bacellar, V. Aute, and Y. Hwang, “Experimental Investigation of a Phase Change Material Charged Serpentine Heat Exchanger with Louvered Fins,” 2023.

[189] J. Yang, J. Muehlbauer, D. Bacellar, V. Aute, and Y. Hwang, “Experimental Investigation of Melting and Solidification Processes of Phase Change Material Heat Exchanger,” 2021, doi: 10.18462/iir.PCM.2021.2034.

[190] J. Yang, J. Muehlbauer, D. Bacellar, J. Ling, V. Aute, and Y. Hwang, “Experimental Investigation of a Phase Change Material Charged Finned-Tube Heat Exchanger,” 2022.

[191] J. Yang, J. Muehlbauer, D. Bacellar, V. Aute, and Y. Hwang, “Experimental Investigation of a Phase Change Material Charged Serpentine Heat Exchanger with Louvered Fins,” 2023.

[192] T. Alam, J. Yang, J. Tancabel, J. Muehlbauer, Y. Hwang, and V. Aute, “Optimization and Experimental Validation of Annular Finned PCM-HX for a Domestic Hot Water Heater Application,” 2024.

[193] J. Yang, J. Muehlbauer, J. Tancabel, V. Aute, and Y. Hwang, “Experimentation on Finned-Tube Microchannel Heat Exchanger Incorporating Phase Change Material and R-410A,” 2024.

[194] J. Woods, A. Mahvi, A. Goyal, E. Kozubal, A. Odukomaiya, and R. Jackson, “Rate capability and Ragone plots for phase change thermal energy storage,” *Nat. Energy*, vol. 6, no. 3, pp. 295–302, 2021, doi: 10.1038/s41560-021-00778-w.